NON-LOCAL EFFECTS on SURFACE PLASMON THEORY and THEIR NOVEL APPLICATIONS : NANO-SCALE PLASMONIC STRUCTURES

by

Arif Engin Çetin

A Thesis Submitted to the
Graduate School of Engineering
in Partial Fulfillment of the Requirements for
the Degree of

Master of Science

in

Electrical & Computer Engineering

Koç University

July, 2009

Koç University
Graduate School of Sciences and Engineering

This is to certify that I have examined this copy of a master's thesis by

Arif Engin Çetin

and have found that it is complete and satisfactory in all respects,
and that any and all revisions required by the final
examining committee have been made.

Committee Members:

Assoc. Prof. Özgür E. Müstecaplıoğlu

Prof. Alphan Sennaroğlu

Assoc. Prof. Kaan Güven

Date:

ABSTRACT

Non-Local Effects on Surface Plasmon Theory and Their Novel Applications : Nano-Scale Plasmonic Structures

In this study, we have explored the surface plasmon theory with Bloch hydrodynamic model and compared the results with Drude model to point out the advantage of the non-local models over free electron models at higher frequencies, especially around the plasma frequency. We have then shown how this model affects the extraordinary transmission of light through a single subwavelength slit embedded in a metal layer. By obtaining the dielectric constant of the metals with Bloch model, we consider the interrelated effects between the field and the material which the field impinges on. We have reported the differences between Bloch and Drude models in the permittivity of the metal medium and we have shown how these differences affect the surface plasmon excitation and dispersion relation for a two-layered medium of dielectric-metal qualitatively and quantitatively. We have recalculated the effective refractive index of the slit embedded in a metal layer with Bloch's hydrodynamic model and shown the differences with Drude model. We have then determined the transmission of light through metallic nano-apertures in a metal layer whose dielectric response modeled by Drude and Bloch models to show how non-local models predict the transmittance behavior of subwavelength apertures more realistically than free-electron models and we have shown how Bloch model contributes in controlling light transmission through nano-slits. Bloch model gives the advantage that, we can control the transmittance behavior of nano-apertures by changing the material parameters defined by Bloch model. This advantage has been used to design new nano-circuit elements for beam shaping and tilting using subwavelength systems. We have shown how we control the focusing and deflecting mechanisms by changing the material characteristics modeled by Bloch's hydrodynamic model.

Keywords: non-local model, hydrodynamic model, surface plasmon, extraordinary transmission, nano-optic lens, beam shaping, beam tilting.

ÖZETÇE

Yüzey Plazmonları Üzerindeki Yerel Olmayan Etkiler ve Yeni Uygulamaları : Nano Ölçekli Plazmonik Yapılar

Bu çalışmada, yüzey plazmon teorisini Bloch hidrodinamik modeli ile inceledik ve yüksek frekansta, özellikle de plazma frekansı civarında yerel olmayan teorilerin, bağımsız elektron teorilerine göre daha avantajlı olduğunu göstermek için Bloch modeli ile bulunan sonuçları Drude modeli ile bulunanlar ile karsılaştırdık. Daha sonra bu modelin, ışığın metal tabakasına yerleştirilmiş dalgaboyu altında olan aralıktan aktarılmasını nasıl etkilediğini gösterdik. Metallerin dielektrik sabitlerini Bloch modeli ile elde ederek, alan ve alanın çarptığı materyalin arasındaki ilişkiyi değerlendirmiş olduk. Bloch ve Drude modellerinden elde edilen dielektrik sabiti sonuçlarındaki farkları rapor ettik ve bu farkların yüzey plazmonunun uyarılmasını ve saçılım ilişkisini nasıl etkilediğini nitel ve nicel olarak gösterdik. Metal tabakasına yerleştirilmiş olan aralığın efektif kırılma indisini Bloch hidrodinamik modelini kullanarak tekrar hesapladık ve sonuçları Drude modeli ile karşılaştırdık. Daha sonra, yerel olmayan teorilerin bağımsız elektron modellerine göre dalgaboyu altındaki deliklerin iletim davranışlarını daha gerçekçi öngördüğünü göstermek için dielektrik tepkisi Drude ve Bloch modelleriyle modellenmiş olan metal tabakanın içine yerleştirilmiş nano deliklerden ışığın aktarımını yeniden hesapladık ve Bloch modelinin ışığın nano deliklerden aktarımına nasıl katkı sağladığını gösterdik. Bloch modeli, model tarafından tanımlanmış olan materyal parametrelerini kullanalarak nano deliklerin aktarım davranışlarını kontrol edebilme avantajını sağlar. Bu avantaj, ışığın şekillendirilmesi ve bükülmesinde kullanılan nano devre elemanlarının tasarımında kullanıldı. Bloch modeli tarafından belirlenen materyal parametrelerini kullanarak odaklama ve saptırma mekanizmalarını nasıl kontrol ettiğimizi gösterdik.

Anahtar kelimeler: yerel olmayan model, hidrodinamik model, yüzey plazmonu, olağanüstü geçirgenlik, nano optik lens, ışın şekillendirme, ışın bükme.

ACKNOWLEDGMENTS

Foremost, I would like to express my gratitude to my advisor, Assoc. Prof. Özgür E. Müstecaplıoğlu for the continuous support of my research. His guidance, inspiration and encouragement helped me in my research and writing of this thesis. I could not have imagined having a better advisor and mentor for my M.S. study.

I would like to thank Prof. M. İrşadi Aksun for his guidance and providing the necessary basis and proper conditions for my thesis project.

I would like to thank Prof. Alphan Sennaroğlu for his appreciable suggestions, criticism and comments in my thesis project.

I would like to thank Assoc. Prof. Kaan Güven for his collaboration in my thesis project.

I would like to thank Prof. Ali Serpengüzel for his support and guidance in my subproject.

I would also like to thank TÜBİTAK (The Scientific and Technological Research Council of Turkey) for providing the graduate scholarship during my M.S. study.

I would like to thank my friends, Birsen, Pınar, Aytaç, Seda, Ersen and Selim for their support and optimism that helps me in long days of my project.

Finally I would like to thank my parents, Süleyman Çetin and Hanife Çetin and my brother Erdem Çetin for their endless support and love, which made it possible to achieve my goals in my life.

TABLE OF CONTENTS

LIST OF FIGURES

Chapter 1

INTRODUCTION

The interaction between light and matter is a very important topic in science and technology. Using light, researchers have made innumerable discoveries in the last twenty years but when it comes to interaction between light and a metal, subwavelength scale structures do not lead to the expected results predicted by the conventional theories such as low transmission of light through nano-apertures in subwavelength size. Microchips, nano-circuits and optical data storage devices are made at the limit of conventional optics and these restrictions are still a constraint for researchers. Thus, new ways to modulate photons had to be found. In that sense, since the pioneering work of Ritchie in 1954, surface plasmons have been widely recognized in the field of surface science [3]. Surface plasmons give the advantage that the optical circuit elements can be manufactured in nano-size, very small compared to the wavelength of light and designed to work at very small wavelengths. Surface plasmons are the electromagnetic waves that propagate at the interface between a metal and a dielectric medium. As shown in figure 1.1, on the surface of the metal, the collective oscillations of the electrons excited by the electric field of the light hitting the metal surface allow the formation of surface plasmons.

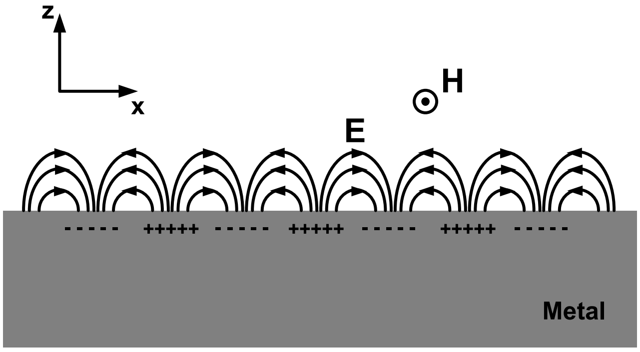

Figure 1.1: Electric field of the light which is normal to the surface of the metal triggers the free electron oscillation which results in the surface plasmon excitation.

One of the nice illustrations of the surface plasmon is the colored glass, the famous Lycurgus cup shown in figure 1.2 made by ancient roman artists and is today exhibited at the British Museum in London. When illuminated by a white source from outside, the cup shows in green color and when illuminated from inside, it appears red. For a long time it was not clear what causes this phenomenon. Today, it is known that this phenomenon is due to the nanometer-sized gold particles embedded in the glass. The colors are determined by an interplay of reflection (figure 1.2 - (a)) and transmission (figure 1.2 - (b)).

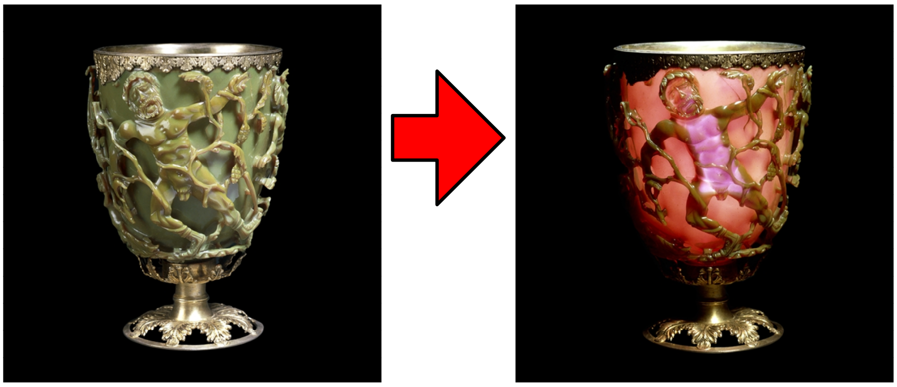

(a) Reflected wave **(b) Transmitted wave**

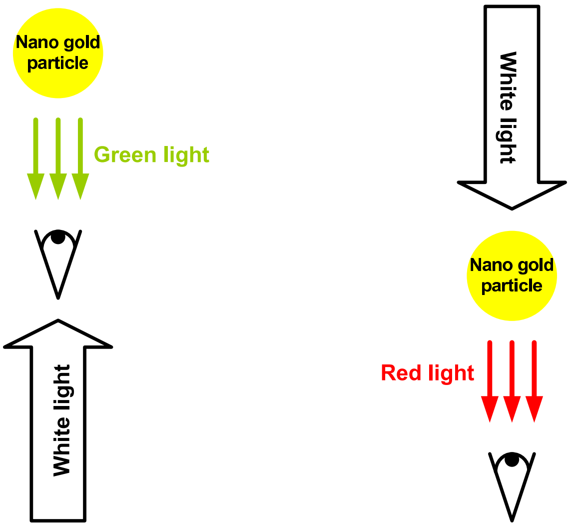

Figure 1.2: Ancient roman Lycurgus cup illuminated by a light source from (a) outside and (b) inside. Light absorption by the embedded gold particles leads to a red color of the transmitted light whereas scattering at the particles yields a greenish color.

The reason behind this optical phenomenon is that the metal particles (gold) inside the cup have free electrons floating around them. The electric field of the light and the free electrons of the gold particles interfere and at the interface between light and electrons, the oscillation of the electric field of the light causes the electrons in the metal to oscillate. Due to the fact that the electrons have mass, it takes time to make them move. Hence, they tend to oscillate in a certain phase difference with the electric field of light. For instance, if the electric field moves right, the free electrons move left. This anti-phase movement prevents the light from entering the metal and the free electrons form a screening field that the light cannot pass through so it is reflected because there is no way for the light to go. The free electrons can only oscillate at certain frequencies which depend on the allowed standing waves which are the surface plasmons, oscillations of the free electrons at the surface of a metal at a certain frequency. At this frequency range, the light is highly absorbed and scattered, which results in the color properties of the cup, green (enhanced reflection) and red colors (enhanced transmisson).

In new the field of optics, surface plasmons help us to concentrate and channel light using subwavelength structures [2]. In these structures, it is possible to transform photons into plasmons, use their special properties to manipulate and process the original light wave properties by the logic elements and then reconvert the plasmons into photons. This aspect leads to minimize the size of the photonic circuits by a scale of length smaller than the conventional ones. The electromagnetic field of the surface plasmon is confined to the interface and this confinement leads to the enhancement of the electromagnetic field at the interface which results in a great sensitivity to surface conditions, such as surface roughness or adsorbates on the surface [4]. This sensitivity phenomenon can be used in chemo and bio sensors for characterizing the optical properties of complex structures such as bio-molecules. Using surface plasmons, metals can be used as a photonic band-gap material but in this time, the surface is periodically textured [2]. When the periodicity of texturing of the metal surface is equal to half of the wavelength of the surface plasmon, scattering leads to the formation of the surface plasmon standing waves and the surface plasmon modes are prevented from traveling in any direction (band-gap formation).

While the conventional aperture theory predicts that small nano-apertures show low transmittance behavior, the periodic nano-hole arrays have much higher transmission by the surface plasmon related effects [1]. This idea is used for signal enhancement in near field microscopy by using structures including nano slits and grooves embedded in metal layers. Surface plasmons have a great potential as a new class of subwavelength photonic devices [2]. Their related effects, near-field character and field enhancement capability lead to innumerable developments in optics and surface science. As the researchers understand the surface plasmon phenomenon, i.e. how they propagate on the surfaces, couple to the propagating modes or carry energy on the subwavelength structures where the light cannot propagate on, they design new devices such as waveguides, reflectors, beam splitters and beam shapers by using subwavelength metallic structures. Surface plasmon is still a developing concept in nano-science and further work is needed to make completely plasmonic circuits.

In this thesis, we have explored the non-local effects on the surface plasmon theory. Nano-lenses provide beam focusing and deflecting for data storage, near-field microscopy and scanning [13]. In nano-lens operation, the principle of extraordinary light transmission is used which surface plasmon resonances result in the enhanced optical transmission of light through a subwavelength aperture. It is desirable to increase the operational frequencies of nano-lenses but near the plasma frequency non-local effects play a significant role. We have applied Bloch's hydrodynamic model to investigate spatial dispersion effects in enhanced transmission of nano-apertures. Using Bloch's model, we have found new surface plasmon excitations near the plasma frequency and exploited them to increase the working frequency of nano-lenses to higher frequencies. The focal length is found to be highly sensitive to the propagation speed of the hydrodynamic disturbances. In addition, some novel controllable nano-structure designs are suggested with movable slits and convex shape that can enhance nano-scanning capabilities to wider angles.

Nano-optic lenses are slits of subwavelength size embedded in metal layers. Studies of transmission through subwavelength apertures suggest the potential for applications of the nanoscale control of light [1], [2], [13], [15], [16], [20], [28], [29]. The metallic nano-optic lenses are used because of their advantages of unaffected by the diffraction effects unlike the conventional dielectric lenses and adjustable focal length that varies with the number of slits [13].

Previous studies have shown that surface plasmons play a significant role in the enhanced transmission of light through nano-slits [2], [13], [28]. Despite the fact that the dielectric response of the materials is nonlocal, the dielectric function of the metals used in the nano-optic lens designs is modeled using the Drude model [30] which only accounts for the frequency dependence of the dielectric response function and completely ignores its wave vector dependence. On the other hand, for many metallic materials, especially near the plasma frequency, free electron theory is not reliable [31]. The Drude model is successful in modeling the dielectric function of the materials at lower frequencies but at higher frequencies around the plasma frequency, non-local interaction plays significant role. To check whether an optical phenomenon needs a nonlocal theory or not, Bloch's hydrodynamic model can be used as a benchmark [32], [33], before considering more sophisticated nonlocal theories, such as Lindhard-Mermin [34] or Boltzmann-Mermin models. Since its first introduction [35], hydrodynamic model has been used to illuminate many nonlocal optical properties of semiconductors and conductors [37].

This thesis uses Bloch's hydrodynamic model to examine the non-local surface plasmon effects in enhanced transmission of nano-apertures and nano-circuit designs. In addition to a general discussion of spatial dispersion effects, specific example of silver has been given, for which hydrodynamic model works well around the plasma frequency while the usual Drude model fails [40], [41]. For nano-lens applications, silver is the commonly preferred metal in experiments. Despite the well-known empirical or semi-empirical [42], as well as analytical, dielectric response functions specifically developed for silver [43], the hydrodynamic model, with its generality and simplicity, has been used in a more general context in the thesis. Silver has been referred only for a specific example while reporting our enhanced transmission and nano-structure results which are also valid for a wide range of metals.

Throughout the thesis, in Chapter 2, the classical theory of surface plasmon including the surface plasmon dispersion relation and the surface plasmon length scales has been explored. In Chapter 3, one of the conventional setups used to excite surface plasmon, which is the Otto configuration, has been described in detail. Chapter 4 discusses the reason of the fact that TE waves cannot be used for the surface plasmon excitation and proposes a new method, which is applying the left handed materials in the Otto configuration. In Chapter 5, the dielectric function of silver has been modeled by Drude and Bloch models and the difference of both models in describing the permittivity around the plasma frequency has been investigated. After that, the classical surface plasmon theory has been re-studied with

Bloch's hydrodynamic model and the differences in the surface plasmon dispersion relation obtained by Drude and Bloch models have been examined. Chapter 6 explains the fundamental theory of enhanced transmission of light through nano-apertures and then gives some examples of nano-circuitry for beam shaping and tilting. At the end of the chapter, the advantage of the controllable manner of Bloch model on the material has been proposed for the nano-circutry examples as a new and easily applicable approach for beam shaping and tilting.

Chapter 2

SURFACE PLASMON THEORY

2.1 Introduction

In this chapter, the theory behind the surface plasmon excited at an interface between a dielectric and a metal layer has been reviewed and the surface plasmon length scales have been discussed.

2.2 Surface Plasmon Dispersion Relation

The interaction between surface charges and electromagnetic field of light has two consequences. First, this interaction results in a momentum mismatch that the momentum of the surface plasmon, $\hbar k_{sp}$ (or the magnitude of the surface plasmon wavevector) is greater than that of free space photon of the same frequency, $\hbar k_0$ and this increase in momentum is due to the binding of the surface plasmon to the surface in other words the strong coupling between light and surface charges. Second, while the surface plasmon wave propagates along the surface, the field normal to the surface is evanescent field which decays exponentially with distance from the surface [2]. Therefore, surface plasmon modes on a planar metal surface are bound to the surface and propagates until their energy is dissipated as heat in the metal.

The electromagnetic field of the surface plasmon at a dielectric-metal interface is obtained from the Maxwell's equations and the associated boundary conditions. Consider a TM (transverse magnetic) polarized wave that propagates in x-direction and decays in z-direction in the structure consisting of a dielectric characterized by a real and positive dielectric constant ε_d in $z > 0$ and a metal characterized by a frequency dependent and complex dielectric constant $\varepsilon(w) = \varepsilon(\omega)' - j\varepsilon(\omega)''$ in $z < 0$ as shown in figure 2.1.

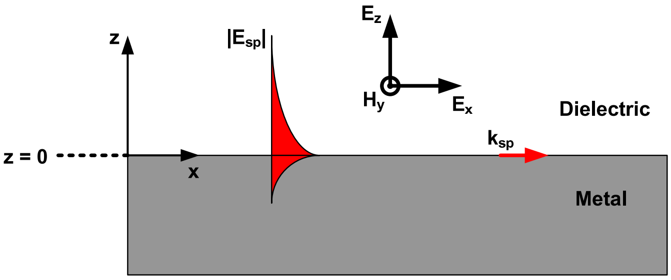

Figure 2.1: Surface plasmon at an interface between a dielectric and a metal layer.

In the dielectric region ($z > 0$), the electric and magnetic fields are

$$\begin{aligned} \mathbf{H}(r,t) &= \widehat{y}Ae^{-jk_x x - k_z^{(d)}z + j\omega t} \\ \mathbf{E}(r,t) &= (A\frac{1}{j\omega\varepsilon_0\varepsilon_d})(\widehat{x}k_z^{(d)} - \widehat{z}jk_x)e^{-jk_x x - k_z^{(d)}z + j\omega t} \end{aligned} \tag{2.1}$$

and in the metal region ($z < 0$)

$$\begin{aligned} \mathbf{H}(r,t) &= \widehat{y}Be^{-jk_x x + k_z^{(m)}z + j\omega t} \\ \mathbf{E}(r,t) &= (B\frac{1}{j\omega\varepsilon_0\varepsilon(\omega)})(-\widehat{x}k_z^{(m)} - \widehat{z}jk_x)e^{-jk_x x + k_z^{(m)}z + j\omega t} \end{aligned} \tag{2.2}$$

where $k_z^{(d,m)}$ determines the decay in the electromagnetic field and is calculated from the Maxwell's wave equation as below.[1]

$$\nabla^2\mathbf{H} - \frac{\varepsilon_r}{c^2}\frac{\partial^2\mathbf{H}}{\partial t^2} = 0 \Longrightarrow -k_x^2 + (k_z^{d,m})^2 + \varepsilon_{d,m}(\frac{\omega}{c})^2 = 0 \tag{2.3}$$

Thus, we get the normal components of the wavevectors in both media as

$$\begin{aligned} k_z^{(d)} &= (k_x^2 - \varepsilon_d(\omega/c)^2)^{\frac{1}{2}} \qquad z > 0 \\ k_z^{(m)} &= (k_x^2 - \varepsilon(\omega)(\omega/c)^2)^{\frac{1}{2}} \qquad z < 0 \end{aligned} \tag{2.4}$$

Assuming that there is no charge and current source ($\mathbf{J}_s = 0$ and $\rho_s = 0$) in the structure, the boundary conditions at the interface between two media ($z = 0$) requiring that the tangential components (x and y components) of the electric and magnetic fields should be continuous yields

$$A = B, \qquad A\frac{k_z^{(d)}}{\varepsilon_d} = -B\frac{k_z^{(m)}}{\varepsilon(\omega)} \tag{2.5}$$

---

[1] Permittivity of the layers, μ_r is assumed to be 1.

From equation 2.5, we get the following relationship.

$$\frac{k_z^{(m)}}{k_z^{(d)}} = -\frac{\varepsilon(\omega)}{\varepsilon_d} \tag{2.6}$$

In order for equations 2.1 and 2.2 to describe a surface electromagnetic wave, $k_z^{(d)}$ and $k_z^{(m)}$ must be real and positive. Hence, $\varepsilon(\omega)$ must be negative to yield the equality shown in equation 2.6.

Squaring both sides of equation 2.6 and substituting the square of equation 2.4 into equation 2.6, the surface plasmon wavevector $k_{sp} = k_x$ is found as in equation 2.7.

$$k_{sp} = \frac{\omega}{c}\sqrt{\frac{\varepsilon_d \varepsilon(\omega)}{\varepsilon_d + \varepsilon(\omega)}} = k_0\sqrt{\frac{\varepsilon_d \varepsilon(\omega)}{\varepsilon_d + \varepsilon(\omega)}} \tag{2.7}$$

When a dipole source which is the source of both propagating and decaying TM polarized waves is located on the surface of the metal as shown in figure 2.2, the evanescent fields produced by the dipole excite the surface plasmon on the surface of the metal.

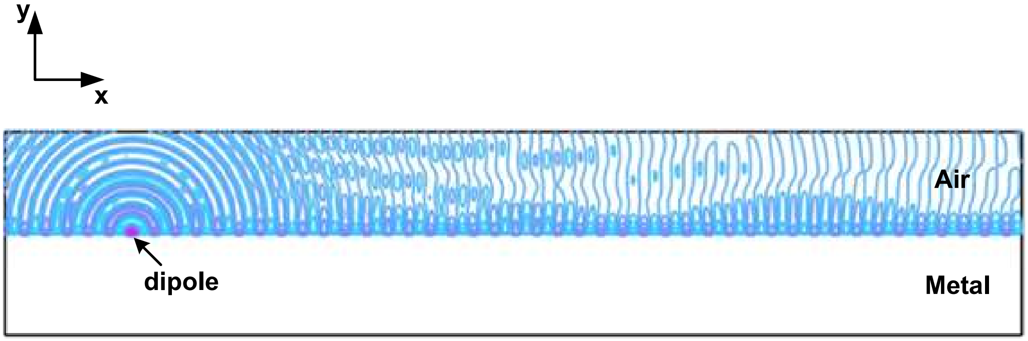

Figure 2.2: COMSOL Multiphysics simulation of the system where a dipole is located on the surface of the metal. Thicknesses of the air and metal layers are infinite. The corresponding parameters are $\lambda = 852$ nm, $\varepsilon_m = -33.22 - j1.17$ and $\varepsilon_d = 1$.

The surface wave nature of the field generated by the dipole can be approximated as $\Upsilon \frac{e^{-jkx}}{\sqrt{x}}$ where Υ is the amplitude of the field and x is the distance along the interface. To find the wavevector of the wave that propagates on the surface of the metal, we use the Generalized Pencil of Function (GPOF) method (discussed in Appendix A), a method to approximate the functions by the sum of complex exponentials [17]. In this method, first the field data are multiplied with $\sqrt{x}$ to reduce the problem to a problem of the summation of exponentials then using the GPOF method, new data are fitted to exponentials to find the wavevector of the field.

In figure 2.3, the tangential component of the wavevector, in other words the wave component propagating on the surface of the metal is shown. Notice that, at the distance far away from the dipole, the wavevector converges to the surface plasmon wavector which means on the surface of the metal, the dominant field that propagates on the surface is the surface plasmon.

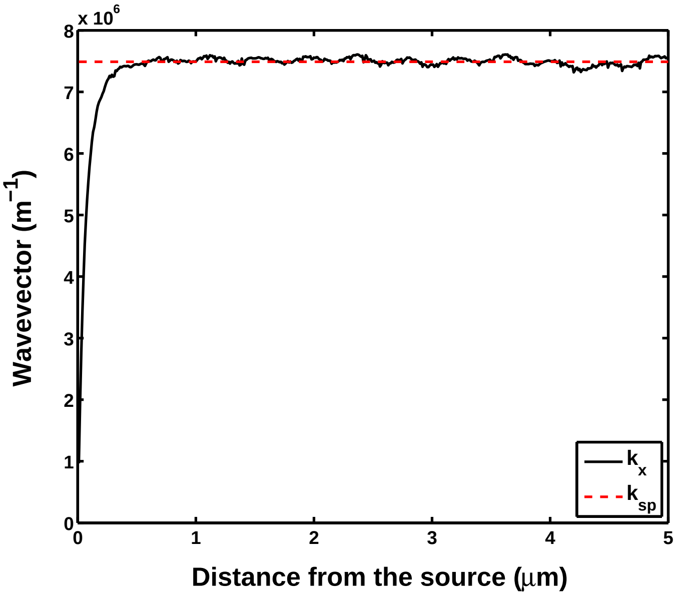

Figure 2.3: The tangential component (propagating component) of the wavevector of the wave on the surface of the metal. The corresponding parameters are $\lambda = 852$ nm, $\varepsilon_m = -33.22 - j1.17$ and $\varepsilon_d = 1$.

At this stage, the frequency dependent dielectric function of the metal can be modeled by the Drude model as below.

$$\varepsilon(\omega) = 1 - \frac{\omega_p^2}{\omega^2 - j\Gamma\omega} \tag{2.8}$$

where ω_p is the plasma frequency which is the frequency of bulk longitudinal electron excitations and Γ is the scattering rate used to show the dissipation of the electron motion. Assuming that the real part of $\varepsilon(\omega)$ is dominant, the corresponding dispersion curve of the surface plasmon is drawn by taking the real part of surface plasmon wavevector as in figure 2.4 [5].

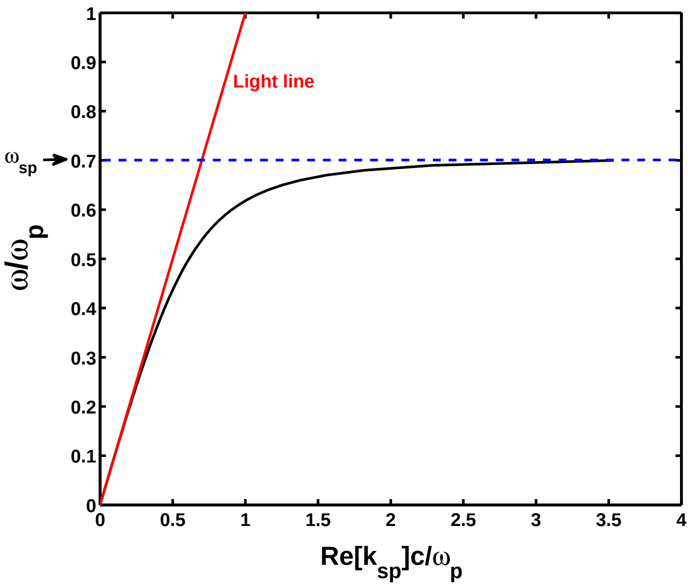

Figure 2.4: Dispersion curve of the surface plasmon at an interface between a dielectric and a metal layer. The corresponding parameters are $\omega_p/2\pi = 12 \times 10^{15}$ Hz (7.9 eV), $\Gamma = 1.45 \times 10^{13}$ Hz (0.06 eV) and $\varepsilon_d = 1$.

The dispersion curve shows that at low frequencies, the surface plasmon mode lies close to the light line (the dispersion of light in the dielectric medium, $\omega = ck/\sqrt{\varepsilon_d}$) and is predominantly light-like and in this region it is described as polariton. As the frequency rises, the mode moves further away from the light line and gradually approaches an asymptotic limit, the surface plasmon frequency, ω_{sp} [5].

$$\omega_{sp} = \frac{\omega_p}{\sqrt{1+\varepsilon_d}} \tag{2.9}$$

This occurs when the permittivity of the metal and the dielectric medium are of the same magnitude but opposite sign. Also because $k_{sp} > \sqrt{\varepsilon_d}k_0$, we cannot use the incident plane wave light to couple the surface plasmon modes and the surface plasmon cannot radiate light into the dielectric medium.[2]

The dispersion relation (equation 2.7) shows that due to the complex nature of the dielectric function of the metal (imaginary part is due to the ohmic losses in the metal), k_{sp} is also a

---

[2] The light field has to drag the electrons along the metal surface. Consequently, this means that the surface plasmon on a plane interface cannot be excited by light of any frequency that propagates in free space.

complex quantity.

$$k_{sp} = k'_{sp} - jk''_{sp} \tag{2.10}$$

Due to its complex wavevector, surface plasmons attenuate as they propagate and the energy carried by the surface plasmon decays exponentially.

2.3 Surface Plasmon Length Scales

The surface plasmon wavelength is inversely proportional with the real part of the surface plasmon wavevector as shown below.

$$\lambda_{sp} = \frac{2\pi}{k'_{sp}} = \lambda_0 \sqrt{\frac{\varepsilon_d + \varepsilon(\omega)'}{\varepsilon_d \varepsilon(\omega)'}} \tag{2.11}$$

where the dielectric constant of the metal is a complex quantity, $\varepsilon(\omega) = \varepsilon(\omega)' - j\varepsilon(\omega)''$. Figure 2.5 - (a) shows the ratio of the surface plasmon wavelength to the free space wavelength as a function of the free space wavelength, λ_0 and it implies that the surface plasmon wavelength is always slightly less than the free space wavelength and this shows the bounding nature of the surface plasmon modes on the planar surface [5].

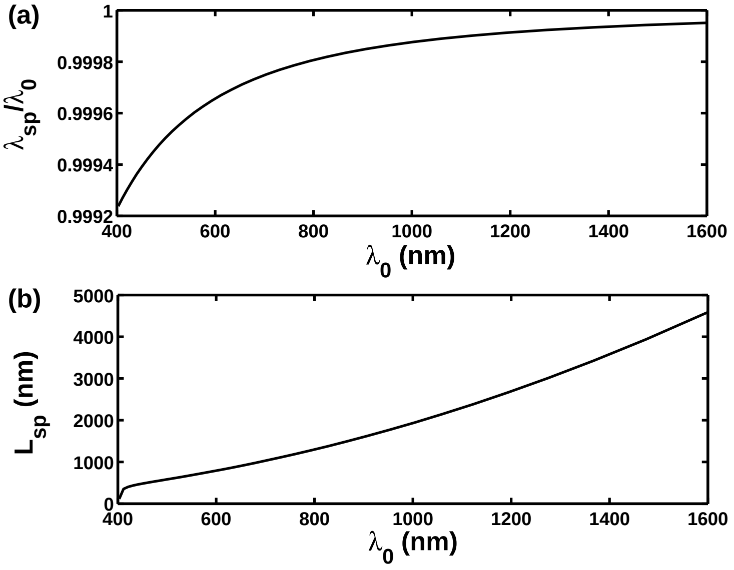

Figure 2.5: (a) Normalized surface plasmon wavelength as a function of the free space wavelength. (b) Surface plasmon propagation length as a function of the wavelength of the incident light wave in free space. The corresponding parameters are $\omega_p/2\pi = 12 \times 10^{15}$ Hz (7.9 eV), $\Gamma = 1.45 \times 10^{13}$ Hz (0.06 eV) and $\varepsilon_d = 1$.

The surface plasmon propagation length is the distance, the surface plasmon travels before its intensity diminished by the factor of e^2 and found by taking the imaginary part of the surface plasmon wavevector [4].

$$L_{sp} = \frac{1}{2k''_{sp}} = \frac{\lambda_0}{2\pi} \frac{\varepsilon(\omega)'^2}{\varepsilon(\omega)''} (\frac{\varepsilon(\omega)' + \varepsilon_d}{\varepsilon(\omega)'\varepsilon_d})^{\frac{3}{2}} \tag{2.12}$$

The surface plasmon propagation length can be approximated as below if $|\varepsilon(\omega)'| \gg |\varepsilon_d|$.

$$L_{sp} = \frac{\lambda_0}{2\pi} \frac{\varepsilon(\omega)'^2}{\varepsilon(\omega)''} \tag{2.13}$$

From figure 2.5 - (b), it can be inferred that for a long surface plasmon propagation length, metal must have a dielectric constant with a high and negative real part and a small imaginary part. The surface plasmon propagation length can be seen as the upper limit size for the subwavelength photonic components.

The total wavevector of the light of free space wavevector, k_0 in a system consisting of a dielectric medium which has a relative permittivity, ε_d and a metal medium which has a relative permittivity, $\varepsilon(\omega)$ is $\varepsilon_d k_0^2$ in the dielectric medium and $\varepsilon(\omega)k_0^2$ in the metal medium. The relationship between the total wavevector and the normal component of the wavevector can be written in equation 2.14 [5].

$$\begin{aligned} \varepsilon_d k_0^2 &= k_{sp}^2 + (k_z^{(d)})^2 \\ \varepsilon(\omega) k_0^2 &= k_{sp}^2 + (k_z^{(m)})^2 \end{aligned} \tag{2.14}$$

As noted before, the surface plasmon wavevector is greater than the wavevector of free space in any medium, ($k_{sp}^2 \gg \varepsilon_d k_0^2$ and $k_{sp}^2 \gg \varepsilon(\omega) k_0^2$). Thus, the normal components of the fields in both dielectric and metal layers decay exponentially as depicted in figure 2.6.

Assuming that $|\varepsilon(\omega)'| \gg |\varepsilon(\omega)''|$ and substituting equation 2.7 into equation 2.14, the penetration depths into dielectric medium, L_d and metal medium, L_m are found in equation 2.15. In figures 2.7 - (a) and (b), the penetration depths in dielectric and metal layers as a function of free space wavelength is shown respectively.

$$\begin{aligned} L_d &= \frac{1}{k_0}\sqrt{\frac{|\varepsilon(\omega)' + \varepsilon_d|}{\varepsilon_d^2}} \\ L_m &= \frac{1}{k_0}\sqrt{\frac{|\varepsilon(\omega)' + \varepsilon_d|}{\varepsilon_m^2}} \end{aligned} \tag{2.15}$$

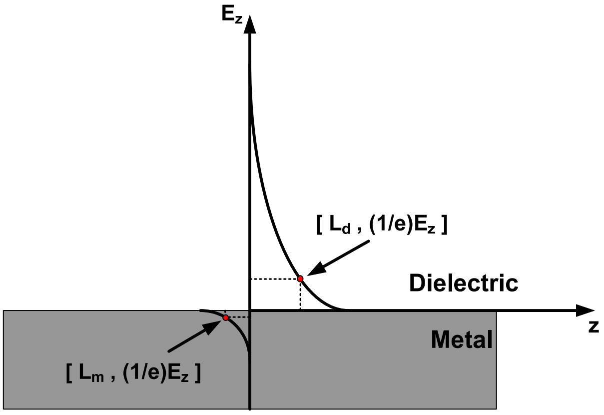

Figure 2.6: The falls in the normal component of the electric field (E_z) with the distance away from the surface between dielectric and metal media.

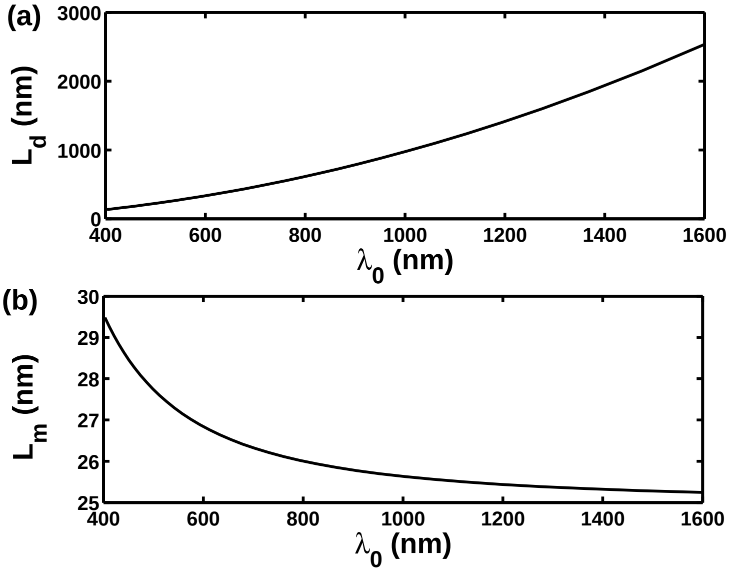

Figure 2.7: The penetration depth into (a) the dielectric medium and (b) the metal medium as a function of the free space wavelength. The corresponding parameters are $\omega_p/2\pi = 12 \times 10^{15}$ Hz (7.9 eV), $\Gamma = 1.45 \times 10^{13}$ Hz (0.06 eV) and $\varepsilon_d = 1$.

We see from figure 2.7 that while in the visible spectrum the penetration depth in the dielectric is less than the free space wavelength, in the infrared region it is more than free space wavelength. This increase in the penetration depth varying with the free space wavelength is due to fact that as the wavelength increases, the metal is better conductor and the surface plasmon mode has a wavevector that is closer to the free space wavevector. At this stage, it is more light-like and can less likely be confined to the surface [5]. The penetration depth of the field shows how the surface plasmon mode is sensitive to the changes in the dielectric region such as the presence of the prism at the metal surface. This sensitivity is due to the field enhancement at the interface.

The penetration depth into the metal gives us the measure of the thickness required for the metal films that allow coupling of surface plasmons to propagating light in the prism coupling geometry, the thickness of the films in the surface plasmon mediated transmission of light through metals and the thickness of the metal films where the surface plasmon modes on the two metal surfaces interact [5]. It also determines the size of the structure needed to control the surface plasmon. The penetration depth into metal limits the extent of the field enhancement.

2.4 Can TE Polarized Surface Plasmon Exist at an Interface between a Dielectric and a Metal Layer?

If the incident wave is TE (transverse electric) polarized, the fields of the structure depicted in figure 2.1 are written for the dielectric region ($z > 0$)

$$\begin{aligned} \mathbf{E}(r,t) &= \widehat{y}Ae^{-jk_x x - k_z^{(d)}z + j\omega t} \\ \mathbf{H}(r,t) &= (-A\frac{1}{j\mu_0\omega})(\widehat{x}k_z^{(d)} - \widehat{z}jk_x)e^{-jk_x x - k_z^{(d)}z + j\omega t} \end{aligned} \tag{2.16}$$

and for the metal region ($z < 0$)

$$\begin{aligned} \mathbf{E}(r,t) &= \widehat{y}Be^{-jk_x x + k_z^{(m)}z + j\omega t} \\ \mathbf{H}(r,t) &= (-B\frac{1}{j\mu_0\omega})(-\widehat{x}k_z^{(m)} - \widehat{z}jk_x)e^{-jk_x x + k_z^{(m)}z + j\omega t} \end{aligned} \tag{2.17}$$

Using the corresponding boundary conditions, the following equalities are found.

$$A = B, \qquad Ak_z^{(d)} = -Bk_z^{(m)} \tag{2.18}$$

From equation 2.18, the following relation is found.

$$(k_z^{(d)} + k_z^{(m)})A = 0 \tag{2.19}$$

In order that equations 2.16 and 2.17 describe a surface electromagnetic wave, $k_z^{(d)}$ and $k_z^{(m)}$ must be real and positive. Hence, the only solution for equation 2.19 is $A = 0$ so that $B = 0$. Therefore, TE polarized incident wave cannot excite the surface plasmons in the structure depicted in figure 2.1.

2.5 Surface Plasmon on two Sides of a Metal Layer

To examine the properties of the surface plasmons on the surface of metal films, we consider a structure consisting of air characterized by the dielectric constant $\varepsilon_d = 1$ at $z > d$, a metal film characterized by a complex, frequency dependent dielectric function $\varepsilon(\omega)$ at $0 < z < d$ and a dielectric medium characterized by real and positive dielectric constatnt ε_s at $z < 0$ as shown in figure 2.8.

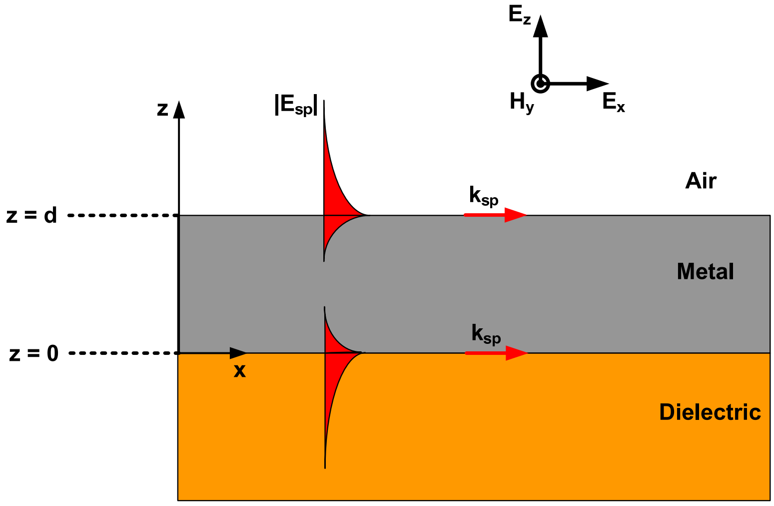

Figure 2.8: Surface plasmons excited on the two interfaces between a metal and two dielectric media.

The magnetic field localized on each surface can be written as

$$\begin{aligned} \mathbf{H}(r,t) &= \widehat{y}Ae^{-jk_x x - k_z^{(d)} z + j\omega t} && z \geq d \\ &= \widehat{y}e^{-jk_x x}[Be^{k_z^{(m)} z} + Ce^{-k_z^{(m)} z}]e^{+j\omega t} && 0 \leq z \leq d \\ &= \widehat{y}De^{-jk_x x + k_z^{(s)} z + j\omega t} && z \leq 0 \end{aligned} \tag{2.20}$$

where

$$\begin{aligned} k_z^{(d)} &= [k_x^2 - \varepsilon_d(\omega/c)^2]^{\frac{1}{2}} \\ k_z^{(s)} &= [k_x^2 - \varepsilon_s(\omega/c)^2]^{\frac{1}{2}} \end{aligned} \tag{2.21}$$

Assuming that there is no charge and current source, the boundary conditions indicating that the tangential components of the magnetic field and the normal component of the displacement vector must be continuous at each interface yield the following.

$$\nabla \times \mathbf{H} = \frac{\partial \mathbf{D}}{\partial t} = \varepsilon_0 \varepsilon_r \frac{\partial \mathbf{E}}{\partial t} \Rightarrow \frac{1}{\varepsilon_0 \varepsilon_r} \frac{\partial \mathbf{H}}{\partial z} \text{ is continuous.} \tag{2.22}$$

At $z = d$, using boundary conditions, following relations are found.

$$\begin{aligned} A e^{-k_z^{(d)} d} &= B e^{k_z^{(m)} d} + C e^{-k_z^{(m)} d} \\ -\frac{1}{\varepsilon_d} A k_z^{(d)} e^{-k_z^{(d)} d} &= \frac{k_z^{(m)}}{\varepsilon(\omega)} [B e^{k_z^{(m)} d} - C e^{-k_z^{(m)} d}] \end{aligned} \tag{2.23}$$

and at $z = 0$

$$\begin{aligned} D &= B + C \\ \frac{k_z^{(s)}}{\varepsilon_s} D &= \frac{k_z^{(m)}}{\varepsilon(\omega)} [B - C] \end{aligned} \tag{2.24}$$

Using equations 2.23 and 2.24, the general condition for this system is found.

$$[\frac{\varepsilon(\omega)}{\varepsilon_d} \frac{k_z^{(d)}}{k_z^{(m)}} + 1][\frac{\varepsilon(\omega)}{\varepsilon_s} \frac{k_z^{(s)}}{k_z^{(m)}} + 1] = [\frac{\varepsilon(\omega)}{\varepsilon_d} \frac{k_z^{(d)}}{k_z^{(m)}} - 1][\frac{\varepsilon(\omega)}{\varepsilon_s} \frac{k_z^{(s)}}{k_z^{(m)}} - 1] e^{-2k_z^{(m)} d} \tag{2.25}$$

As $d \to \infty$, the dispersion relations for surface plasmons at the interfaces of air-metal and metal-dielectric are found.

$$\frac{\varepsilon(\omega)}{\varepsilon_d} \frac{k_z^{(d)}}{k_z^{(m)}} + 1 = 0, \qquad \frac{\varepsilon(\omega)}{\varepsilon_s} \frac{k_z^{(s)}}{k_z^{(m)}} + 1 = 0 \tag{2.26}$$

Two surface plasmons on each interfaces are affected by the interactions that one exerts to the other and the dispersion curve of each one is distorted by these interactions as shown in figure 2.9.

One special case of this phenomenon is that the top and bottom layers are air, $\varepsilon_d = \varepsilon_s = 1$, such that $k_d = k_s$. Using equation 2.25, the following result is found.

$$\begin{aligned} [\varepsilon(\omega) \frac{k_z^{(d)}}{k_z^{(m)}} + 1] &= \pm[\varepsilon(\omega) \frac{k_z^{(d)}}{k_z^{(m)}} - 1] e^{-k_z^{(m)} d} \Rightarrow \varepsilon(\omega) \frac{k_z^{(d)}}{k_z^{(m)}} = -\frac{1 \pm e^{-k_z^{(m)} d}}{1 \mp e^{-k_z^{(m)} d}} \\ \Rightarrow \quad \varepsilon(\omega) \frac{k_z^{(d)}}{k_z^{(m)}} &= -\frac{e^{-k_z^{(m)} d/2} (e^{+k_z^{(m)} d/2} \pm e^{-k_z^{(m)} d/2})}{e^{-k_z^{(m)} d/2} (e^{+k_z^{(m)} d/2} \mp e^{-k_z^{(m)} d/2})} \end{aligned} \tag{2.27}$$

After arranging some terms, equation 2.27 turns into equation 2.28.

$$\begin{aligned} \varepsilon(\omega) \frac{k_z^{(d)}}{k_z^{(m)}} &= -\coth(\frac{1}{2} k_z^{(m)} d) \\ \varepsilon(\omega) \frac{k_z^{(d)}}{k_z^{(m)}} &= -\tanh(\frac{1}{2} k_z^{(m)} d) \end{aligned} \tag{2.28}$$

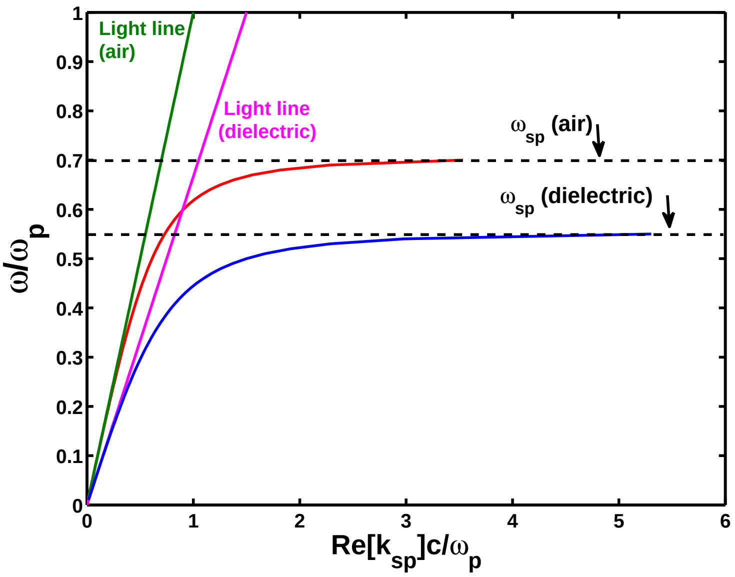

Figure 2.9: Dispersion curves of the surface plasmons at the interfaces of air-metal film and metal film-dielectric medium. The corresponding parameters are $\omega_p/2\pi = 12 \times 10^{15}$ Hz (7.9 eV), $\Gamma = 1.45 \times 10^{13}$ Hz (0.06 eV), $d = 30$ nm, $\varepsilon_d = 1$ and $\varepsilon_s = 2.25$.

The first and second parts of equation 2.28 correspond to the surface plasmon modes in which the tangential component of the electric field (E_x) is an even and odd functions of $z-d/2$ respectively [4]. For large wavevectors, the frequencies of the surface plasmon modes for the first and second parts of equation 2.28 can be written as below respectively.

$$\begin{aligned} \omega_- &= \frac{\omega_p}{\sqrt{2}}(1 - e^{-|k_x|d})^{\frac{1}{2}} \\ \omega_+ &= \frac{\omega_p}{\sqrt{2}}(1 + e^{-|k_x|d})^{\frac{1}{2}} \end{aligned} \tag{2.29}$$

If the metal film is very thin, the electromagnetic interaction between two surface plasmons cannot be neglected. The imaginary part of the wavevector which determines the propagation length of the high frequency (ω_+) surface plasmon mode is inversely proportional with the film thickness, d. This kind of surface plasmon propagation length is very long and called long-range surface plasmon and this leads to a large field enhancement. The imaginary part of the wavevector which determines the propagation length of the low frequency (ω_-) surface plasmon mode is proportional with the film thickness, d.

The reason for this longer propagation length compared to the shorter propagation length is that the tangential component of the electric field E_x of the former surface plasmon mode vanishes at the midplane of the film, $z = d/2$, while it reaches its maximum value at that plane for the latter mode. The mode with the smaller fraction of its electric field inside the film has the longer propagation length because it interacts more weakly with the dissipative mechanisms in the film [4].

Chapter 3

EXCITATION OF SURFACE PLASMONS

3.1 Introduction

In this chapter, the reflection and transmission coefficients of TE and TM polarized waves incident from one layer to another have been derived. The reflection coefficient of the wave which propagates with an incident angle greater than the critical angle defined between two layers will be discussed. The excitation of surface plasmons using a three-layered medium has been analyzed. The angle dependent reflectivity behavior of the three-layered medium has been shown.

3.2 Reflection and Transmission Coefficients of a TM Polarized Wave Propagating Between Two Layers

Consider a TM polarized wave that propagates through the structure consisting of two media as shown in figure 3.1.

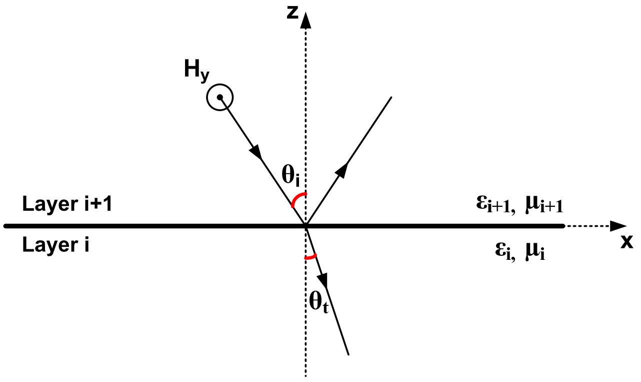

Figure 3.1: TM polarized wave at an interface between two media.

We write the magnetic field of the TM polarized wave in two layers as in equation 3.1.

$$\begin{aligned} \mathbf{H}_{i+1} &= \widehat{y}(H_{i+1}^{+}e^{-jk_z^{(i+1)}z-jk_x^{(i+1)}x} + H_{i+1}^{-}e^{+jk_z^{(i+1)}z-jk_x^{(i+1)}x}) \\ \mathbf{H}_{i} &= \widehat{y}(H_{i}^{+}e^{-jk_z^{(i)}z-jk_x^{(i)}x} + H_{i}^{-}e^{+jk_z^{(i)}z-jk_x^{(i)}x}) \end{aligned} \tag{3.1}$$

Defining $R^{TM}_{i+1,i}$ and $T^{TM}_{i+1,i}$ as the reflection and transmission coefficients of the TM polarized wave from layer i+1 to i respectively and H_0 is the amplitude of the incident wave, the amplitude of the magnetic field in each medium can be written below.[1]

$$\begin{aligned} H^-_{i+1} = H_0, \quad H^+_{i+1} = R^{TM}_{i+1,i}H_0 \\ H^+_i = 0, \quad H^-_i = T^{TM}_{i+1,i}H_0 \end{aligned} \tag{3.2}$$

Substituting equation 3.2 into 3.1, we get the magnetic fields of TM polarized wave in two media as

$$\begin{aligned} \mathbf{H}_{i+1} &= \widehat{y}H_0 e^{-jk_x^{(i+1)}x}(e^{+jk_z^{(i+1)}z} + R^{TM}_{i+1,i}e^{-jk_z^{(i+1)}z}) \\ \mathbf{H}_i &= \widehat{y}T^{TM}_{i+1,i}H_0 e^{-jk_x^{(i)}x}e^{+jk_z^{(i)}z} \end{aligned} \tag{3.3}$$

Substituting equation 3.3 into the Maxwell's curl equation (equation 3.4), we get the electric fields of TM polarized wave (equation 3.5).

$$\nabla \times \mathbf{H} = j\omega\varepsilon_0\varepsilon_r\mathbf{E} \tag{3.4}$$

$$\begin{aligned} \mathbf{E}_{i+1} &= \frac{H_0 e^{-jk_x^{(i+1)}x}}{j\omega\varepsilon_0\varepsilon_{i+1}}([-\widehat{z}jk_x^{(i+1)} - \widehat{x}jk_z^{(i+1)}]e^{jk_z^{(i+1)}z} + [-\widehat{z}jk_x^{(i+1)} + \widehat{x}jk_z^{(i+1)}]R^{TM}_{i+1,i}e^{-jk_z^{(i+1)}z}) \\ \mathbf{E}_i &= \frac{T^{TM}_{i+1,i}H_0 e^{-jk_x^{(i)}x}}{j\omega\varepsilon_0\varepsilon_i}[-\widehat{z}jk_x^{(i)} - \widehat{x}jk_z^{(i)}]e^{jk_z^{(i)}z} \end{aligned} \tag{3.5}$$

The boundary condition implying that the tangential components (x and y) of the electric and magnetic fields are continuous yields the following.

$$\begin{aligned} 1 + R^{TM}_{i+1,i} &= T^{TM}_{i+1,i} \\ \frac{k_z^{(i+1)}}{\varepsilon_{i+1}}(1 - R^{TM}_{i+1,i}) &= \frac{k_z^{(i)}}{\varepsilon_i}T^{TM}_{i+1,i} \end{aligned} \tag{3.6}$$

Hence, we get the reflection coefficient of the TM polarized wave propagating in the structure depicted in figure 3.1 as

$$R^{TM}_{i+1,i} = \frac{k_z^{(i+1)}\varepsilon_i - k_z^{(i)}\varepsilon_{i+1}}{k_z^{(i+1)}\varepsilon_i + k_z^{(i)}\varepsilon_{i+1}} \tag{3.7}$$

Using the geometry of figure 3.1, we can write the following relationship.

$$\begin{aligned} k_x^{(i+1)} = k_{i+1}\sin(\theta_i), \quad k_z^{(i+1)} = k_{i+1}\cos(\theta_i) \\ k_x^{(i)} = k_i\sin(\theta_i), \qquad k_z^{(i)} = k_i\cos(\theta_t) \end{aligned} \tag{3.8}$$

---

[1] The layers have infinite thickness so there is no reflection from the boundaries.

where $k_{i+1} = k_0\sqrt{\varepsilon_{i+1}}$ and $k_i = k_0\sqrt{\varepsilon_i}$ and from the phase matching condition, we can write

$$k_x^{(i+1)} = k_x^{(i)} \Rightarrow \frac{\sin(\theta_i)}{\sin(\theta_t)} = \sqrt{\frac{\varepsilon_i}{\varepsilon_{i+1}}} \tag{3.9}$$

Using equations 3.8 and 3.9, the reflection coefficient depicted in equation 3.7 becomes

$$R^{TM}_{i+1,i} = \frac{\sqrt{\varepsilon_{i+1}}\varepsilon_i\cos(\theta_i) - \sqrt{\varepsilon_i}\varepsilon_{i+1}\cos(\theta_t)}{\sqrt{\varepsilon_{i+1}}\varepsilon_i\cos(\theta_i) + \sqrt{\varepsilon_i}\varepsilon_{i+1}\cos(\theta_t)} \tag{3.10}$$

Equation 3.9 yields the following.

$$\begin{aligned}\frac{\sin(\theta_i)^2}{\sin(\theta_t)^2} = \frac{\varepsilon_i}{\varepsilon_{i+1}} \quad &\Rightarrow \quad \sin(\theta_t)^2 = 1 - \cos(\theta_t)^2 \\ \cos(\theta_t) \quad &= \quad \sqrt{1 - \frac{\varepsilon_{i+1}}{\varepsilon_i}\sin(\theta_i)^2} \qquad (3.11)\end{aligned}$$

Thus, the reflection coefficient of the TM polarized wave as a function of the incident angle, θ_i is found in equation 3.12.

$$R^{TM}_{i+1,i} = \frac{\cos(\theta_i) - \sqrt{\frac{\varepsilon_{i+1}}{\varepsilon_i}}\sqrt{1 - \frac{\varepsilon_{i+1}}{\varepsilon_i}\sin(\theta_i)^2}}{\cos(\theta_i) + \sqrt{\frac{\varepsilon_{i+1}}{\varepsilon_i}}\sqrt{1 - \frac{\varepsilon_{i+1}}{\varepsilon_i}\sin(\theta_i)^2}} \tag{3.12}$$

3.3 Reflection and Transmission Coefficients of a TE Polarized Wave Propagating Between Two Layers

Consider a TE polarized wave that propagates through the structure consisting of two media as shown in figure 3.2.

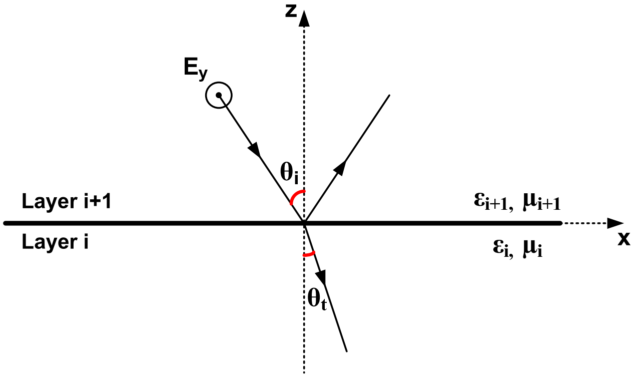

Figure 3.2: TE polarized wave at an interface between two media.

We write the electric field of the TE polarized wave in two layers as in equation 3.13.

$$\begin{aligned}\mathbf{E}_{i+1} &= \widehat{y}(E^+_{i+1}e^{-jk_z^{(i+1)}z - jk_x^{(i+1)}x} + E^-_{i+1}e^{+jk_z^{(i+1)}z - jk_x^{(i+1)}x}) \\ \mathbf{E}_i &= \widehat{y}(E^+_i e^{-jk_z^{(i)}z - jk_x^{(i)}x} + E^-_i e^{+jk_z^{(i)}z - jk_x^{(i)}x})\end{aligned} \tag{3.13}$$

Defining $R^{TE}_{i+1,i}$ and $T^{TE}_{i+1,i}$ as the reflection and transmission coefficients of the TE polarized wave from layer i+1 to i respectively and E_0 is the amplitude of the incident wave, the amplitude of the electric field in each medium can be written below.

$$\begin{aligned} E^-_{i+1} = E_0, \quad E^+_{i+1} = R^{TE}_{i+1,i}E_0 \\ E^+_i = 0, \quad E^-_i = T^{TE}_{i+1,i}E_0 \end{aligned} \tag{3.14}$$

Substituting equation 3.14 into 3.13, we get the electric fields of TE polarized wave in two media as

$$\begin{aligned} \mathbf{E}_{i+1} &= \widehat{y}E_0 e^{-jk_x^{(i+1)}x}(e^{+jk_z^{(i+1)}z} + R^{TE}_{i+1,i}e^{-jk_z^{(i+1)}z}) \\ \mathbf{E}_i &= \widehat{y}T^{TE}_{i+1,i}E_0 e^{-jk_x^{(i)}x}e^{+jk_z^{(i)}z} \end{aligned} \tag{3.15}$$

Substituting equation 3.15 into the Maxwell's curl equation (equation 3.16), we get the magnetic fields of TE polarized wave (equation 3.17).

$$\nabla \times \mathbf{E} = -j\omega\mu_0\mathbf{H} \tag{3.16}$$

$$\begin{aligned} \mathbf{H}_{i+1} &= -\frac{E_0 e^{-jk_x^{(i+1)}x}}{j\omega\mu_0}([-\widehat{z}jk_x^{(i+1)} - \widehat{x}jk_z^{(i+1)}]e^{jk_z^{(i+1)}z} + [-\widehat{z}jk_x^{(i+1)} + \widehat{x}jk_z^{(i+1)}]R^{TE}_{i+1,i}e^{-jk_z^{(i+1)}z}) \\ \mathbf{H}_i &= -\frac{T^{TE}_{i+1,i}E_0 e^{-jk_x^{(i)}x}}{j\omega\mu_0}(-\widehat{z}jk_x^{(i)} - \widehat{x}jk_z^{(i)})e^{jk_z^{(i)}z} \end{aligned} \tag{3.17}$$

The boundary condition implying that the tangential components (x and y) of the electric and magnetic fields are continuous yields the following.

$$\begin{aligned} 1 + R^{TE}_{i+1,i} &= T^{TE}_{i+1,i} \\ k_z^{(i+1)}(1 - R^{TE}_{i+1,i}) &= k_z^{(i)}T^{TE}_{i+1,i} \end{aligned} \tag{3.18}$$

Hence, we get the reflection coefficient of the TE polarized wave propagating in the structure depicted in figure 3.2 as

$$R^{TE}_{i+1,i} = \frac{k_z^{(i+1)} - k_z^{(i)}}{k_z^{(i+1)} + k_z^{(i)}} \tag{3.19}$$

Using the geometry of figure 3.2, we can write the reflection coefficient of the TE polarized wave as a function of the incident angle, θ_i as in equation 3.20.

$$R^{TE}_{i+1,i} = \frac{\sqrt{\varepsilon_{i+1}}\cos(\theta_i) - \sqrt{\varepsilon_i}\sqrt{1 - \frac{\varepsilon_{i+1}}{\varepsilon_i}\sin(\theta_i)^2}}{\sqrt{\varepsilon_{i+1}}\cos(\theta_i) + \sqrt{\varepsilon_i}\sqrt{1 - \frac{\varepsilon_{i+1}}{\varepsilon_i}\sin(\theta_i)^2}} \tag{3.20}$$

If we plot the reflection coefficient of the TM and TE polarized wave as a function of the angle of incidence, we get the following figure.

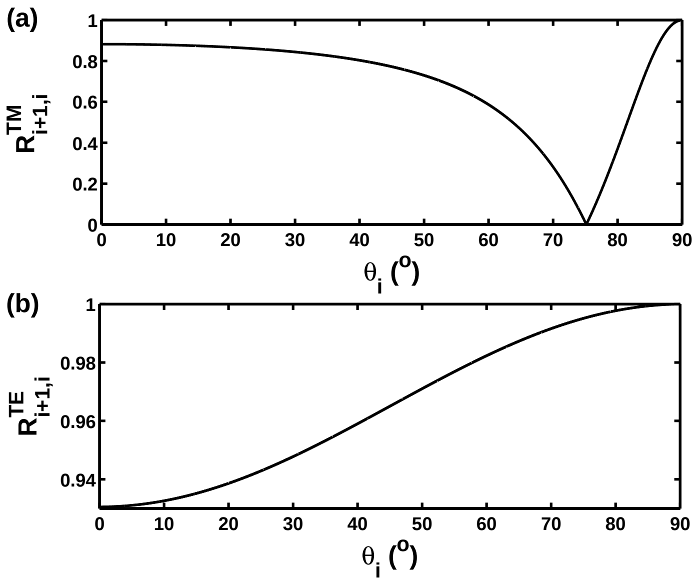

Figure 3.3: Reflection coefficient of (a) TM and (b) TE polarized wave as a function of the angle of incidence. The corresponding parameters are $\varepsilon_{i+1} = 1$ and $\varepsilon_i = -16.12 - j0.09$.

3.4 Reflection Coefficient of the Wave Propagating at an Angle Greater than the Critical Angle

When a wave is incident from one medium to another, it obeys the Snell's law shown in equation below.

$$\sqrt{\varepsilon_{i+1}}\sin(\theta_i) = \sqrt{\varepsilon_i}\sin(\theta_t) \tag{3.21}$$

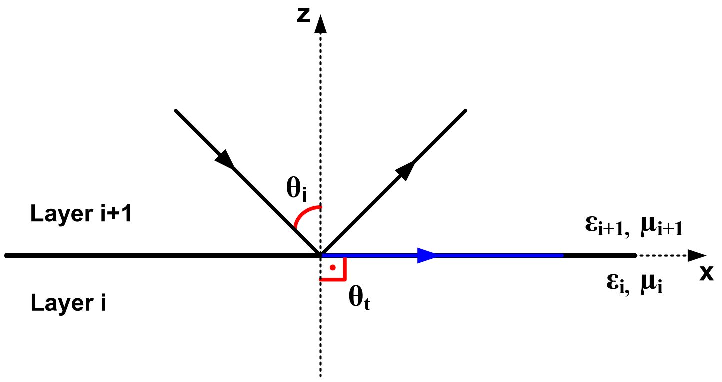

Figure 3.4: Wave propagating at an angle greater than the critical angle defined between two media.

When $\varepsilon_{i+1} \gg \varepsilon_i$, a critical angle is defined as the angle that makes the transmission angle, θ_t ,$\pi/2$ such that there is no transmission from layer i+1 to i.

$$\theta_c = \theta_i \Rightarrow \theta_t = \pi/2 \Rightarrow \theta_c = sin^{-1}(\sqrt{\frac{\varepsilon_i}{\varepsilon_{i+1}}}) \tag{3.22}$$

If the incident angle is greater than the critical angle, from the Snell's law

$$\sin(\theta_i) > \sin(\theta_c) = \sqrt{\frac{\varepsilon_i}{\varepsilon_{i+1}}} \Rightarrow \sin(\theta_t) > 1 \tag{3.23}$$

This inequality satisfies only complex solutions of θ_t. Hence, we write the propagation vector of the transmitted wave as

$$k_i = \widehat{x}k_x^{(i)} - \widehat{z}k_z^{(i)} \tag{3.24}$$

From phase matching condition, we write

$$\begin{aligned} k_x^{(i)} &= k_i \sin(\theta_t) \\ k_z^{(i)} &= k_i \cos(\theta_t) \\ \cos(\theta_t) &= \sqrt{1-\sin(\theta_t)^2} = \sqrt{1-\frac{\varepsilon_{i+1}}{\varepsilon_i}\sin(\theta_i)^2} \end{aligned} \tag{3.25}$$

Thus, we get

$$\begin{aligned} k_z^{(i)} &= k_i \cos(\theta_t) = k_0\sqrt{\varepsilon_i}\sqrt{1-\frac{\varepsilon_{i+1}}{\varepsilon_i}\sin(\theta_i)^2} \\ &= k_0\sqrt{\varepsilon_{i+1}}\sqrt{\frac{\varepsilon_i}{\varepsilon_{i+1}}-\sin(\theta_i)^2} = jk_{i+1}\sqrt{\sin(\theta_i)^2-\frac{\varepsilon_i}{\varepsilon_{i+1}}} \end{aligned} \tag{3.26}$$

After finding the wavevectors, we write the magnetic field of the TM polarized wave in each medium as

$$\begin{aligned} \mathbf{H}_{i+1} &= \widehat{y}H_0 e^{-jk_{i+1}\sin(\theta_i)x}(e^{jk_{i+1}\cos(\theta_i)z} + R_{i+1,i}^{TM}e^{-jk_{i+1}\cos(\theta_i)z}) \\ \mathbf{H}_i &= \widehat{y}T_{i+1,i}^{TM}H_0 e^{-jk_{i+1}\sin(\theta_i)x}e^{-k_{i+1}(\sqrt{\sin(\theta_i)^2-\frac{\varepsilon_i}{\varepsilon_{i+1}}})z} \end{aligned} \tag{3.27}$$

and the electric field of the TM polarized wave in each medium as

$$\begin{aligned} \mathbf{E}_{i+1} &= \frac{H_0 e^{-jk_{i+1}\sin(\theta_i)x}}{j\omega\varepsilon_0\varepsilon_{i+1}}([-\widehat{z}jk_{i+1}\sin(\theta_i) - \widehat{x}jk_{i+1}\cos(\theta_i)]e^{jk_{i+1}\cos(\theta_i)z} \\ &+ [-\widehat{z}jk_{i+1}\sin(\theta_i) + \widehat{x}jk_{i+1}\cos(\theta_i)]R_{i+1,i}^{TM}e^{-jk_{i+1}\cos(\theta_i)z}) \\ \mathbf{E}_i &= \frac{T_{i+1,i}^{TM}H_0 e^{-jk_{i+1}\sin(\theta_i)x}}{j\omega\varepsilon_0\varepsilon_i}(-\widehat{z}jk_{i+1}\sin(\theta_i) + \widehat{x}k_{i+1}\sqrt{\sin(\theta_i)^2-\frac{\varepsilon_i}{\varepsilon_{i+1}}}) \\ &\times \; e^{-k_{i+1}(\sqrt{\sin(\theta_i)^2-\frac{\varepsilon_i}{\varepsilon_{i+1}}})z} \end{aligned} \tag{3.28}$$

Looking at the field equations, we can say that the field in layer i is evanescent when $\varepsilon_{i+1} \gg \varepsilon_i$ and the incident angle is greater than the critical angle defined between layers i+1 and i.

Hence, the reflection coefficients of TE and TM polarized waves are calculated as

$$\begin{aligned} R^{TE}_{i+1,i} &= \frac{\cos(\theta_i) - j\sqrt{\sin(\theta_i)^2 - \frac{\varepsilon_i}{\varepsilon_{i+1}}}}{\cos(\theta_i) + j\sqrt{\sin(\theta_i)^2 - \frac{\varepsilon_i}{\varepsilon_{i+1}}}} \\ R^{TM}_{i+1,i} &= \frac{\varepsilon_i\cos(\theta_i) - j\varepsilon_{i+1}\sqrt{\sin(\theta_i)^2 - \frac{\varepsilon_i}{\varepsilon_{i+1}}}}{\varepsilon_i\cos(\theta_i) + j\varepsilon_{i+1}\sqrt{\sin(\theta_i)^2 - \frac{\varepsilon_i}{\varepsilon_{i+1}}}} \end{aligned} \tag{3.29}$$

We define the reflectivity as the square of the magnitude of the reflection coefficient, $|R|^2$. In figure 3.5, the reflectivity of both TM and TE cases is plotted.

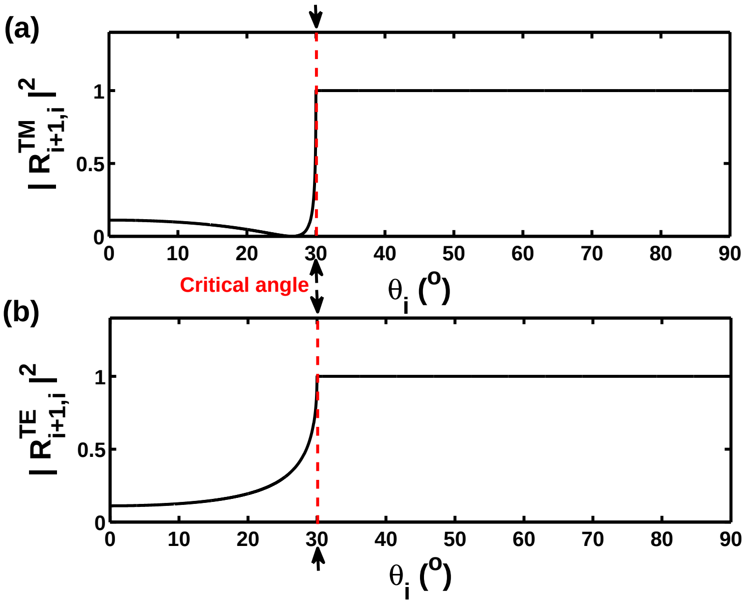

Figure 3.5: Reflectivity for (a) TM and (b) TE case. The corresponding parameters are $\varepsilon_{i+1} = 4$ and $\varepsilon_i = 1$.

3.5 Excitation of Surface Plasmon

We use a simple demonstration of a three-layered medium where the upper layer is dielectric characterized by a dielectric constant $\varepsilon_{(2)}$, the middle layer is air characterized by a dielectric constant $\varepsilon_{(1)}$ and the bottom layer is metal characterized by a dielectric constant $\varepsilon_{(0)}$ as shown in figure 3.6. The idea is that in the upper layer, we use a TM polarized wave that propagates at an angle greater than the critical angle defined between layers 2 and 1 resulting in an evanescent field in the middle layer and this evanescent field excites the surface plasmon on the surface of the metal.[2]

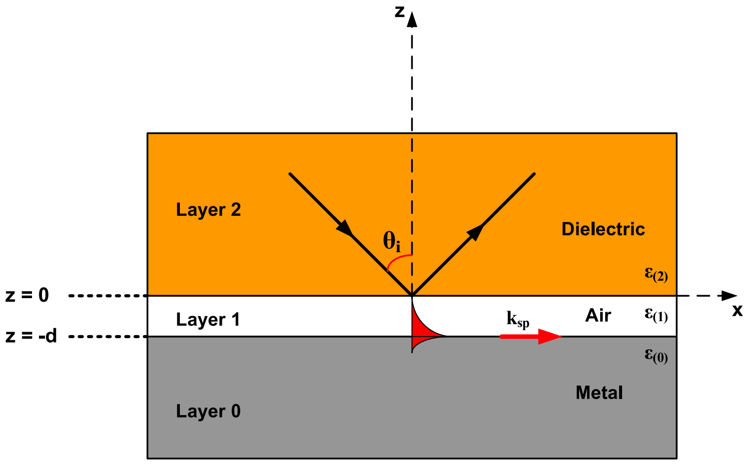

Figure 3.6: Three-layer structure used to excite the surface plasmon on the surface of the metal.

For layer 2, we can write the magnetic field of the TM polarized wave as below.

$$\mathbf{H}_{(2)} = \widehat{y}e^{-jk_x^{(2)}x}(A_{(2)}e^{jk_z^{(2)}z} + B_{(2)}e^{-jk_z^{(2)}z}) \tag{3.30}$$

In this equation, the unknown amplitude $B_{(2)}$ is due to the multiple reflections from the interface between layer 1 and layer 2 as depicted in figure 3.7. Thus, the generalized reflection coefficient at the interface is defined as the ratio of the sum of the reflected wave to the incident wave in layer 2, $\widetilde{R}_{2,1}^{TM} = B_{(2)}/A_{(2)}$. Using the definition of the generalized reflection coefficient, equation 3.30 becomes

$$\mathbf{H}_{(2)} = \widehat{y}A_{(2)}e^{-jk_x^{(2)}x}(e^{jk_z^{(2)}z} + \widetilde{R}_{2,1}^{TM}e^{-jk_z^{(2)}z}) \tag{3.31}$$

We can write the magnetic field in the middle layer as

$$\mathbf{H}_{(1)} = \widehat{y}A_{(1)}e^{-jk_x^{(1)}x}(e^{jk_z^{(1)}z} + R_{1,0}^{TM}e^{-jk_z^{(1)}(z+2d)}) \tag{3.32}$$

---

[2] In this structure, dielectric and metal layers are infinitely thick compare to the air gap. Hence, there is no reflection back from the top and bottom layers.

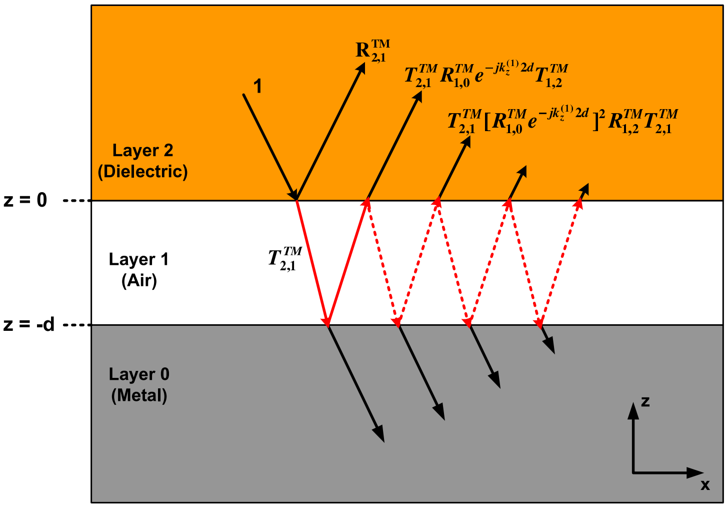

Figure 3.7: Multiple reflections in a tree-layered structure.

Assuming that $A_{(2)}$ is the user defined amplitude, we can find the amplitude $A_{(1)}$ in terms of $A_{(2)}$. Using the structure depicted in figure 3.7, we can write the expression of the amplitude transfer between layers 2 and 1 (at $z = 0$) for down-going waves.

$$A_{(1)} = A_{(2)} T_{2,1}^{TM} + A_{(1)} R_{1,0}^{TM} e^{-jk_z^{(1)}2d} R_{1,2}^{TM} \tag{3.33}$$

Hence, $A_{(1)}$ is found as

$$A_{(1)} = A_{(2)} \frac{T_{2,1}^{TM}}{1 - R_{1,0}^{TM} R_{1,2}^{TM} e^{-jk_z^{(1)}2d}} \tag{3.34}$$

We write the expression of the amplitude transfer between layer 2 and layer 1 for up-going waves as

$$A_{(2)} \widetilde{R}_{2,1}^{TM} = A_{(2)} R_{2,1}^{TM} + A_{(1)} R_{1,0}^{TM} e^{-jk_z^{(1)}2d} T_{1,2}^{TM} \tag{3.35}$$

Substituting equation 3.34 into 3.35, we get the generalized reflection coefficient as

$$\widetilde{R}_{2,1}^{TM} = R_{2,1}^{TM} + \frac{T_{2,1}^{TM} T_{1,2}^{TM} R_{1,0}^{TM} e^{-jk_z^{(1)}2d}}{1 - R_{1,0}^{TM} R_{1,2}^{TM} e^{-jk_z^{(1)}2d}} \tag{3.36}$$

We define the reflectivity as the square of the magnitude of the generalized reflection coefficient of the corresponding layers and plot $\widetilde{R}_{2,1}^{TM}$ as a function of the incident angle and for different gap thicknesses as shown in figure 3.8. For the angle of incidence, a clear resonance is observed around 31.5^o. For a small gap width, resonance is broadened due to the radiation damping of the surface plasmon. This is caused by the presence of the air layer which allows the surface plasmon to rapidly decay radiatively by transforming the evanescent surface plasmon field into a propagating field in the air. On the other hand, for a large gap width such that the surface plasmon can no longer be efficiently excited, the resonance vanishes.

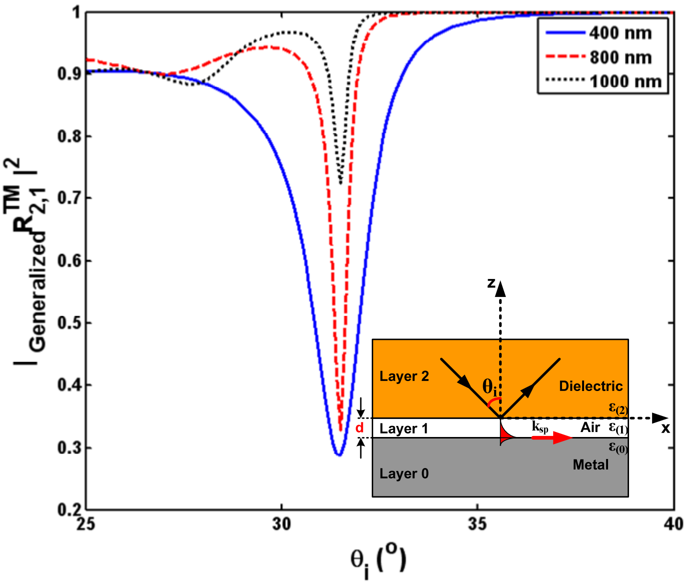

Figure 3.8: Reflectivity of the system depicted in figure 3.6. The reflectivity of the exciting beam is plotted as a function of the incident angle and for different air gaps. The corresponding parameters are $\varepsilon_{(2)} = 4$, $\varepsilon_{(1)} = 1$, $\varepsilon_{(0)} = -11.6 - 1.2j$ and the wavelength of the incident beam is 633 nm.

In the configuration depicted in figure 3.6, the tail of the evanescent wave at the interface between the dielectric and air layers is brought into contact with the interface between the air and metal layers that supports the surface plasmons. For a sufficiently large separation between the air and metal layers, the evanescent wave is only weakly influenced by the presence of the metal. By tuning the angle of incidence of the totally reflected beam inside the dielectric, the resonance condition for the excitation of the surface plasmon such that the matching of the parallel wave vector component can be fulfilled. The excitation of the surface plasmon will show up as a minimum in the reflected light.

The minimum in the reflectivity curve can have two physical reasons. The first reason is that the minimum occurs due to the destructive interference between the totally reflected light and the light emitted by the surface plasmon due to the radiation damping. The second reason is that the missing light is totally converted to the surface plasmons at the interface which carry away the energy along the interface such that it cannot reach the detector which detects the reflected light in the dielectric layer in the structure depicted in figure 3.6.

In figure 3.10, we show that our analytical calculations for the reflectivity of the three-layered system is well fitted with the result of the COMSOL Multiphysics simulation shown in figure 3.9 - (a).

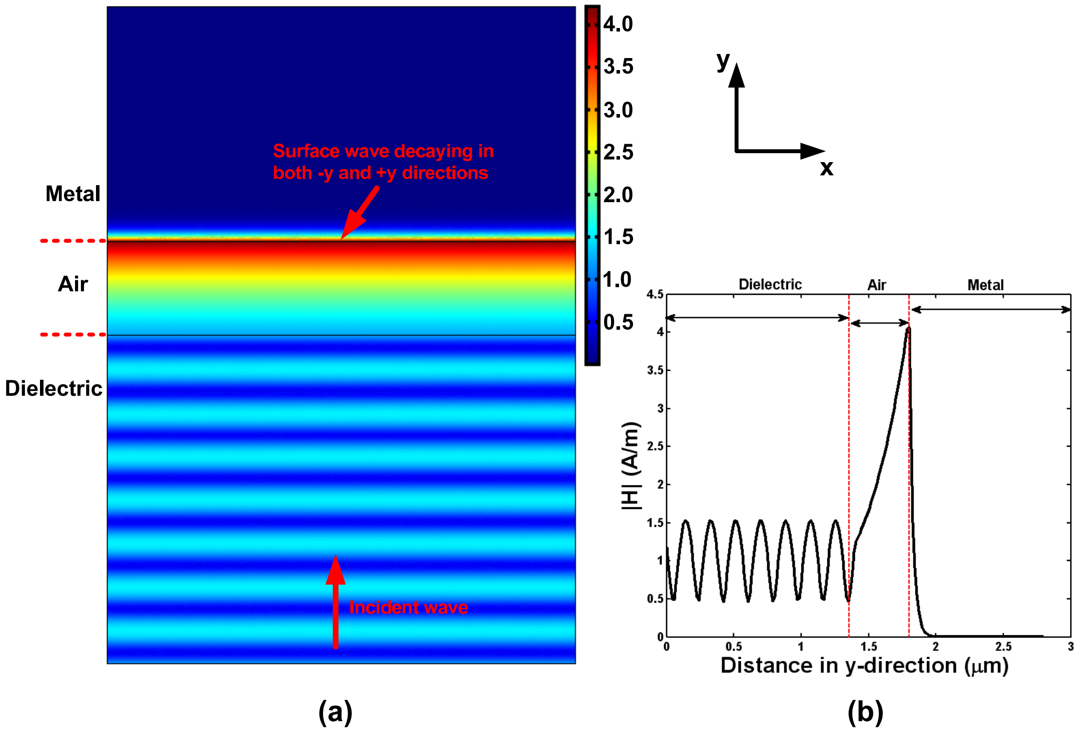

Figure 3.9: (a) COMSOL Multiphysics simulation of the three-layered system at the incident angle of 31.5^o, the angle at what the reflectivity of the system is minimum. (b) $|H|$ field distribution of the system as a function of the distance in y-direction. The corresponding parameters are $H_0 = 1$ [A/m], $\varepsilon_{(2)} = 4$, $\varepsilon_{(1)} = 1$, $\varepsilon_{(0)} = -11.6 - j1.2$, the wavelength of the incident wave is 633 nm and the thickness of the air gap is 400 nm.

To understand whether the wave on the surface of the metal is a surface plasmon or not, we look at the amplitude of the magnetic field in each layer as in figure 3.9 - (b) using COMSOL Multiphysics. Surface waves are the waves which are evanescent in both positive and negative directions normal to the surface of the metal. Notice that the wave on the surface of the metal decays both in $+y$ and $-y$ directions which means that it is a surface wave. Thus, we can say that using our three-layered structure, we excite the surface plasmon on the surface of the metal.

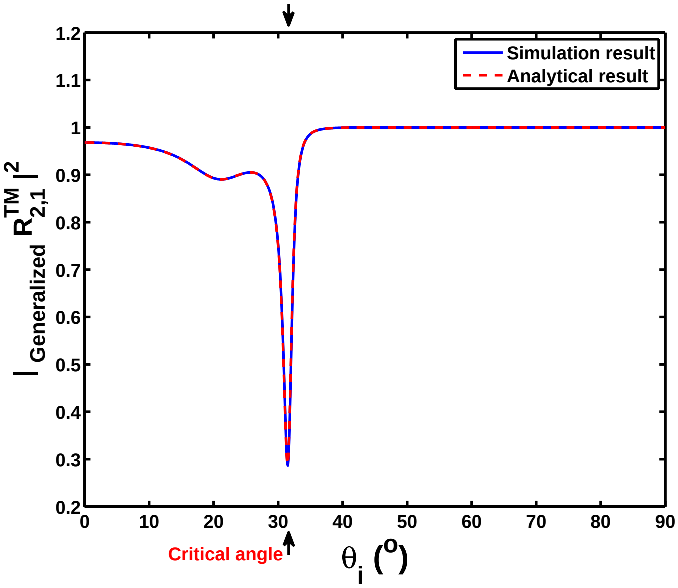

Figure 3.10: The comparison of the reflectivity graph of simulation and analytical results of the structure depicted in figure 3.6. The corresponding parameters are $\varepsilon_{(2)} = 4$, $\varepsilon_{(1)} = 1$, $\varepsilon_{(0)} = -11.6 - 1.2j$, the wavelength of the incident wave is 633 nm and the thickness of the air gap is 400 nm.

In figure 3.11, the magnitude of the tangential component of the wavectors at the interface between the air and metal layers one of which in the air layer, $k_x^{(2)}$ and the other in the metal layer, $k_x^{(1)}$ $(= k_{sp})$ at $z = -d$ are compared. It is shown that at the incident angle where the reflectivity of the three-layered structure is minimum, $k_x^{(1)}$ starts to exceed k_{sp} as seen in figure 3.11. Hence, this result coincides with the theory saying that for the surface plasmon excitation, the tangential component of the wavevector on the surface of the metal should be equal or greater than that of the surface plasmon.

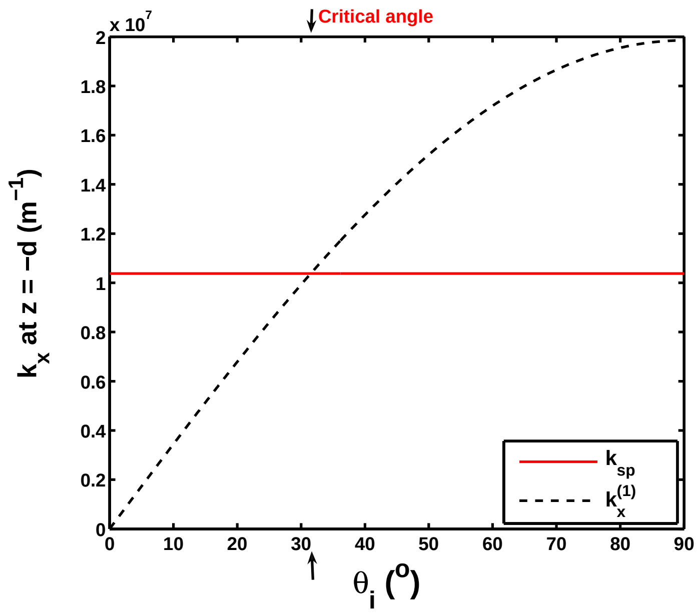

Figure 3.11: The comparison of the tangential component of the wavevector at the surface of the metal with that of the surface plasmon. The corresponding parameters are, $\varepsilon_{(1)} = 1$, $\varepsilon_{(0)} = -11.6 - 1.2j$ and the wavelength of the incident wave is 633 nm.

Chapter 4

EXCITATION OF SURFACE PLASMONS WITH LEFT HANDED MATERIALS

4.1 Introduction

In this chapter, we have used left handed materials to excite surface plasmon with TE waves instead of TM waves. The effects of the left handed materials on the surface plasmon propagation length have been discussed as well.

4.2 Left Handed Materials

Left handed materials have already been known since 1968 as the materials having electrodynamics properties of simultaneously negative values of dielectric permittivity, ε and magnetic permeability, μ. The choice of negative sign for both ε and μ does not cause the physical contradictions, in other words this does not change the classical expression for n [7].

$$n = \sqrt{\varepsilon\mu} \tag{4.1}$$

Simultaneously negative values of ε and μ are possible, but it differs from the electrodynamics of materials with positive ε and μ. From the Maxwell's curl equations, we can say that the vectors **E**, **H**, and **k** form a left-handed triplet of the vectors for negative ε and μ.

$$\begin{aligned} \nabla \times \mathbf{E} &= -\mu\frac{\partial \mathbf{H}}{\partial t} \\ \nabla \times \mathbf{H} &= \varepsilon\frac{\partial \mathbf{E}}{\partial t} \end{aligned} \tag{4.2}$$

If we look at the Poynting vector, $\mathbf{S} = \mathbf{E} \times \mathbf{H}$, it forms a right-handed triplet of the vectors together with the vectors **E** and **H**. The direction of the phase velocity, $\mathbf{v}_{ph}$ coincides with the direction of the wavevector **k**, while the direction of the group velocity, $\mathbf{v}_{gr}$ coincides with the direction of the vector **S**. Hence, the phase and the group velocities are antiparallel when ε and μ are simultaneously negative.

Antiparallel phase and group velocities also affect Snell's law as illustrated in figure 4.1.

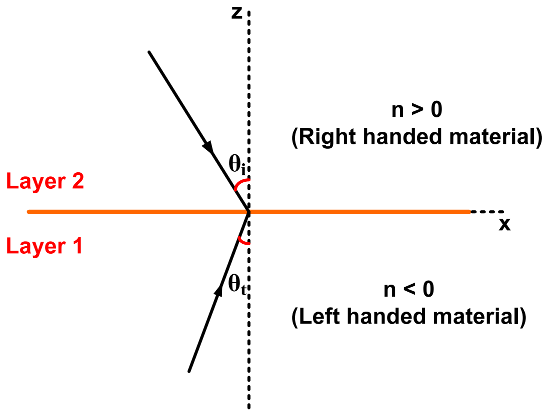

Figure 4.1: Snell's law for the left handed materials.

This unusual propagation of ray is a consequence of the opposite direction of the vectors, $\mathbf{v}_{ph}$ and $\mathbf{v}_{gr}$ and of the continuity of the tangential components of the wavevector on the interface between two media.

We can write the Snell's law as

$$\frac{\sin(\theta_i)}{\sin(\theta_t)} = \frac{n_{(1)}}{n_{(2)}} = \sqrt{\frac{\mu_{(1)}\varepsilon_{(1)}}{\mu_{(2)}\varepsilon_{(2)}}} \tag{4.3}$$

The index of refraction is negative when ε and μ are both negative. Hence, equation 4.1 becomes

$$n = \pm\sqrt{\varepsilon\mu} \tag{4.4}$$

In this equation, positive sign is used for the usual case whereas negative sign is used when ε and μ are both negative.

The complex nature of ε and μ

$$\begin{aligned} \varepsilon &= \varepsilon' - j\varepsilon'' \\ \mu &= \mu' - j\mu'' \end{aligned} \tag{4.5}$$

leads to a complex wavenumber, k

$$k = k' - jk'' \tag{4.6}$$

where

$$\begin{aligned} k' &\approx \frac{w}{c}\sqrt{\varepsilon'\mu'} \\ k'' &\approx \frac{1}{2}k'[\frac{\varepsilon''}{\varepsilon'} + \frac{\mu''}{\mu'}] \end{aligned} \tag{4.7}$$

For negative (ε', μ') and positive (ε'', μ''), k'' becomes negative which means the wave groves while propagating. If real parts of ε and μ change sign, k' changes its sign but k'' does not. The inverse motion of the sinusoidal wave for materials with negative refraction index changes the sign of Doppler effect as in figure 4.2. This phenomenon can be understood clearly from the formula of the classical Doppler effect.

$$\omega = \omega_0[1 - n\frac{v}{c}] \tag{4.8}$$

where ω is the observed frequency, ω_0 is the emitted frequency, c is the velocity of light, v is the velocity of an electron, and n is the index of refraction for the medium. For the usual materials when the receiver moves to the source, the observed frequency increases but for the left handed materials it decreases.

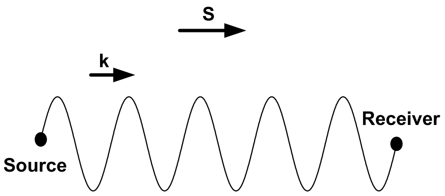

Right Handed Material

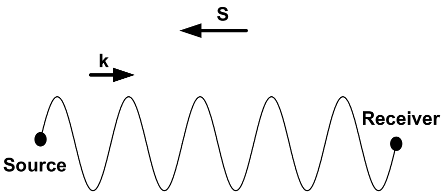

Left Handed Material

Figure 4.2: Poynting vector and wavevector for wave propagations in right-handed and left-handed materials.

The radiation coupling condition for Cherenkov effect is

$$\cos(\theta) = \frac{c}{vn} \tag{4.9}$$

where v is the particle velocity, n is the material index of refraction and θ is the angle between the particle trajectory and radiated photon. Therefore, when the index of refraction is negative, radiation goes backward while in usual case onward as depicted in figure 4.3.

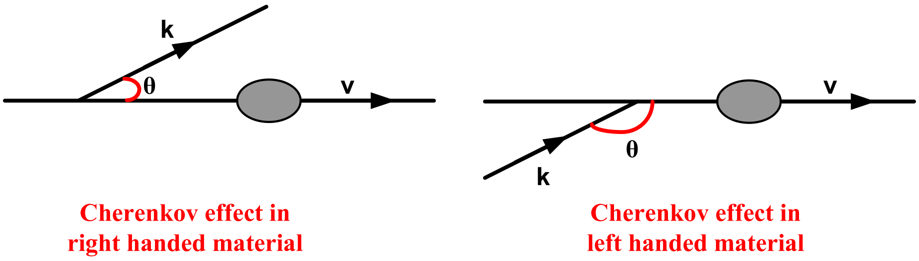

Figure 4.3: Cherenkov effect in right and left handed media.

Left handed materials are artificial materials and simultaneous negative permittivity and permeability can be done by designing periodic thin wire and split ring resonator structures in a composite system.

4.2.1 Periodic Thin Wire

The negative permittivity of the left handed material can be provided by the periodic thin wire structure as shown in the subfigure in figure 4.4. After detailed calculations, the effective dielectric function of this structure can be shown as [8]

$$\varepsilon_{eff} = 1 - \frac{\omega_p^2}{w(w - j\frac{\varepsilon_0 a^2 \omega_p^2}{\pi r^2 \sigma})} \tag{4.10}$$

where σ is the conductivity of the metal and ω_p is the plasma frequency of the medium which is given by

$$\omega_p = \sqrt{\frac{2\pi c_0^2}{a^2 \ln(a/r)}} \tag{4.11}$$

where c_0 is the speed of light.

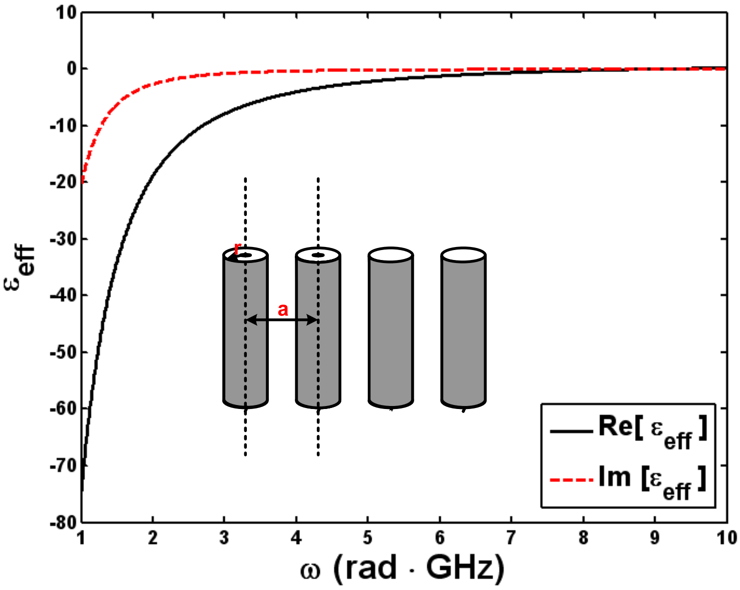

Figure 4.4: Effective dielectric constant ($\varepsilon_{eff} = \varepsilon'_{eff} - j\varepsilon''_{eff}$) of the left handed material. In subfigure, the geometry of the periodic thin wire structure is shown. The corresponding parameters are $a = 5$ mm, $r = 10^{-3}$ mm and $\sigma_{cu} = 5.8 \times 10^{7}$ S/m.

4.2.2 Split Ring Resonator

The negative permeability of the left handed material can be provided by the split ring resonator structure as shown in the subfigure in figure 4.5. After detailed calculations, the effective permeability function of this structure can be shown as [9]

$$\mu_{eff} = 1 - \frac{\frac{\pi r^2}{a^2}}{1 - \frac{2j\sigma}{\omega r \mu_0} - \frac{3dc_0^2}{\pi^2 \omega^2 r^3}} \tag{4.12}$$

4.3 Analysis of the Two Layered Medium Consisting of a Left Handed and Metallic Layers

In this section, we analyze the electrodynamics of a two-layered system consisting of a left handed material on a metal layer using both TM and TE waves like in the Chapter 3 but this time, we also consider the effect of the relative permeability of each layer to the surface plasmon dispersion relation. First, we consider a TM polarized wave propagating in x-direction and decaying in z-direction in the structure depicted in figure 4.6.

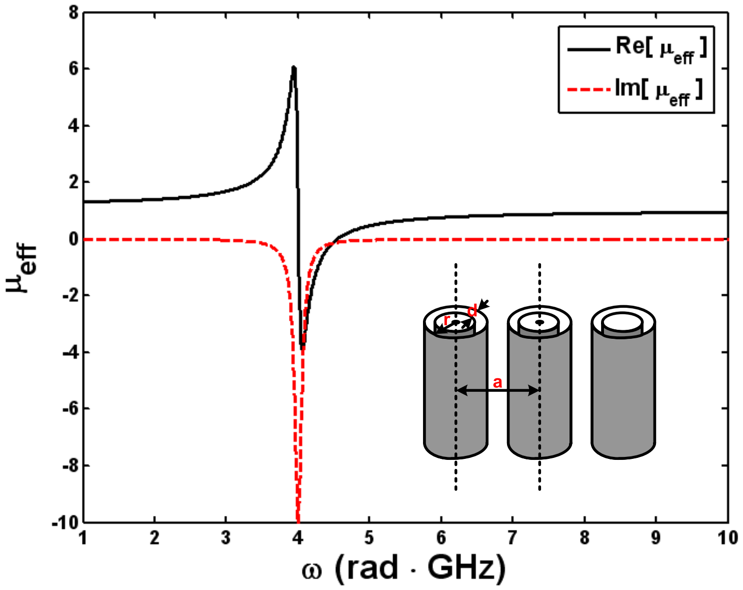

Figure 4.5: Effective permittivity ($\mu_{eff} = \mu'_{eff} - j\mu''_{eff}$) of the left handed material. In subfigure, the geometry of the split ring resonator structure is shown. The corresponding parameters are $a = 5$ mm, $r = 2$ mm, $d = 0.1$ mm and $\sigma \approx 0$.

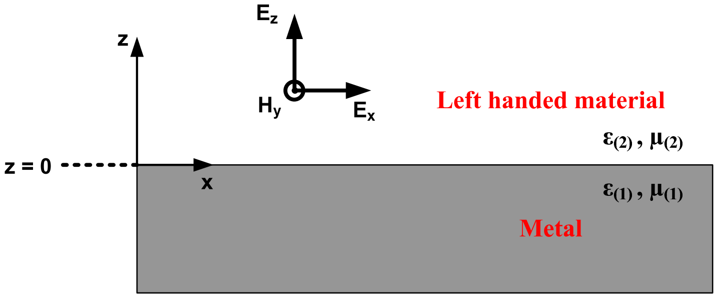

Figure 4.6: TM polarized wave in a two-layered medium.

In layer 2 ($z > 0$), the electric and magnetic fields are

$$\begin{aligned}\mathbf{H}_{(2)} &= \widehat{y}Ae^{-jk_x^{(2)}x - k_z^{(2)}z + j\omega t} \\ \mathbf{E}_{(2)} &= (\frac{A}{j\omega\varepsilon_0\varepsilon_{(2)}})(\widehat{x}k_z^{(2)} - \widehat{z}jk_x^{(2)})e^{-jk_x^{(2)}x - k_z^{(2)}z + j\omega t}\end{aligned} \tag{4.13}$$

and in layer 1 ($z < 0$)

$$\begin{aligned}\mathbf{H}_{(1)} &= \widehat{y}Be^{-jk_x^{(1)}x+k_z^{(1)}z+j\omega t} \\ \mathbf{E}_{(1)} &= (-\frac{B}{j\omega\varepsilon_0\varepsilon_{(1)}})(\widehat{x}k_z^{(1)}+\widehat{z}jk_x^{(1)})e^{-jk_x^{(1)}x+k_z^{(1)}z+j\omega t}\end{aligned} \tag{4.14}$$

where $k_z^{(2,1)}$ determines the decay in the electromagnetic fields and is calculated from the Maxwell's wave equation.

$$\begin{aligned}\nabla^2\mathbf{H}-\frac{\mu_r\varepsilon_r}{c^2}\frac{\partial^2\mathbf{H}}{\partial t^2}=0\Longrightarrow -(k_x^{(2)})^2+(k_z^{(2)})^2+(\frac{\omega}{c})^2\mu_{(2)}\varepsilon_{(2)} &= 0 \\ -(k_x^{(1)})^2+(k_z^{(1)})^2+(\frac{\omega}{c})^2\mu_{(1)}\varepsilon_{(1)} &= 0\end{aligned} \tag{4.15}$$

Assuming that there is no charge and current source ($\mathbf{J}_s = 0$ and $\rho_s = 0$) in the structure, the boundary conditions implying that the tangential components (x and y components) of the electric and magnetic fields at the interface should be continuous yields

$$A = B, \qquad A\frac{k_z^{(2)}}{\varepsilon_{(2)}} = -B\frac{k_z^{(1)}}{\varepsilon_{(1)}} \tag{4.16}$$

From equation 4.16, we get the following relationship

$$\frac{k_z^{(1)}}{k_z^{(2)}} = -\frac{\varepsilon_{(1)}}{\varepsilon_{(2)}} \tag{4.17}$$

Squaring both sides of equation 4.17 and substituting equation 4.15 into the square of equation 4.17, the surface plasmon wavevector $k_x^{(1,2)} = k_{sp}$ is found as

$$k_{sp} = \frac{\omega}{c}\sqrt{\frac{\varepsilon_{(2)}\varepsilon_{(1)}(\varepsilon_{(1)}\mu_{(2)}-\varepsilon_{(2)}\mu_{(1)})}{(\varepsilon_{(1)}^2-\varepsilon_{(2)}^2)}} \tag{4.18}$$

Second, we consider a TE polarized wave propagating in x-direction and decaying in z-direction in the structure depicted in figure 4.7.

In layer 2 ($z > 0$), the electric and magnetic fields are

$$\begin{aligned}\mathbf{E}_{(2)} &= \widehat{y}Ae^{-jk_x^{(2)}x-k_z^{(2)}z+j\omega t} \\ \mathbf{H}_{(2)} &= (-\frac{A}{j\omega\mu_0\mu_{(2)}})(\widehat{x}k_z^{(2)}-\widehat{z}jk_x^{(2)})e^{-jk_x^{(2)}x-k_z^{(2)}z+j\omega t}\end{aligned} \tag{4.19}$$

and in layer 1 ($z < 0$)

$$\begin{aligned}\mathbf{E}_{(1)} &= \widehat{y}Be^{-jk_x^{(1)}x+k_z^{(1)}z+j\omega t} \\ \mathbf{H}_{(1)} &= (-\frac{B}{j\omega\mu_0\mu_{(1)}})(\widehat{x}k_z^{(1)}-\widehat{z}jk_x^{(1)})e^{-jk_x^{(1)}x+k_z^{(1)}z+j\omega t}\end{aligned} \tag{4.20}$$

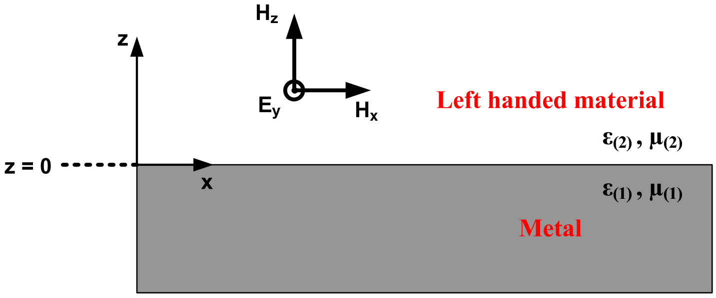

Figure 4.7: TE polarized wave in a two-layered medium.

where $k_z^{(2,1)}$ determines the decay in the electromagnetic fields and is calculated from the Maxwell's wave equation.

$$\begin{aligned}\nabla^2\mathbf{E} - \frac{\mu_r\varepsilon_r}{c^2}\frac{\partial^2\mathbf{E}}{\partial t^2} = 0 \Longrightarrow -(k_x^{(2)})^2 + (k_z^{(2)})^2 + (\frac{\omega}{c})^2\mu_{(2)}\varepsilon_{(2)} &= 0 \\ -(k_x^{(1)})^2 + (k_z^{(1)})^2 + (\frac{\omega}{c})^2\mu_{(1)}\varepsilon_{(1)} &= 0 \qquad (4.21)\end{aligned}$$

Assuming that there is no charge and current source ($\mathbf{J}_s = 0$ and $\rho_s = 0$) in the structure, the boundary conditions implying that the tangential components (x and y components) of the electric and magnetic fields at the interface should be continuous yields

$$A = B, \qquad A\frac{k_z^{(2)}}{\mu_{(2)}} = B\frac{k_z^{(1)}}{\mu_{(1)}} \qquad (4.22)$$

From equation 4.22, we get the following relationship

$$\frac{k_z^{(1)}}{k_z^{(2)}} = \frac{\mu_{(1)}}{\mu_{(2)}} \qquad (4.23)$$

Squaring both sides of equation 4.23 and substituting equation 4.21 into the square of equation 4.23, the surface plasmon wavevector $k_x^{(1,2)} = k_{sp}$ is found as

$$k_{sp} = \frac{\omega}{c}\sqrt{\frac{\mu_{(2)}\mu_{(1)}(\mu_{(1)}\varepsilon_{(2)} - \mu_{(2)}\varepsilon_{(1)})}{(\mu_{(1)}^2 - \mu_{(2)}^2)}} \qquad (4.24)$$

In figure 4.8, we compare the tangential component of the wavevector on the surface of the metal ($k_x^{(1)} = k_{(1)}\sin(\theta_t)$) with the surface plasmon wavevector. Notice that in TM case, k_x is always less than the surface plasmon wavector which means using TM polarized waves, we cannot excite the surface plasmon with the structure depicted in figure 4.6 while in TE case, after a specific incident angle, k_x is greater than the surface plasmon wavector which means using TE polarized waves, we can excite the surface plasmon with the structure depicted in figure 4.7. Thus, in this section we show that while with right handed materials, TE waves cannot be used to excite the surface plasmon as shown in Chapter 2, with the left handed materials, they can.

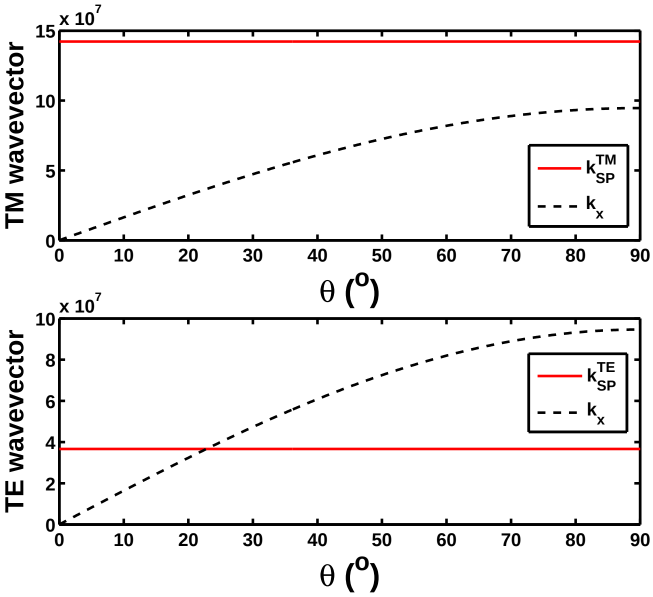

Figure 4.8: The comparison of the tangential component of the wavevector of TE and TM polarized waves with the surface plasmon wavevector. The corresponding parameters are $\varepsilon_{(2)} = -8.36$, $\mu_{(2)} = -9.77$, $\varepsilon_{(1)} = -11.6 - j1.2$, $\mu_{(1)} = 1$ and the wavelength of the incident wave is 633 nm.

4.4 Surface Plasmon Excitation with Left Handed Materials and TE Polarized Wave

We use a simple demonstration of a three-layered medium where the upper layer of dielectric is characterized by a dielectric constant $\varepsilon_{(2)}$ and permeability $\mu_{(2)}$, the middle layer of left handed material is characterized by a dielectric constant $\varepsilon_{(1)}$ and permeability $\mu_{(1)}$ and the bottom layer of metal is characterized by a dielectric constant $\varepsilon_{(0)}$ and and permeability $\mu_{(0)}$ as shown in figure 4.9. The idea is that in the upper layer, we use a TE polarized wave that propagates at an angle greater than the critical angle defined between layers 2 and 1 resulting in an evanescent field in the middle layer and this evanescent field excites the surface plasmon on the surface of the metal.[1]

---

[1] In this structure, dielectric and metal layers are infinitely thick compare to the middle layer. Hence, there is no reflection back from the top and bottom layers.

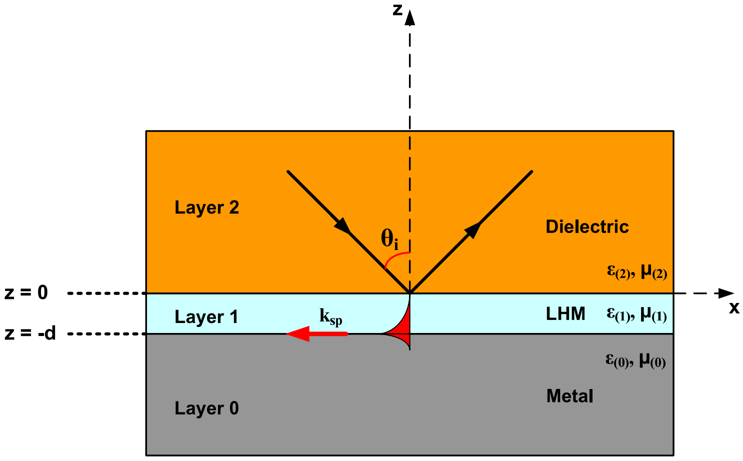

Figure 4.9: Three-layer structure used to excite the surface plasmon on the surface of the metal.

For layer 2, we can write the electric field of the TE polarized wave as below.

$$\mathbf{E}_{(2)} = \widehat{y}e^{-jk_x^{(2)}x}(A_{(2)}e^{jk_z^{(2)}z} + B_{(2)}e^{-jk_z^{(2)}z}) \tag{4.25}$$

In this equation, the unknown amplitude $B_{(2)}$ is due to the multiple reflections from the interface between layer 1 and layer 2 as depicted in figure 4.10. Thus, the generalized reflection coefficient at the interface is defined as the ratio of the sum of the reflected wave to the incident wave in layer 2, $\widetilde{R}_{2,1}^{TE} = B_{(2)}/A_{(2)}$. Using the definition of the generalized reflection coefficient, equation 4.25 becomes

$$\mathbf{E}_{(2)} = \widehat{y}A_{(2)}e^{-jk_x^{(2)}x}(e^{jk_z^{(2)}z} + \widetilde{R}_{2,1}^{TE}e^{-jk_z^{(2)}z}) \tag{4.26}$$

We can write the electric field in the middle layer as

$$\mathbf{E}_{(1)} = \widehat{y}A_{(1)}e^{-jk_x^{(1)}x}(e^{jk_z^{(1)}z} + R_{1,0}^{TE}e^{-jk_z^{(1)}(z+2d)}) \tag{4.27}$$

Assuming that $A_{(2)}$ is the user defined amplitude, we can find the amplitude $A_{(1)}$ in terms of $A_{(2)}$. Using the structure depicted in figure 4.10, we can write the expression of the amplitude transfer between layers 2 and 1 (at $z = 0$) for down-going waves.

$$A_{(1)} = A_{(2)}T_{2,1}^{TE} + A_{(1)}R_{1,0}^{TE}e^{-jk_z^{(1)}2d}R_{1,2}^{TE} \tag{4.28}$$

Thus, $A_{(1)}$ is found as

$$A_{(1)} = A_{(2)}\frac{T_{2,1}^{TE}}{1 - R_{1,0}^{TE}R_{1,2}^{TE}e^{-jk_z^{(1)}2d}} \tag{4.29}$$

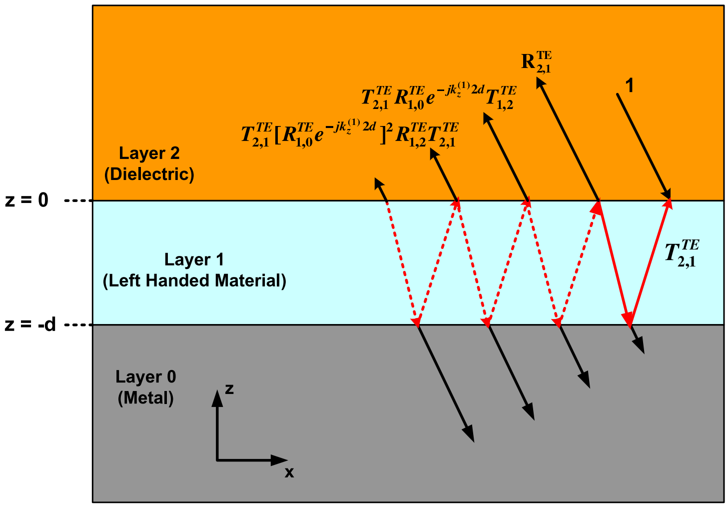

Figure 4.10: Multiple reflections in a tree-layered structure.

We write the expression of the amplitude transfer between layer 2 and layer 1 for up-going waves as

$$A_{(2)}\widetilde{R}_{2,1}^{TE} = A_{(2)}R_{2,1}^{TE} + A_{(1)}R_{1,0}^{TE}e^{-jk_z^{(1)}2d}T_{1,2}^{TE} \tag{4.30}$$

Substituting equation 4.29 into 4.30, we get the generalized reflection coefficient as

$$\widetilde{R}_{2,1}^{TE} = R_{2,1}^{TE} + \frac{T_{2,1}^{TE}T_{1,2}^{TE}R_{1,0}^{TE}e^{-jk_z^{(1)}2d}}{1 - R_{1,0}^{TE}R_{1,2}^{TE}e^{-jk_z^{(1)}2d}} \tag{4.31}$$

Due to the fact that in our analysis, the effect of the relative permeability of the layers is also counted in, the critical angle has the form shown in equation 4.32. In addition to that, in the analysis of the three-layered system where a TE polarized wave and a left handed material are used to excite the surface plasmon, the condition $\mu_2\varepsilon_2 > |\mu_1\varepsilon_1|$ is satisfied to produce an evanescent field in middle layer by using a propagating field shot from the upper layer to the middle layer with an angle greater than the critical angle defined between the upper and middle layers.

$$\sin(\theta_c) = \sqrt{\frac{\mu_1\varepsilon_1}{\mu_2\varepsilon_2}} \tag{4.32}$$

In figure 4.12, we show that our analytical calculations for the reflectivity of the three-layered system is well fitted with the result of the COMSOL Multiphysics simulation of the system shown in figure 4.11 - (a).

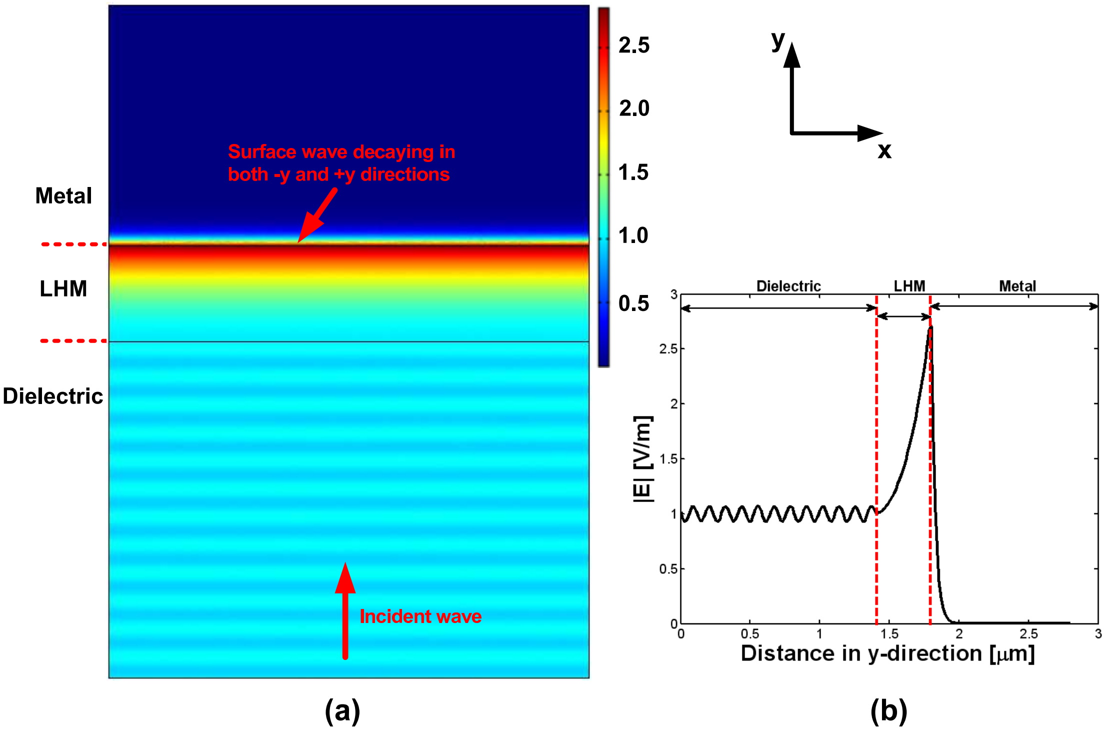

Figure 4.11: (a) COMSOL Multiphysics simulation of the three-layered system at the incident angle of 16.2^o, the angle at what the reflectivity of the system is minimum. (b) $|E|$ field distribution of the system as a function of the distance in y-direction. The corresponding parameters are $E_0 = 1$ [V/m], $\varepsilon_{(2)} = 4$, $\mu_{(2)} = 2$, $\varepsilon_{(1)} = -4.3$, $\mu_{(1)} = -0.1075$, $\varepsilon_{(0)} = -11.6 - j1.2$, $\mu_{(0)} = 1$, the wavelength of the incident wave is 633 nm and the thickness of the air gap is 400 nm.

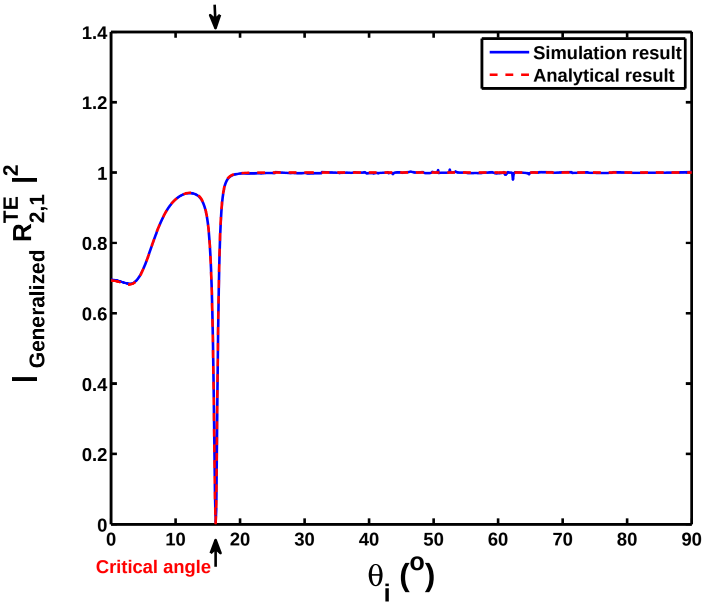

Figure 4.12: The comparison of the reflectivity graph of simulation and analytical results of the structure depicted in figure 4.9. The corresponding parameters are $\varepsilon_{(2)} = 4$, $\mu_{(2)} = 2$, $\varepsilon_{(1)} = -4.3$, $\mu_{(1)} = -0.1075$, $\varepsilon_{(0)} = -11.6 - 1.2j$, $\mu_{(0)} = 1$, the wavelength of the incident wave is 633 nm and the thickness of the air gap is 400 nm.

To understand whether the wave on the surface of the metal is a surface plasmon or not, we look at the amplitude of the electric field in each layer as in figure 4.11 - (b) using COMSOL Multiphysics. Surface waves are the waves which are evanescent in both positive and negative directions normal to the surface of the surface. Notice that the wave on the surface of the metal decays both in $+y$ and $-y$ directions which means that it is a surface wave. Thus, we can say that using our three-layered structure, we excite the surface plasmon on the surface of the metal.

In figure 4.13, the magnitude of the tangential component of the wavectors at the interface between the left handed material and the metal layer one of which in the left handed layer, $k_x^{(2)}$ and the other in the metal layer, $k_x^{(1)}$ $(= k_{sp})$ at $z = -d$ are compared. It is shown that at the incident angle where the reflectivity of the three-layered structure is minimum, $k_x^{(1)}$ starts to exceed k_{sp} as seen in figure 4.13. Hence, this result coincides with the theory saying that for the surface plasmon excitation, the tangential component of the wavevector on the surface of the metal should be greater than that of surface plasmon.

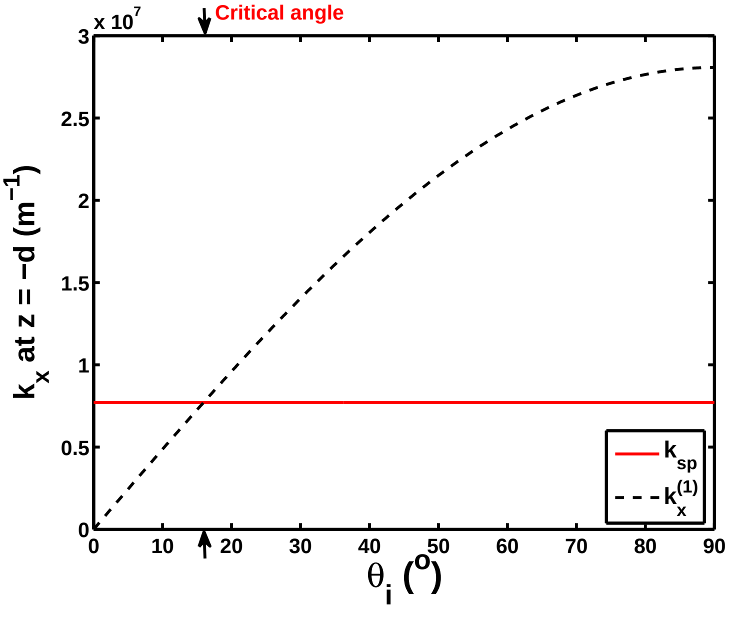

Figure 4.13: The comparison of the tangential component of the wavevector at the surface of the metal with that of the surface plasmon. The corresponding parameters are $\varepsilon_{(1)} = -4.3$, $\mu_{(1)} = -0.1075$, $\varepsilon_{(0)} = -11.6 - 1.2j$, $\mu_{(0)} = 1$ and the wavelength of the incident wave is 633 nm.

4.5 The Effect of Left Handed Materials on Surface Plasmon Propagation Length

The surface plasmon propagation length is the distance that the surface plasmon travels before its intensity diminished by e^2 and found by taking the imaginary part of the surface plasmon wavevector calculated by equation 4.24.

$$L_{sp} = \frac{1}{2Im[k_{sp}]} \tag{4.33}$$

For the two-layered configuration depicted in figure 4.7, we use a left handed material for the upper layer and a metal for the lower layer. We calculate the permittivity and permeability of the left handed material by the following formulas [10].

$$\begin{aligned} \varepsilon_{(2)} &= 1 - \frac{\omega_{pL}^2}{\omega - j\gamma} \\ \mu_{(2)} &= 1 - \frac{F\omega_0^2}{\omega^2 - \omega_0^2 - j\Gamma_L \omega} \end{aligned} \tag{4.34}$$

where ω_{pL} is the plasma frequency of the left handed material, the frequency of bulk longitudinal electron excitations, γ is the damping parameter, F is the parameter between 0 and 1, Γ_L is the scattering rate, the parameter showing the dissipation of electron motion and ω_0 is the frequency at which the effective permeability diverges. The frequency dependent dielectric function of the metal is modeled by Drude model as below.

$$\varepsilon_{(1)} = 1 - \frac{\omega_p^2}{\omega^2 - j\Gamma\omega} \tag{4.35}$$

where ω_p is the plasma frequency of the metal and Γ is the scattering rate.

Figure 4.14 shows that, when the upper layer starts to behave like a left handed material, the surface plasmon propagation length starts to increase which means, using a left handed material, we can excite a strong surface plasmon which propagates on the surface more before dissipating its energy. The reason behind this phenomenon is that the evanescent field on the upper layer is enhanced by the left handed materials. Thus, an enhanced evanescent field excites stronger surface plasmon in the lower layer.

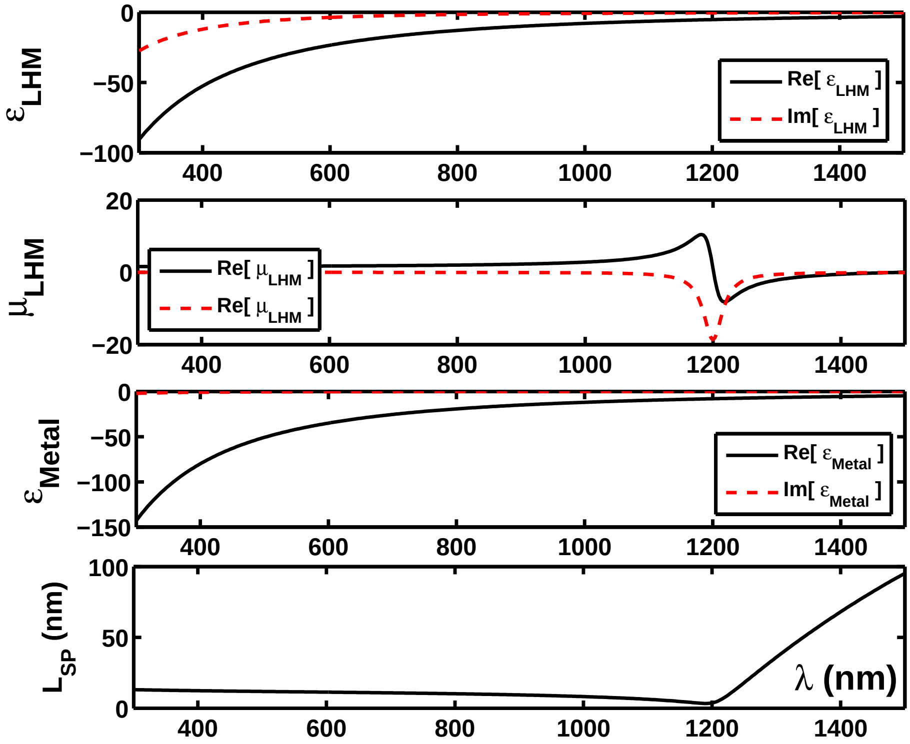

Figure 4.14: The change in the surface plasmon propagation length with respect to the change in the permittivity ($\varepsilon_{LHM} = \varepsilon'_{LHM} - j\varepsilon''_{LHM}$) and permeability ($\mu_{LHM} = \mu'_{LHM} - j\mu''_{LHM}$) of the left handed material and the permittivity ($\varepsilon_{Metal} = \varepsilon'_{Metal} - j\varepsilon''_{Metal}$) of the metal. The corresponding parameters are, for the left handed material $\omega_{pL}/2\pi = 10^{15}$ Hz (0.66 eV), $\omega_0/2\pi = 4 \times 10^{15}$ Hz (2.63 eV), $\gamma = 0.03w_{pL}$, $\Gamma_L = 0.03w_0$, $F = 0.56$ and for the metal $\omega_p/2\pi = 12 \times 10^{15}$ Hz (7.9 eV), $\Gamma = 1.45 \times 10^{13}$ Hz (0.06 eV).

Chapter 5

BLOCH'S HYDRODYNAMIC MODEL AND ITS EFFECTS ON SURFACE PLASMON THEORY

5.1 Introduction

In this chapter, the surface plasmon concept has been studied at a metal-dielectric interface using Bloch's hydrodynamic model. The dispersion relation of the surface plasmon has been reinvestigated by this model and the result has been compared with the conventional dispersion relation found by Drude model. The difference in valid frequency range between Bloch and Drude models has been shown as well.

5.2 Drude Model

Drude model models the interaction between the nucleus of the atoms and the electrons circling around the nucleus with a spring with a specific spring constant depending on the material (figure 5.1) and writes the equation of motion for this system including Newtonian, damping, restoring and electromagnetic forces. Therefore, the equation of motion for a bound charge becomes

$$(-m\omega^2 + j\omega m\Gamma + m\omega_0^2)\mathbf{r} = -e\mathbf{E} \tag{5.1}$$

where e and m are the charge and the mass of the free electrons respectively, ω_0 is the resonance frequency, Γ is the scattering rate and $\mathbf{E}$ and ω are the amplitude and the frequency of the applied electric field respectively.
Using equation 5.1, the position vector is found as

$$\mathbf{r} = -\frac{e}{m}\frac{\mathbf{E}}{\omega_0^2 - \omega^2 + j\omega\Gamma} \tag{5.2}$$

Ignoring the local field corrections and using equation 5.2, the electric susceptibility is found as below.

$$\chi = \frac{Ne^2}{\varepsilon_0 m}\frac{1}{\omega_0^2 - \omega^2 + j\omega\Gamma} \tag{5.3}$$

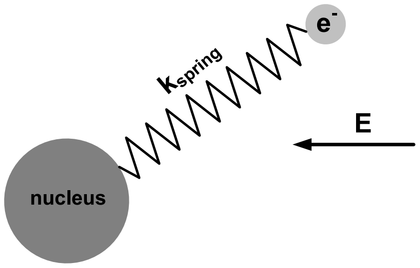

Figure 5.1: Drude oscillator model.

where N is the number of atoms. Using the definition of the plasma frequency $\omega_p = \sqrt{\frac{Ne^2}{\varepsilon_0 m}}$ and the fact that the electrons are not bounded to the atoms ($\omega_0 = 0$) in Drude model to consider only the effects of the free electrons (the equation of motion contains no restoring force), the electric susceptibility becomes

$$\chi = -\frac{\omega_p^2}{\omega^2 - j\omega\Gamma} \tag{5.4}$$

The frequency dependent dielectric function of the metal is found in equation 5.5.

$$\varepsilon_m = 1 - \frac{\omega_p^2}{\omega^2 - j\Gamma\omega} \tag{5.5}$$

The number of electrons, N has a customary relationship with the Bohr radius, a_B as shown below [18].

$$\frac{4\pi}{3}(r_s a_B)^3 = \frac{1}{N} \tag{5.6}$$

where $a_B = 0.529A^o$ and $r_s a_B$ represents the radius of the sphere which contains, on average, one electron.

In this study, we do our analysis with a noble metal, silver (Ag). For silver, the theoretical value of the dimensionless parameter is $r_s = 3.02$ then the number of electrons is calculated as $N = 5.86 \times 10^{22}\ cm^{-3}$ and $m = 0.97m_e$ where m_e is the electron mass then the plasma frequency is calculated as $w_p/2\pi = 1.39 \times 10^{16}$ Hz (9.13 eV) [26]. However, the real (experimental) value of the plasma frequency of silver is $w_p/2\pi = 5.77 \times 10^{15}$ Hz (3.8 eV) [1] so we use the real value of silver for our calculations. Using corresponding values, the dielectric constant of silver $\varepsilon_m = \varepsilon_m' - j\varepsilon_m''$ is plotted in figure 5.2.

---

[1] Datum of the plasma frequency of silver is taken from the lecture notes of Fundamentals of Optical Science Spring 2007 at the University of Central Florida.

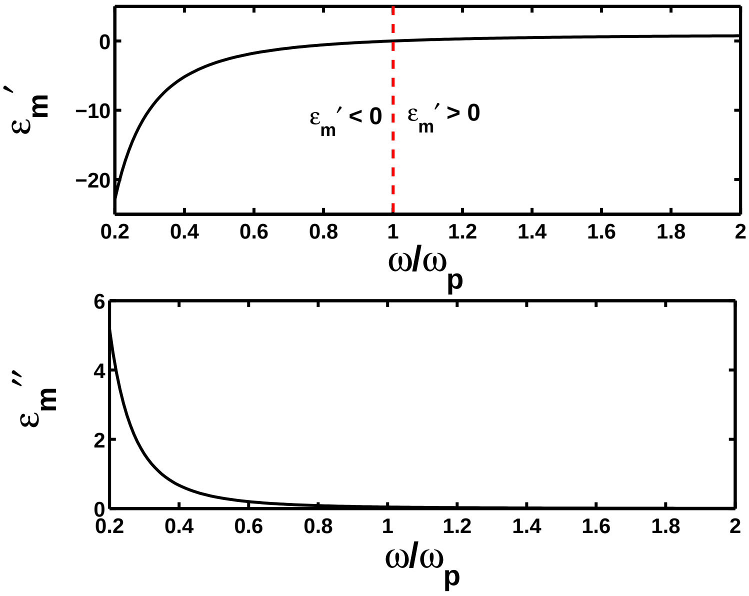

Figure 5.2: Dielectric constant of the metal modeled by Drude model ($\varepsilon_m = \varepsilon'_m - j\varepsilon''_m$). The corresponding parameters are $\omega_p/2\pi = 5.77 \times 10^{15}$ Hz (3.8 eV) and $\Gamma = 2.5 \times 10^{15}$ Hz (1.03 eV).

Because of the local interaction oriented nature, Drude model does not work efficiently around the plasma frequency. In figure 5.3, it is shown that Drude model cannot predict the behavior of the dielectric constant of silver in a wide range of frequencies, even at low frequencies.

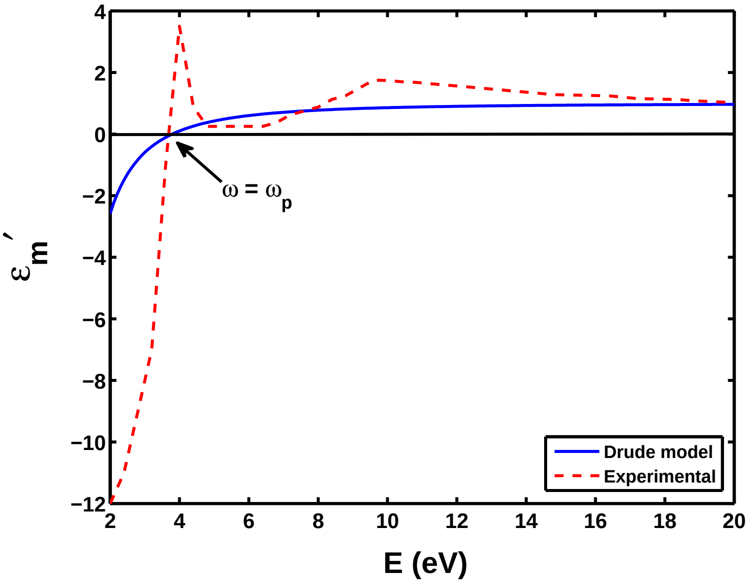

Figure 5.3: Real part of the dielectric constant of Ag calculated by experiment (dashed line) and Drude model (solid line). The corresponding parameters are $\omega_p/2\pi = 5.77 \times 10^{15}$ Hz (3.8 eV) and $\Gamma = 2.5 \times 10^{15}$ Hz (1.03 eV).

The first studies of the surface plasmon such as the studies on the dispersion relation of the surface plasmon are held in the frequency range around the plasma frequency. Actually at this range instead of Drude model, a more efficient model that treats the matter as fluid which is Bloch's hydrodynamic model should be used because at higher frequencies, the atomic level interaction cannot be negligible.

5.3 Hydrodynamic Model

The Bloch's hydrodynamic model expresses the collective motion of the oscillation in a homogenous medium without an external source as [11]

$$\begin{aligned} \frac{d}{dt}n(r,t) &= \nabla \cdot [n(r,t)\nabla\psi(r,t)] \\ \frac{d}{dt}\psi(r,t) &= \frac{1}{2}|\nabla\psi(r,t)|^2 + \frac{\partial G[n]}{\partial n} + \phi(r,t) \end{aligned} \tag{5.7}$$

where $n(r,t)$ is the electron density, $\psi(r,t)$ is the velocity potential which has a relationship with the hydrodynamic velocity $\mathbf{v}(r,t)$ that $\mathbf{v}(r,t) = -\nabla\psi(r,t)$ and $G[n]$ is the internal kinetic energy approximated by Thomas-Fermi function as $G[n] = \frac{3}{10}(3\pi^2)^{2/3}[n(r,t)]^{5/3}$. The Poisson equation is written as

$$\nabla^2\phi(r,t) = 4\pi n(r,t) \tag{5.8}$$

After linearization of the electron density and the velocity potential, we get

$$\begin{aligned} n(r,t) &= n_0(r) + n_1(r,t) + \cdots \\ \psi(r,t) &= \psi_1(r,t) + \cdots \end{aligned} \tag{5.9}$$

Hence, the linearized hydrodynamic equation becomes

$$\begin{aligned} \frac{d}{dt}n_1(r,t) &= \nabla \cdot [n_0(r)\nabla\psi_1(r,t)] \\ \frac{d}{dt}\psi_1(r,t) &= |\beta(r)|^2\frac{n_1(r,t)}{n_0(r)} + \phi_1(r,t) \\ \nabla^2\phi_1(r,t) &= 4\pi n_1(r,t) \end{aligned} \tag{5.10}$$

where $n_0(r)$ is the unperturbed electron density and $\beta(r)$ represents the speed of propagation of hydrodynamic disturbances in the system of electron.

For an electron gas in 2D, the electron density n_0 has a customary relationship with the Bohr radius, a_B as shown below [18].

$$4\pi(r_s a_B)^2 = \frac{1}{n_0} \tag{5.11}$$

where $a_B = 0.529A^o$ and $r_s a_B$ represents the radius of the disk which contains, on average, one electron. The speed of the propagation depends on the electron density as in equation 5.12 and the relation between β and the dimensionless parameter r_s [2] is shown in figure 5.4.

$$\beta = \sqrt{\frac{1}{3}}(3\pi^2 n_0)^{(\frac{1}{3})} \tag{5.12}$$

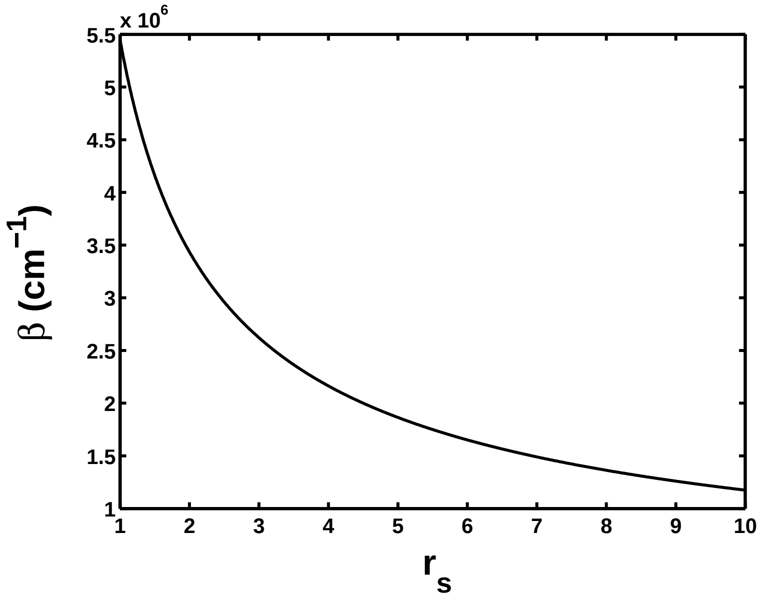

Figure 5.4: The speed of propagation of hydrodynamic disturbances, β as a function of the dimensionless parameter, r_s.

To find the dielectric constant of the metal defined by Bloch model, we model a system consisting of a semi-infinite metal and vacuum shown in figure 5.5 which has an electron density configuration depicted in equation 5.13 [11].

$$\begin{aligned} n_0(z) &= \overline{n} \quad z \leq 0 \\ &= 0 \quad z > 0 \end{aligned} \tag{5.13}$$

---

[2] Metallic densities of the conduction electrons occur mostly in the range of $2 < r_s < 6$ [18].

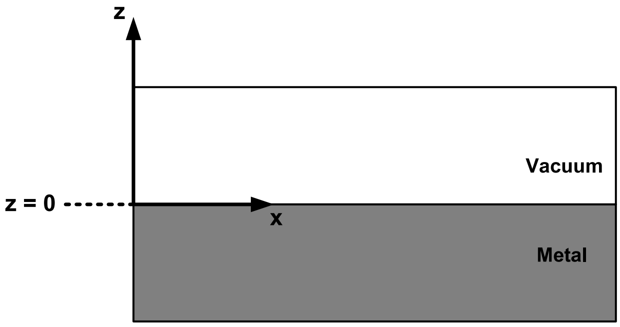

Figure 5.5: Model system consisting of a metal and vacuum which has a fast step change in the electron density distribution at $z = 0$.

Using Fourier expansion of equation 5.10, the differential equations for the plasma normal modes and the Laplace's relation are found respectively [11].

$$\begin{aligned} \nabla^2(\omega^2 - \omega_p^2 + \beta^2\nabla^2)\psi_1(r,\omega) &= 0 \quad z \leq 0 \\ \nabla^2\phi_1(r,\omega) &= 0 \quad z > 0 \end{aligned} \tag{5.14}$$

2D Fourier transform of $\psi_1(z,t)$, $\psi_1(z;q,\omega)$ satisfies the following relation.

$$(-q^2 + \frac{d^2}{dz^2})[\omega^2 - \omega_p^2 - \beta(-q^2 + \frac{d^2}{dz^2})]\psi_1(z;q,\omega) = 0 \quad z \leq 0 \tag{5.15}$$

where q is the magnitude of the 2D wavevector on the surface. Using the fact that the normal component of the hydrodynamical velocity vanishes at the interface ($z = 0$), we reach the relation between ω and q for the surface normal mode.

$$\omega^2 = \frac{1}{2}[\omega_p^2 + (\beta q)^2 + \beta q\sqrt{2\omega_p^2 + (\beta q)^2}] \tag{5.16}$$

For a system consisting of N mutually interacting electrons, the induced electron density function can be written as [12]

$$\delta n(r,\omega) = \int dr'\chi_e(r,r';\omega)\phi^{ext}(r',\omega) \tag{5.17}$$

where $\chi_e(r,r';\omega)$ is the density response function of the system of N electrons. The potential induced by an external potential $\phi^{ext}(r,\omega)$ is formulated as below.

$$\delta\phi(r,\omega) = \int dr'V(r,r')\delta n(r',\omega) \tag{5.18}$$

where $V(r,r')$ stands for the Coulomb interaction. The total potential $\phi(r,\omega)$ of a unit test charge is expressed as follows.

$$\phi(r,\omega) = \phi^{ext}(r,\omega) + \delta\phi(r,\omega) \tag{5.19}$$

Using equations 5.17 and 5.18, the total potential is found as

$$\phi(r,\omega) = \int dr'\varepsilon^{-1}(r,r';\omega)\phi^{ext}(r',\omega) \tag{5.20}$$

where the inverse longitudinal dielectric function of the system consisting of N electrons is shown as

$$\varepsilon^{-1}(r,r';\omega) = \delta(r-r') + \int dr''V(r-r'')\chi_e(r'',r';\omega) \tag{5.21}$$

The total potential $\phi(r,\omega)$ of a unit test charge at point r can be also calculated as

$$\phi(r,\omega) = \int dr'W(r,r';\omega)n^{ext}(r',\omega) \tag{5.22}$$

where $W(r,r';\omega)$ is the screened interaction which shows the collective electron oscillation and $n^{ext}(r',\omega)$ is the density of the external test charge at point r'. Assuming the translational invariance in the plane of the surface and the fact that the normal component of the hydrodynamic velocity vanishes at the interface, $W(r,r';\omega)$ is calculated from the linearized hydrodynamic equations (equation 5.10) and the electron density distribution in equation 5.13.

$$\begin{aligned}
W(z,z';\omega) &= \frac{2\pi}{q}[\varepsilon_m(z-z') + \varepsilon_m(z+z') - 2g\frac{\varepsilon_m(z)\varepsilon_m(z')}{1-\varepsilon_m^0}] && z<0, z'<0 \\
&= \frac{2\pi}{q}[2g\frac{\varepsilon_m(a)}{1-\varepsilon_m^0}e^{-qb}] && a<0, b<0 \\
&= \frac{2\pi}{q}[e^{-q|z-z'|} - ge^{q(z+z')}] && z<0, z'<0
\end{aligned} \tag{5.23}$$

where a and b are the smallest and largest values of z and z' respectively, $\varepsilon_m^0(q,\omega) = \varepsilon_m(z = 0;q,\omega)$ and

$$\begin{aligned}
\varepsilon_m(z;q,\omega) &= \frac{\Lambda\omega(\omega-j\eta)e^{-q|z|} - q\omega_p^2 e^{-\Lambda|z|}}{\Lambda[\omega(\omega-j\eta)-\omega_p^2]} \\
g(q,\omega) &= \frac{\omega_p^2}{2\beta^2\Lambda(\Lambda+q)-\omega_p^2} \\
\Lambda &= \frac{1}{\beta}\sqrt{\omega_p^2 + (\beta q)^2 - \omega(\omega-j\eta)}
\end{aligned} \tag{5.24}$$

The permittivity of the metal defined by Bloch model (equation 5.24) is shown in figure 5.6.

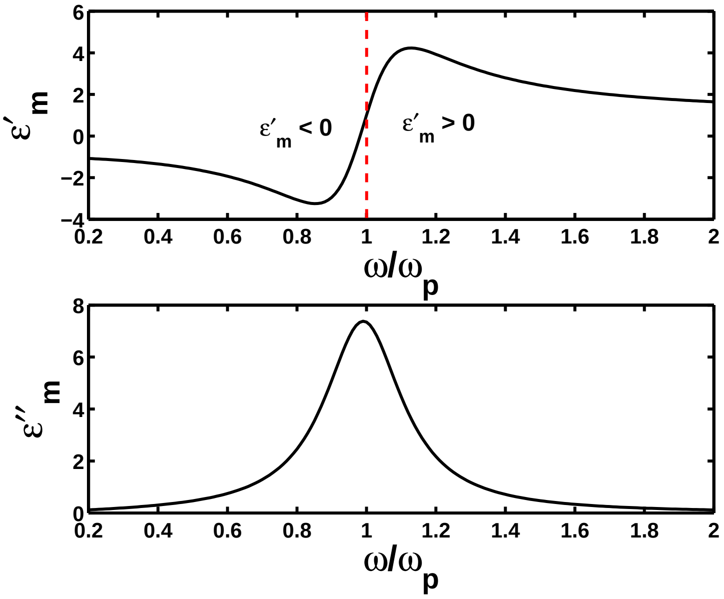

Figure 5.6: Dielectric constant of the metal modeled by Bloch model ($\varepsilon_m = \varepsilon'_m - j\varepsilon''_m$). The corresponding parameters are $\omega_p/2\pi = 5.77 \times 10^{15}$ Hz (3.8 eV) and $\eta = 2.5 \times 10^{14}$ Hz (1.03 eV).

In figure 5.7, we compare the permittivity of the metal calculated by experiment, Drude and Bloch models. Using the real value of the plasma frequency ($\omega_p = 3.8$ eV), Bloch model predicts the behavior of the dielectric constant for a wide range of frequencies (especially the peak behavior around the plasma frequency) while Drude model fails to predict it.

After analyzing the dielectric function of the metal by hydrodynamic model, we get the dispersion relation of the surface plasmon as in figure 5.8. The dramatic difference between Drude and Bloch models in the dispersion relation of the surface plasmon is that at frequency $\omega = \omega_{sp}$, there is a singularity for Drude model. The system excites the surface plasmon if and only if the dispersion curve of the surface plasmon lies below the light line. For Drude model, after frequency ω_{sp}, there is no surface plasmon excitation but for Bloch model, the surface plasmon excitation exists for all frequencies at the frequency range from 0 to ω_p. The problem in Drude model is that at the frequency range from ω_{sp} to ω_p, due to singularity, the excitation of the surface plasmon does not exist even though the matter behaves like a metal, in other words, both real and imaginary parts of the dielectric constant of the material are negative.

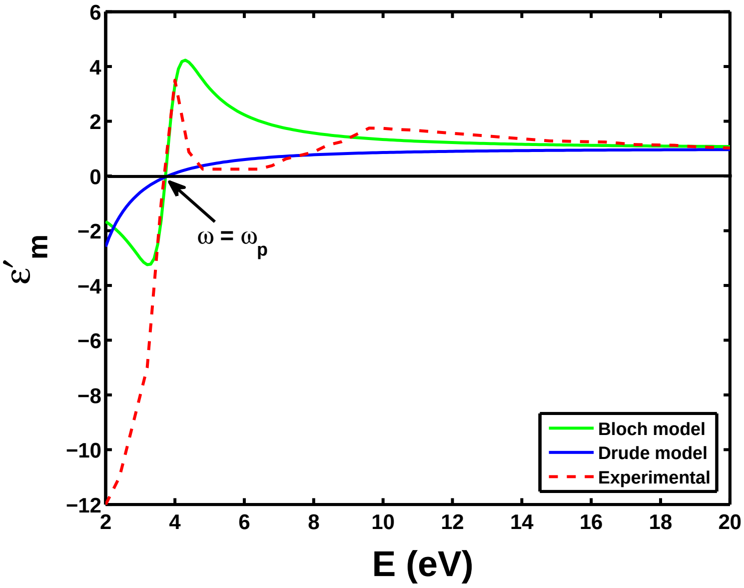

Figure 5.7: Real part of the dielectric constant of Ag determined by experiment (dashed line), Drude model (blue line) and Bloch model (green line). The corresponding parameters are $\omega_p/2\pi = 5.77 \times 10^{15}$ Hz (3.8 eV), $\Gamma = 2.5 \times 10^{14}$ Hz (1.03 eV) and $\eta = 2.5 \times 10^{14}$ Hz (1.03 eV).

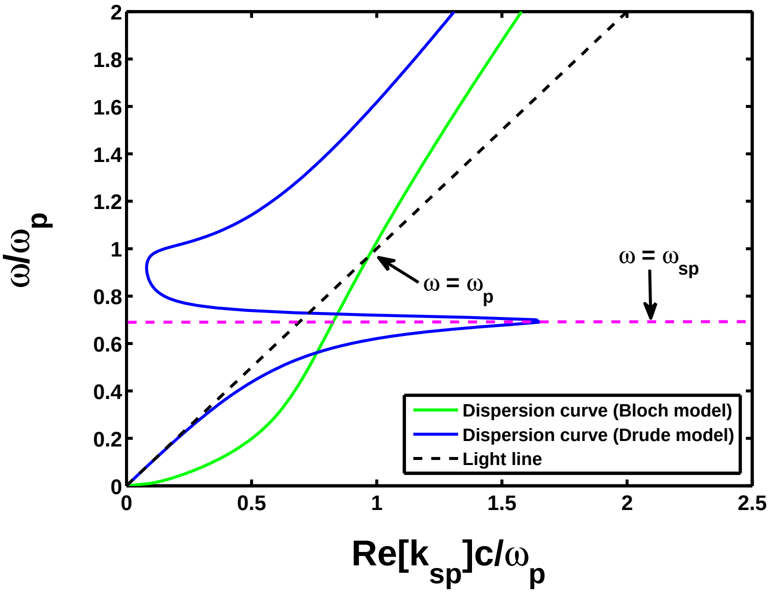

Figure 5.8: Comparison of the dispersion curves of the surface plasmon modeled by Drude (blue line) and Bloch (green line) models at an interface between a dielectric and a metal layer. The corresponding parameters are $\omega_p/2\pi = 5.77 \times 10^{16}$ Hz (3.8 eV), $\eta = 2.5 \times 10^{14}$ Hz (1.03 eV), $\Gamma = 2.5 \times 10^{14}$ Hz (1.03 eV) and $\varepsilon_d = 1$.

To see the difference between two models, we analyze a system consisting of a metal sheet which has a dielectric function calculated by both Drude and Bloch models. We then find the propagating wave with a specific wavevector on the surface of the metal using GPOF method. In the following experiment, we select a frequency ($\omega = 3$ eV $\Rightarrow \lambda = 413$ nm) in the frequency range between the surface plasmon frequency, $\omega_{sp} = 2.69$ eV and the plasma frequency, $\omega_p = 3.8$ eV to see what happens at the frequency around the singularity region for Drude model.

We analyze the metal sheet with infinite thickness at the free space wavelength of 413 nm. Using Bloch model, the dielectric constant of the metal is calculated as $\varepsilon_m = -3.0110 - j2.3019$ and from the surface plasmon dispersion relation, the surface plasmon wavevector is found as $k_{sp} = 1.6856 \times 10^7 - j1.6915 \times 10^6$ $[m^{-1}]$. Using COMSOL Multiphysics and GPOF method, we find the wavevector of the propagating field on the surface of the metal as $k_x = 1.6856 \times 10^7 - j1.5851 \times 10^5$ $[m^{-1}]$ which shows that this wave is a surface plasmon propagating on the surface of the metal. To show that this wave is a surface wave [3], we look at the amplitude of the field (figure 5.9) at the point where we select to find the wavevector of the wave and see that the field decays in both $+y$ and $-y$ directions (y is the direction normal to the surface) which means this wave is a surface wave, in other words, surface plasmon.

When we analyze the same system with Drude model, the dielectric constant of the metal is found as $\varepsilon_m = -0.5959 - j0.0875$ and the surface plasmon wavevector as $k_{sp} = 3.2786 \times 10^6 - j1.8067 \times 10^7$ $[m^{-1}]$. From COMSOL Multiphysics simulation, we get the tangential component of the wavector as $k_x = 2.7822 \times 10^5 - j1.8031 \times 10^7$ $[m^{-1}]$ which is smaller than k_{sp}, in other words this wave is not a surface plasmon. Figure 5.9 also shows that on the surface, the wave does not decay in $+y$ direction which means that the wave on the surface is not a surface wave. Thus, even though the material behaves like a metal, it does not excite surface plasmon for Drude model at the frequency range from ω_{sp} to ω_p.

---

[3] Surface waves are the waves which propagate on the surface and decay in the direction normal to the surface.

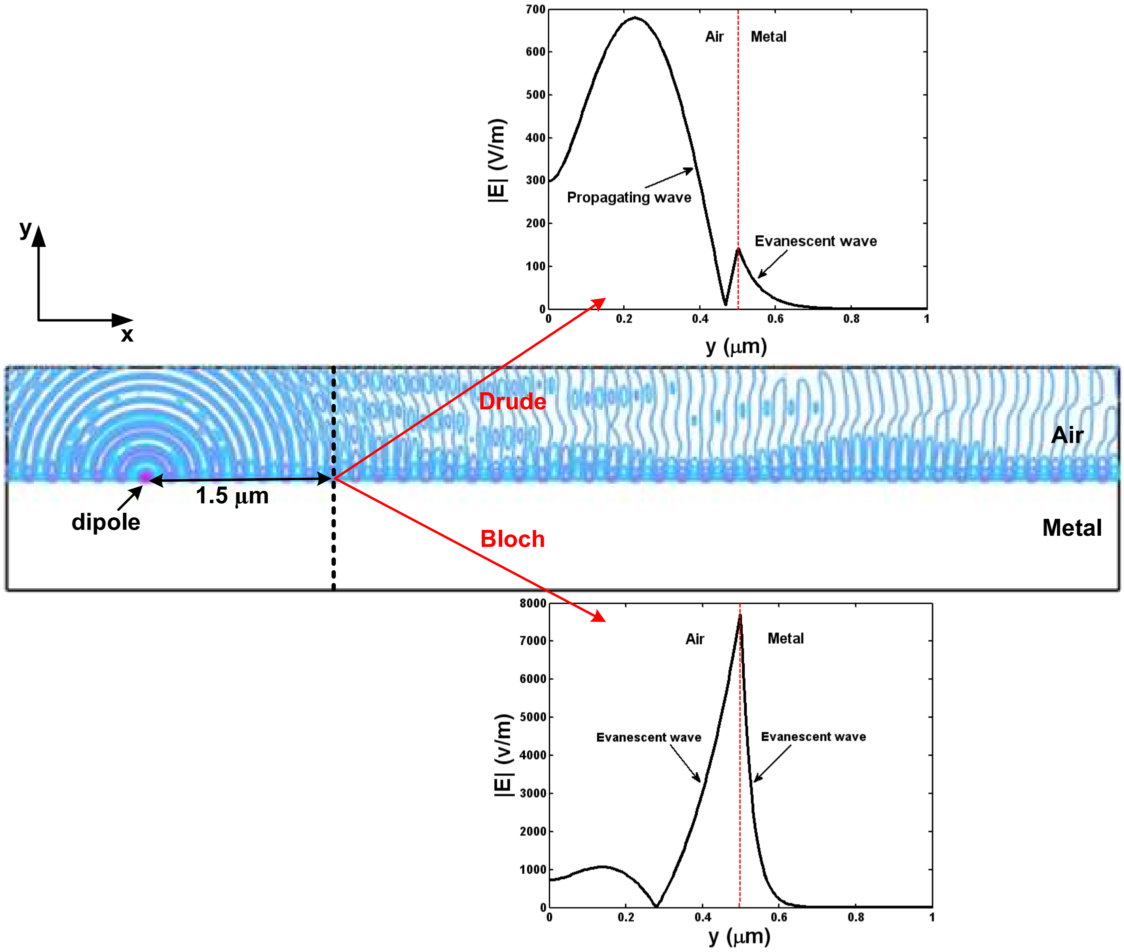

Figure 5.9: COMSOL Multiphysics simulation of the system to analyze the waves on the surface of the metal with infinite thickness. In subfigures, the amplitude of the wave at a distance 1.5 μm far away from the source is shown for both Drude and Bloch models. The corresponding parameters are $\varepsilon_{m(Drude)} = -0.5959 - j0.0875$, $\varepsilon_{m(Bloch)} = -3.0110 - j2.3019$, $\lambda = 413$ nm and $\varepsilon_d = 1$.

In this section, we show that Drude model is not a realistic method for higher frequency range and Bloch Model can be used to see the effects of fields into matter in a more accurate way. After analyzing and comparing two models, we will look at the effects of Bloch model into the surface plasmon theory through different experiments, i.e. the effective index calculation and the transmittance behavior of a slit embedded in a metal layer.

Chapter 6

ENHANCED TRANSMISSION OF LIGHT THROUGH NANO-APERTURES

6.1 Introduction

In this chapter, the effects of Bloch's hydrodynamic model on the conventional surface plasmon theory have been shown through different simulations. The effective refractive index of a slit embedded in a metal layer has been analyzed and the results have been used in the investigation of the enhanced transmission of light through the slit. The transmission behavior of light has been investigated by both Drude and Bloch models and results have been compared in the frequency range used in the conventional studies on the surface plasmon theory. A parameter defined by Bloch model depending on the electron density of the metal which has a role in controlling the effective refractive index of nano-apertures and the transmission behavior of light through nano-apertures has been introduced.

6.2 Rectangular Waveguide

Rectangular waveguides are one of the earliest types of the transmission line and has been used in many applications. The shape of the rectangular waveguide under study is shown in figure 6.1.

Guided modes in a rectangular waveguide cannot propagate below some certain frequency, the cut-off frequency. For a TM wave, $H_z = 0$ and E_z should obey the wave equation below.

$$[\frac{\partial^2}{\partial x^2} + \frac{\partial^2}{\partial y^2} + h^2]E_z(x, y) = 0 \tag{6.1}$$

Using separation of variables such that $E_z(x, y) = X(x) \cdot Y(y)$, we get

$$-\frac{1}{X(x)}\frac{\partial^2 X(x)}{\partial x^2} = \frac{1}{Y(y)}\frac{\partial^2 Y(y)}{\partial y^2} + h^2 \tag{6.2}$$

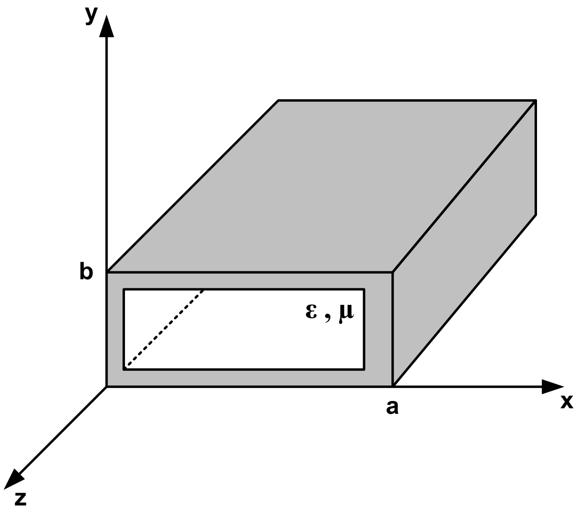

Figure 6.1: Rectangular waveguide.

Since the right side contains only x terms and the left side contains only y terms, they are both equal to a constant such that k_x^2 and k_y^2.

$$\begin{aligned} \frac{\partial^2 X(x)}{\partial x^2} + k_x^2 X(x) &= 0 \\ \frac{\partial^2 Y(y)}{\partial y^2} + k_y^2 Y(y) &= 0 \end{aligned} \tag{6.3}$$

where $k_y^2 = h^2 - k_x^2$

We then solve equation 6.3 for X and Y using corresponding boundary conditions written in equation 6.4.

$$\begin{aligned} E_z(0,y) = 0 \quad E_z(x,0) = 0 \\ E_z(a,y) = 0 \quad E_z(x,b) = 0 \end{aligned} \tag{6.4}$$

Hence, we conclude that $X(x)$ is in the form of $\sin(k_x x)$ where $k_x = m\pi/a$, $m = 1, 2, 3, ...$ and $Y(y)$ is in the form of $\sin(k_y y)$ where $k_y = n\pi/b$, $n = 1, 2, 3...$ Thus, the solution for $E_z(x,y)$ is

$$E_z(x,y) = E_0 \sin(\frac{m\pi}{a}x)\sin(\frac{n\pi}{b}y) \tag{6.5}$$

Using the fact that $h^2 = k_x^2 + k_y^2$, we have the following relation.

$$h^2 = (\frac{m\pi}{a})^2 + (\frac{n\pi}{b})^2 \tag{6.6}$$

For TM waves, we have

$$\begin{aligned}
E_x(x,y) &= -\frac{\gamma}{h^2}\frac{\partial E_z}{\partial x} &\Rightarrow\quad E_x(x,y) &= -\frac{\gamma}{h^2}(\frac{m\pi}{a}x)E_0\cos(\frac{m\pi}{a}x)\sin(\frac{n\pi}{b}y)\\
E_y(x,y) &= -\frac{\gamma}{h^2}\frac{\partial E_z}{\partial y} &\Rightarrow\quad E_y(x,y) &= -\frac{\gamma}{h^2}(\frac{n\pi}{b}x)E_0\sin(\frac{m\pi}{a}x)\cos(\frac{n\pi}{b}y)\\
H_x(x,y) &= \frac{j\omega\varepsilon}{h^2}\frac{\partial E_z}{\partial y} &\Rightarrow\quad H_x(x,y) &= \frac{j\omega\varepsilon}{h^2}(\frac{n\pi}{b}x)E_0\sin(\frac{m\pi}{a}x)\cos(\frac{n\pi}{b}y)\\
H_y(x,y) &= \frac{j\omega\varepsilon}{h^2}\frac{\partial E_z}{\partial x} &\Rightarrow\quad H_y(x,y) &= \frac{j\omega\varepsilon}{h^2}(\frac{m\pi}{a}x)E_0\cos(\frac{m\pi}{a}x)\sin(\frac{n\pi}{b}y)
\end{aligned}\tag{6.7}$$

where

$$\gamma = j\beta = j\sqrt{\omega^2\mu\varepsilon - (\frac{m\pi}{a})^2 - (\frac{n\pi}{b})^2}\tag{6.8}$$

In this representation, m and n represent the possible modes and TM_{mn} is the mode in the waveguide where m denotes the number of half cycle variations of the fields in the x-direction and n denotes the number of half cycle variations of the fields in the y-direction. For TM modes in the rectangular waveguide, neither m nor n can be zero because the field expressions are zero if either m or n is zero. Thus, the lowest mode for the rectangular waveguide of TM mode is TM_{11}.

The cut-off wave number is

$$k_c = \sqrt{(\frac{m\pi}{a})^2 + (\frac{n\pi}{b})^2}\tag{6.9}$$

and

$$\beta = \sqrt{k^2 - k_c^2}\tag{6.10}$$

and the cut-off frequency is

$$f_c = \frac{1}{2\sqrt{\varepsilon\mu}}\sqrt{(\frac{m}{a})^2 + (\frac{n}{b})^2}\tag{6.11}$$

and the cut-off wavelength is

$$\lambda_c = \frac{2}{\sqrt{(\frac{m}{a})^2 + (\frac{n}{b})^2}}\tag{6.12}$$

While modes with a frequency greater than f_c propagate, the modes with $f < f_c$ lead to an imaginary b, decay exponentially and do not propagate (cut-off or evanescent modes).

The mode with the lowest cut-off frequency is called the dominant mode. Since TM modes for the rectangular waveguides start from TM_{11} mode, the dominant frequency is

$$(f_c)_{11} = \frac{1}{2\sqrt{\varepsilon\mu}}\sqrt{(\frac{1}{a})^2 + (\frac{1}{b})^2}\tag{6.13}$$

For rectangular waveguide, the wave impedance is defined as the ratio of the transverse electric field E_x and the magnetic field H_y.

$$Z_{TM} = \frac{E_x}{H_y} = \frac{\gamma}{j\omega\varepsilon} = \frac{j\beta}{j\omega\varepsilon} \Rightarrow Z_{TM} = \frac{\beta\eta}{k} \tag{6.14}$$

6.3 Slit on a Thin Metal Film

The surface plasmon formed on the surface of the metal influences the refractive index of the slit embedded in a thin metal film. To understand the refractive index phenomenon, we model the slit as a rectangular waveguide [14]. Due to coupling of the incident wave to the surface plasmon, the cut-off wavelength increases, in comparison with a perfect conducting waveguide, as the slit width is reduced. Two contributions that cause the extension of the cut-off wavelength are first, the penetration of the field into the metal along the x-direction and second, the coupling between the surface plasmon modes along the z-direction for the configuration in figure 6.2.

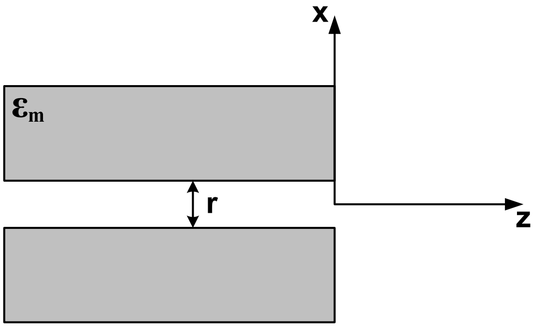

Figure 6.2: Geometry of the problem under consideration.

In figure 6.3, the system, a subwavelength slit embedded in a metal layer characterized by a frequency dependent negative relative permittivity is shown. The TM problem is solved within the subwavelength regime where only one mode is assumed to exist within the slit. The cut-off condition of the rectangular waveguide is found by considering the surface plasmon coupled on the surface of the metal. Considering the case of two parallel plates, we can formulate the TM mode of this configuration as the sum of the surface plasmon modes on the top and the bottom plates. In the region between the plates, the field has

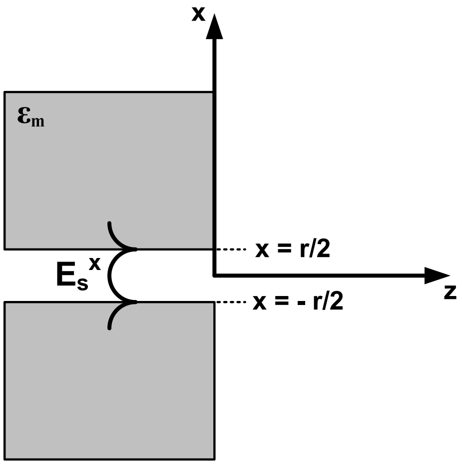

Figure 6.3: Schematic representation of the slit embedded in a metal layer with relative permittivity ε_m. The magnitude of the x-component of the electric field of the lowest-order mode inside the slit, $|E_x^s|$ is shown. The slit width is represented as r and the boundary to free space is at $z = 0$.

a hyperbolic cosine dependence obtained from the sum of two exponentials of the surface plasmon modes decaying on the top and bottom plates [15].

$$\begin{aligned} E_x^s(x,s) &= \cosh(\sqrt{k_0^2 - k_z^2}x)e^{-jk_z z} && |x| \leq r/2 \\ &= \frac{1}{\varepsilon_m}\cosh(\sqrt{k_0^2 - k_z^2}r/2)e^{[-\sqrt{k_z^2 - \varepsilon_m k_0^2}(|x| - r/2)]}e^{-jk_z z} && |x| > r/2 \end{aligned} \tag{6.15}$$

where k_0 is the free-space wave vector, k_z is the propagation constant in the z-direction, ε_m is the relative permittivity of the metal and r is the width of the slit, which is centered at $x = 0$. From the Maxwell-Faraday equation, the corresponding y-component of the magnetic field can be found. Using the corresponding boundary conditions, the equation of the propagation constant of this mode is found.

$$\tanh(\sqrt{k_z^2 - k_0^2}r/2) = \frac{-\sqrt{k_z^2 - \varepsilon_m k_0^2}}{\varepsilon_m\sqrt{k_z^2 - k_0^2}} \tag{6.16}$$

In the case of a metal slit with slit width r, propagation of a plasmon wave along the slit is governed by the following dispersion relation formed by rearranging the terms in equation 6.16 [16].

$$\frac{\gamma_m}{\varepsilon_m} + \frac{\gamma_d}{\varepsilon_d}\frac{1 - e^{-\gamma_d r}}{1 + e^{-\gamma_d r}} = 0 \tag{6.17}$$

where the decay constant of the surface plasmon fields inside the slit region is

$$\gamma_d = (k_{eff}^2 - \varepsilon_d k_0^2)^{1/2} = k_0(n_{eff}^2 - \varepsilon_d)^{1/2} \tag{6.18}$$

and the decay constant in the metal region is

$$\gamma_m = (k_{eff}^2 - \varepsilon_m k_0^2)^{1/2} = k_0(n_{eff}^2 - \varepsilon_m)^{1/2} \tag{6.19}$$

Using equations 6.17, 6.18 and 6.19, we calculate the effective refractive index, n_{eff} which relates the wave vector k_z propagating in the slit region to the wave vector in the air region, $k_z = n_{eff}k_0$. In a PEC, due to the fact that $n_{eff} = n_0 = 1$, the propagation constant of the mode within the slit is the same as free space. Figures 6.4 and 6.5 show that the real part of the propagation constant is much larger than the imaginary part (because $|n'_{eff}| > |n''_{eff}|$) which means that the wave in the slit region sees less attenuation. Figure 6.4 shows that as the magnitude of the real part of the dielectric constant of the metal increases, both real and imaginary parts of the effective refractive index decrease and figure 6.5 shows that as the magnitude of the imaginary part of the dielectric constant of the metal increases, the real part of the effective refractive index decreases whereas the imaginary part of the effective refractive index increases.

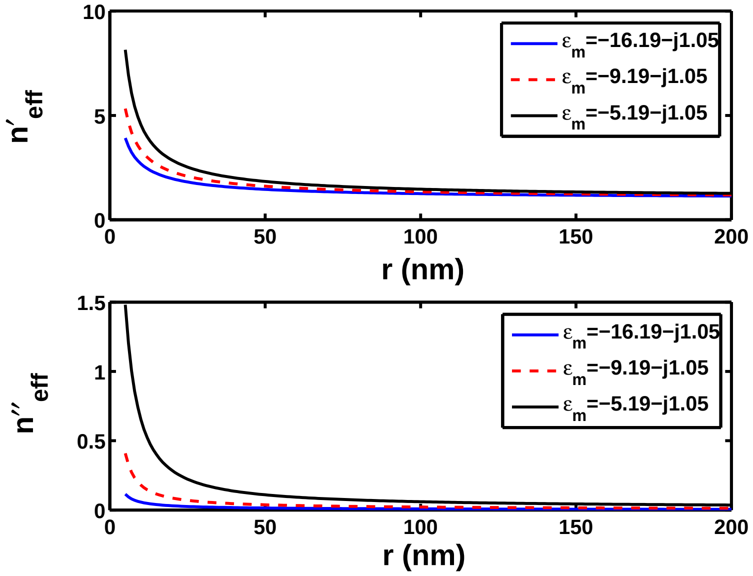

Figure 6.4: Real and imaginary parts of the effective refractive index ($n_{eff} = n'_{eff} - jn''_{eff}$) of the slit for different permittivity values as a function of slit width. (Real part of the dielectric constant is changed.) The corresponding parameters are $\lambda = 650$ nm and $\varepsilon_d = 1$.

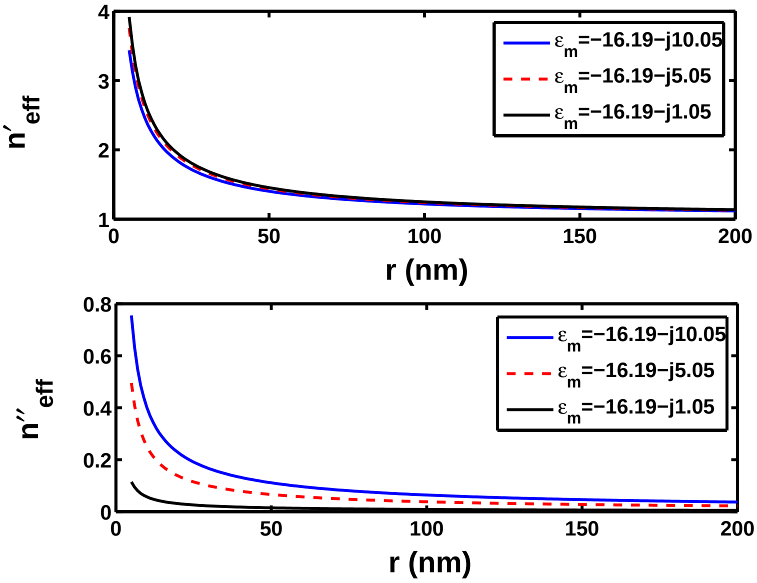

Figure 6.5: Real and imaginary parts of the effective refractive index ($n_{eff} = n'_{eff} - jn''_{eff}$) of the slit for different permittivity values as a function of slit width. (Imaginary part of the dielectric constant is changed.) The corresponding parameters are $\lambda = 650$ nm and $\varepsilon_d = 1$.

It can be inferred that the propagation constant increases as the slit width is made narrower and the relative permittivity of the metal is reduced in magnitude. These two cases both correspond to an increased penetration of the electric field into the metal. If we look at the permittivity formula (equation 6.20), we see that as the effective conductivity increases, system behaves like PEC and n_{eff} becomes close to the refractive index of the material filling the slit region (In our case it is air with $\varepsilon_d = 1 \Rightarrow n_d = 1$). It is seen from figures 6.4 and 6.5 that as the width of the slit is increased to a value comparable to the wavelength of the free space, n_{eff} converges to the free space refractive index which is $n_0 = 1$.

$$\varepsilon = \varepsilon' - j\varepsilon'' - \frac{\sigma}{\omega} = \varepsilon'(1 - \frac{\sigma_{eff}}{\omega\varepsilon'}) \tag{6.20}$$

Figure 6.6 and 6.7 show the variation in the real and imaginary parts of the effective refractive index of the slit as a function of wavelength where the permittivity of the metal is determined by Drude and Bloch models. For the two models, the material behaves like a metal[1] for the frequency range smaller than the plasma frequency. Also to define an

---

[1] The dispersion relation depicted in equation 6.17 gives the solution of n_{eff} for only the frequency range which makes sure that the material has the properties of a metal (Both real and imaginary parts of the permittivity are negative).

effective refractive index, there should be an excitation of surface plasmon because effective refractive index is the refractive index that relates the surface plasmon wavevector to the free space wavevector. Thus, for our system where a TM polarized wave is used to excite the surface plasmon, we select the frequency values smaller than ω_p.

For Drude model, both real and imaginary parts of the effective refractive index decrease with wavelength. For the frequency range greater than the surface plasmon frequency ω_{sp}, due to the singularity in the dispersion relation at ω_{sp}, the effective index cannot be defined because the surface plasmon is excited only for frequencies smaller than the surface plasmon frequency. When it comes to the effective refractive index modeled by Bloch's hydrodynamic model, both real and imaginary parts of the effective refractive index increase with wavelength. Another difference between two models in the refractive index phenomenon is that for the frequency range between ω_{sp} and ω_p, Drude model cannot define an effective refractive index while Bloch model can.

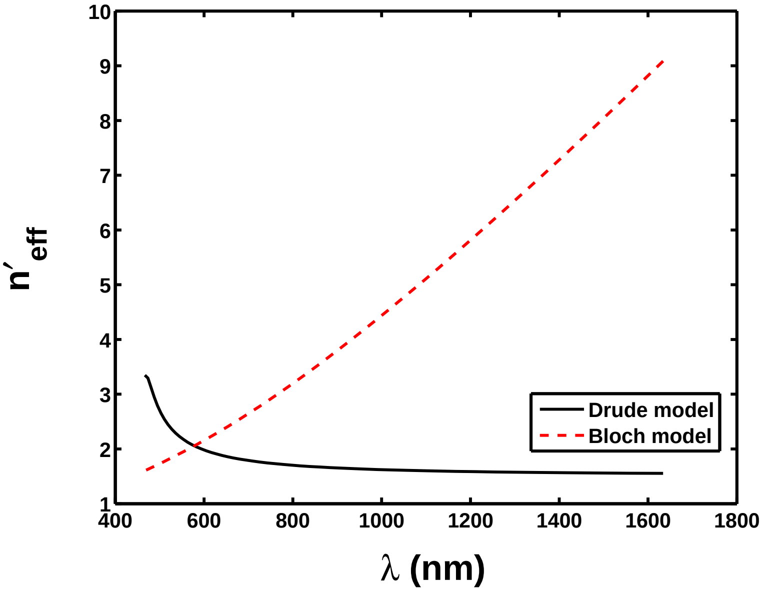

Figure 6.6: Real part of the effective refractive index ($n_{eff} = n'_{eff} - jn''_{eff}$) of the slit as a function of wavelength. The corresponding parameters are $\omega_p/2\pi = 5.77 \times 10^{15}$ Hz (3.8 eV), $\lambda_p = 327$ nm, $\omega_{sp}/2\pi = 4.08 \times 10^{15}$ Hz (2.69 eV), $\lambda_{sp} = 462$ nm, $\eta = 2.5 \times 10^{14}$ Hz (1.03 eV), $\Gamma = 2.5 \times 10^{14}$ Hz (1.03 eV), $r = 80$ nm and $\varepsilon_d = 1$.

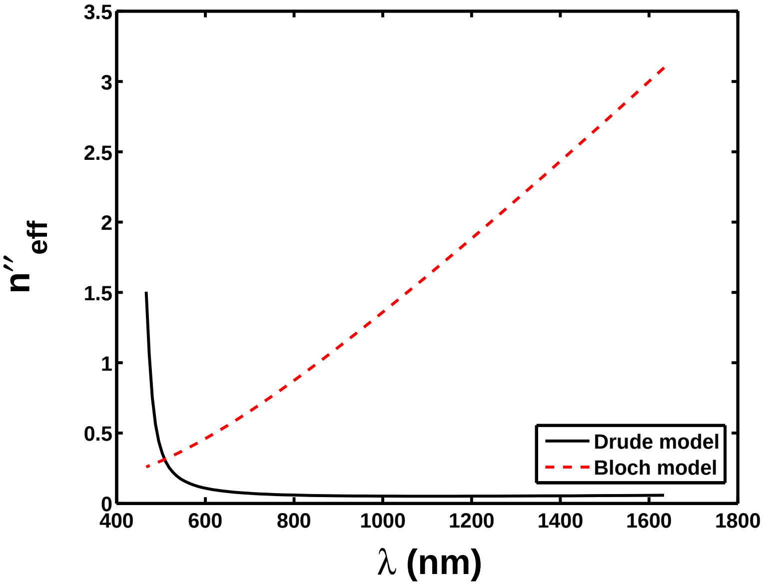

Figure 6.7: Imaginary part of the effective refractive index ($n_{eff} = n'_{eff} - jn''_{eff}$) of the slit as a function of wavelength. The corresponding parameters are $\omega_p/2\pi = 5.77 \times 10^{15}$ Hz (3.8 eV), $\lambda_p = 327$ nm, $\omega_{sp}/2\pi = 4.08 \times 10^{15}$ Hz (2.69 eV), $\lambda_{sp} = 462$ nm, $\eta = 2.5 \times 10^{14}$ Hz (1.03 eV), $\Gamma = 2.5 \times 10^{14}$ Hz (1.03 eV), $r = 80$ nm and $\varepsilon_d = 1$.

6.4 Enhanced Transmission of a Slit

Figure 6.8 shows the optical transmission of a wave through a single slit formed in a metal layer. The incident wave excites the surface plasmon at the slit entrance which propagates along the slit region with a complex propagation constant and decouples into radiation modes at the slit exit and diffracts into all radial directions with a uniform power distribution.

To show that nano-slits are one of the sources of the surface plasmon, we set up a system with COMSOL Multiphysics as shown in figure 6.9. In the system, a magnetic dipole which excites TM polarized waves in all kinds, i.e. planar and evanescent waves is located at the far field. The dipole is located at the far field to prevent decaying fields from reaching the surface of the metal so only propagating planar-like waves hit the surface. Hence, we avoid the surface plasmon excitation by the evanescent wave formed by the magnetic dipole.

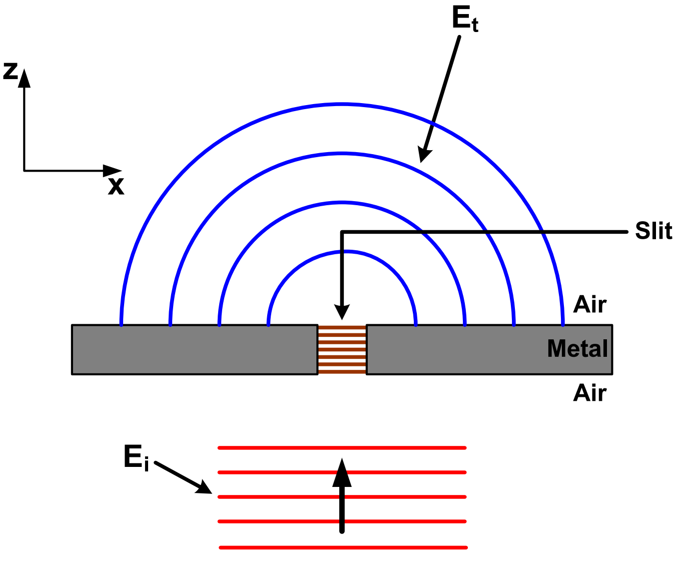

Figure 6.8: Optical transmission through a single slit formed in a metal layer. A TM-polarized plane wave is incident on the slit from the bottom side of the metal film. In the system, E_i and E_t are the incident and transmitted waves respectively.

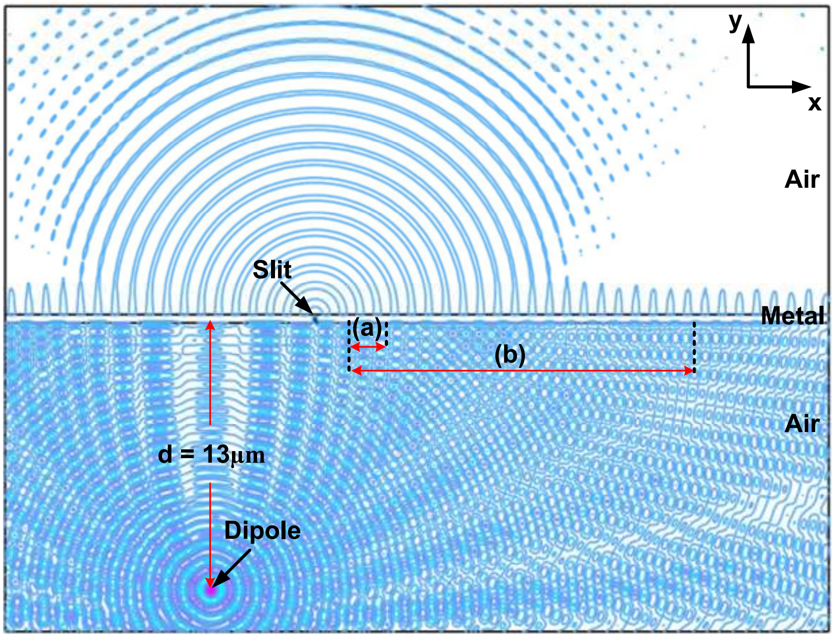

Figure 6.9: COMSOL Multiphysics simulation of the optical transmission through a single nano-slit embedded in a metal layer. TM-polarized wave with a wavelength of 852 nm is shot to the bottom side of the metal film with thickness of 400 nm and slit width of 100 nm. $\varepsilon_m = -33.22 - j1.7$ and $\varepsilon_d = 1$. The surface plasmon wavevector is calculated as $k_{sp} = 7.4881 \times 10^6 - j4.0874 \times 10^3\ [m^{-1}]$.

To show how nano-slits have a role in the excitation of the surface plasmon, we design two systems, one of which is a system that includes a metal layer and the second one, a system which includes a metal layer with a nano-slit embedded on it. We then subtract the field data obtained from the first system from the field data obtained from the second system. Then the remaining data are the data of the fields generated only by slit. We fit this data into five exponentials with GPOF method and determine which exponential corresponds to a propagating wave, a surface plasmon or just a noise (the term with very small amplitude). In the following two results, we show the exponentially fitted field data for a region, horizontally 1 μm far away from the slit (region-a) and a region, 20 μm far away from the slit (region-b). The field data show that the slit produces the surface plasmon itself.

In region-a, the fields are found as

$$\mathbf{H}_1 = \widehat{z}(0.0709) \times e^{-j(297.81-j9.20)10^6 x} \ [A/m] \quad \Rightarrow \text{Noise}$$
$$\mathbf{H}_2 = \widehat{z}(0.1168) \times e^{-j(203.23-j120.34)10^6 x} \ [A/m] \quad \Rightarrow \text{Noise}$$
$$\mathbf{H}_3 = \widehat{z}(55.0367) \times e^{-j(7.57-j0.02)10^6 x} \ [A/m] \quad \Rightarrow \text{SPP}$$
$$\mathbf{H}_4 = \widehat{z}(0.0201) \times e^{-j(3.76-j0.36)10^6 x} \ [A/m] \quad \Rightarrow \text{Noise}$$
$$\mathbf{H}_5 = \widehat{z}(0.0100) \times e^{-j(6.95-j0.49)10^6 x} \ [A/m] \quad \Rightarrow \text{Noise}$$

and for region-b

$$\mathbf{H}_1 = \widehat{z}(0.0007) \times e^{-j(242.22-5.70j)10^6 x} \ [A/m] \quad \Rightarrow \text{Noise}$$
$$\mathbf{H}_2 = \widehat{z}(0.0041) \times e^{-j(282.52-24.33)10^6 x} \ [A/m] \quad \Rightarrow \text{Noise}$$
$$\mathbf{H}_3 = \widehat{z}(0.01679) \times e^{-j(7.64-j0.13)10^6 x} \ [A/m] \quad \Rightarrow \text{Noise}$$
$$\mathbf{H}_4 = \widehat{z}(4.6443) \times e^{-j(7.48-j1.09)10^6 x} \ [A/m] \quad \Rightarrow \text{SPP}$$
$$\mathbf{H}_5 = \widehat{z}(0.2782) \times e^{-j(7.41-j0.27)10^6 x} \ [A/m] \quad \Rightarrow \text{Noise}$$

The transmission of light through a single slit is expressed in terms of its magnitude and phase as $T = Ae^{-j\phi}$ [13].

$$\begin{aligned} A &= \frac{\tau_{01}\tau_{12}e^{-jkh}}{1+\rho_{01}\rho_{12}e^{-j2kh}} \\ \phi &= \phi_{01}+\phi_{12}+n_{eff}k_0 h-\theta \end{aligned} \qquad (6.21)$$

where $k = n_{eff}k_0$, h is the slit depth, 0, 1 and 2 denote the media before, inside, and after the nano-slit array respectively, and $\rho_{01} = (n_0 - n_{eff})/(n_0 + n_{eff})$, $\rho_{12} = (n_{eff} - n_2)/(n_{eff} + n_2)$, $\phi_{01} = arg[\rho_{01}]$, $\phi_{12} = arg[\rho_{12}]$, $\tau_{01} = 1 - \rho_{01}$, $\tau_{12} = 1 - \rho_{12}$, $\theta = arg[1 + \phi_{01}\phi_{12}e^{-j2kh}]$ where n_0 and n_2 are the refractive indices of the media outside the slit. For a specific wavelength, variation in the amplitude and phase of the transmittance of a slit with respect to the slit depth is shown in figure 6.10.

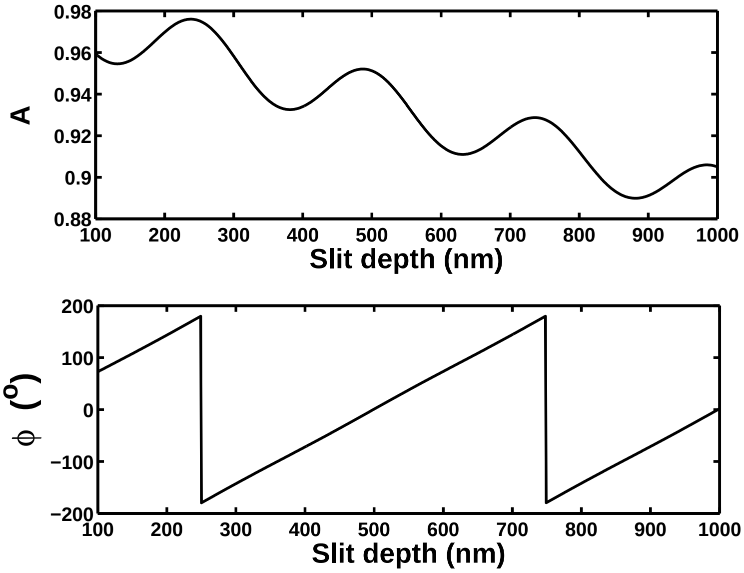

Figure 6.10: Amplitude (A) and phase (ϕ) of the transmittance of a single slit embedded in a thin metal layer as a function of slit depth. The corresponding parameters are $\varepsilon_m = -16.19 - j1.05$, $r = 80$ nm, $\varepsilon_d = 1$ and $\lambda = 650$ nm.

For the one-slit case as depicted in figure 6.8, we increase the thickness of the metal layer in 20-nm steps and plot the magnitude of the transmitted wave at the center of the slit exit where the $|H_z|$ distribution of the field is maximum on the surface of the metal. Figure 6.11 shows one of the COMSOL Multiphysics simulations when the thickness of the metal layer is 200 nm.

Figure 6.12 shows that the transmittance behavior of the system shows Bessel function characteristics and the periodicity of the function is $\lambda_{eff}/2$ where λ_{eff} is the effective wavelength in the slit region. Using the slit width dependent effective refractive index formula (equation 6.17), we find the effective refractive index of the slit for our case where we shot a TM polarized planar wave with a wavelength of 650 nm to the bottom side of the

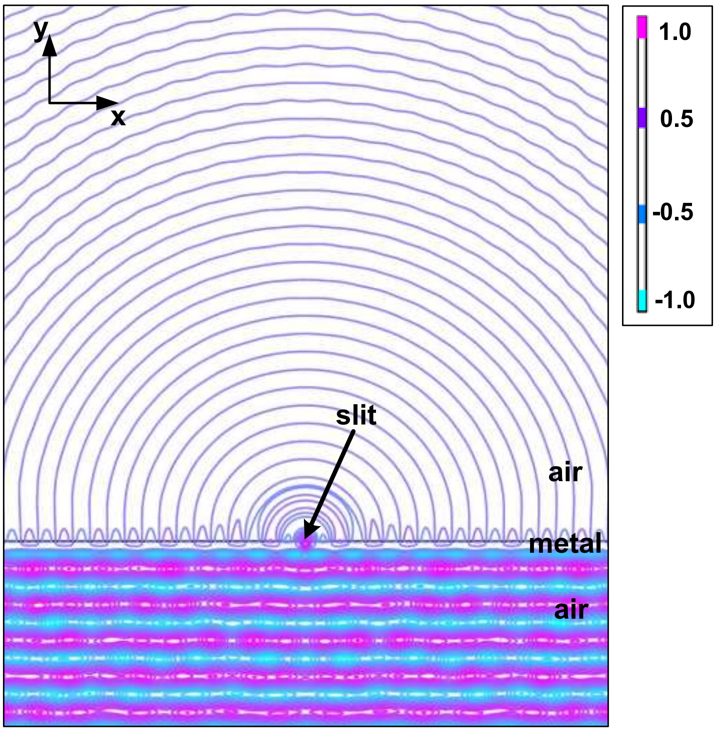

Figure 6.11: COMSOL Multiphysics simulation of the system consisting of a single slit formed in a metal layer ($\varepsilon_m = -16.19 - j1.05$, $\varepsilon_d = 1$). A TM-polarized plane wave with 650 nm wavelength is shot to the bottom side of the metal layer with thickness of 200 nm where a 80 nm wide slit is embedded in.

metal layer where a 80 nm wide slit is embedded in.

$$n_{eff} \approx 1.3023 - j0.01 \Rightarrow \lambda_{eff} = \frac{\lambda_0}{n_{eff}} \approx 500 \ \ nm \Rightarrow \frac{\lambda_{eff}}{2} \approx 250 \ \ nm \tag{6.22}$$

This fact shows that the effective refractive index dependent on the width of the slit on the metal film effects the transmittance behavior of the the slit.

6.5 Enhanced Transmission Analyzed using Bloch Model

After analyzing the enhanced transmission theory, we show how Bloch model modifies the conventional transmission theory with a transmission experiment. In this study, we first find the dielectric constant of a material with both Drude and Bloch models and using this dielectric constant values, we find the effective refractive indices for a slit formed on this material to calculate the transmittance of this slit.

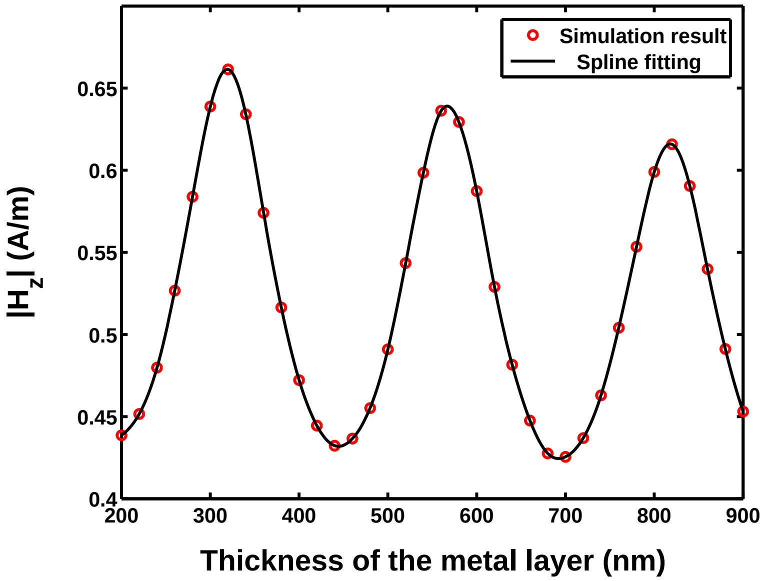

Figure 6.12: Maximum amplitude of the transmitted field from the slit as a function of the slit thickness for the single-slit case. The corresponding parameters are $r = 80$ nm, $\lambda = 650$ nm, $\varepsilon_m = -16.19 - j1.05$ and $\varepsilon_d = 1$.

Figures 6.13 and 6.14 show the amplitude and phase of the transmittance of light through the slit respectively as a function of wavelength for Drude and Bloch models.

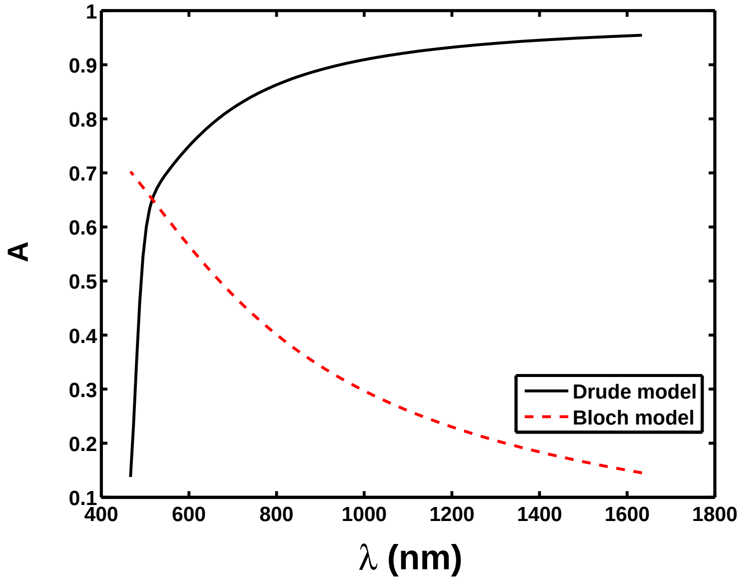

Figure 6.13: Amplitude of the transmittance of light through a single slit embedded in a thin metal layer as a function of wavelength. The corresponding parameters are $\omega_p/2\pi = 5.77 \times 10^{15}$ Hz (3.8 eV), $\lambda_p = 327$ nm, $\omega_{sp}/2\pi = 4.08 \times 10^{15}$ Hz (2.69 eV), $\lambda_{sp} = 462$ nm, $\eta = 2.5 \times 10^{14}$ Hz (1.03 eV), $\Gamma = 2.5 \times 10^{14}$ Hz (1.03 eV), $r = 80$ nm and $\varepsilon_d = 1$.

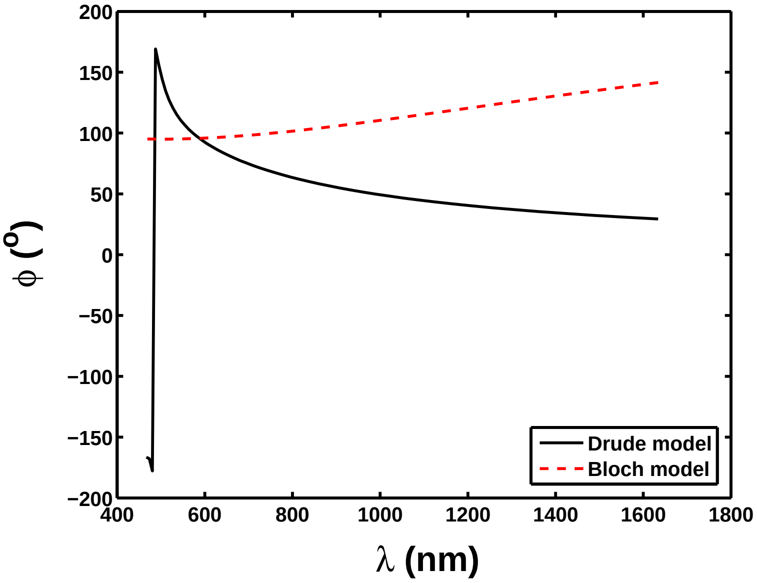

Figure 6.14: Phase of the transmittance of light through a single slit embedded in a thin metal layer as a function of wavelength. The corresponding parameters are $\omega_p/2\pi = 5.77 \times 10^{15}$ Hz (3.8 eV), $\lambda_p = 327$ nm, $\omega_{sp}/2\pi = 4.08 \times 10^{15}$ Hz (2.69 eV), $\lambda_{sp} = 462$ nm, $\eta = 2.5 \times 10^{14}$ Hz (1.03 eV), $\Gamma = 2.5 \times 10^{14}$ Hz (1.03 eV), $r = 80$ nm and $\varepsilon_d = 1$.

At higher frequencies (smaller wavelength), the phase and amplitude of the transmittance calculated by Drude and Bloch models show radical differences. The focus of our study is smaller wavelengths and the previous studies ([1], [2], [3], [4], [5], [11], [13], [16], [19], [20], [21], [22]) on the surface plasmon theory, i.e. plasmon coupling or enhanced transmission are generally done in the wavelength range from 400 nm to 1600 nm (187.5 THz to 750 THz), which is the wavelength range where the difference between two transmission behaviors of light calculated by Drude and Bloch models cannot be negligible. Around the higher operational frequencies (low wavelength), Drude model becomes inefficient to predict the transmission behavior of light through nano-apertures due to the fact that as the wavelength of the fields is increased to make the dimension of the slit lose its comparability with the wavelength, the transmittance of slit decreases, unlike the Drude model's prediction. Thus, at small wavelength, a non-local model should be used.

Bloch's hydrodynamic model gives us the advantage that we can control the transmission of light through the slit by modulating β which depends on the dimensionless parameter r_s specific for each material. In figures 6.15, 6.16 and 6.17, we show how the dielectric constant of the metal, the effective refractive index of the slit and the transmittance of light through the slit change as a function of r_s. In figure 6.15, for a specific wavelength, $\lambda = 350$ nm ($\omega/2\pi = 4.71 \times 10^{15}$ Hz [3.1 eV].), we change β by modifying r_s and find the r_s range where the material behaves like a metal. From figure 6.15, it is found that the dielectric function of the metal has metal properties until $r_s = 5.6$. Hence, we look at the effect of r_s on the effective refractive index of the slit and the transmittance of light for r_s values smaller than this value.

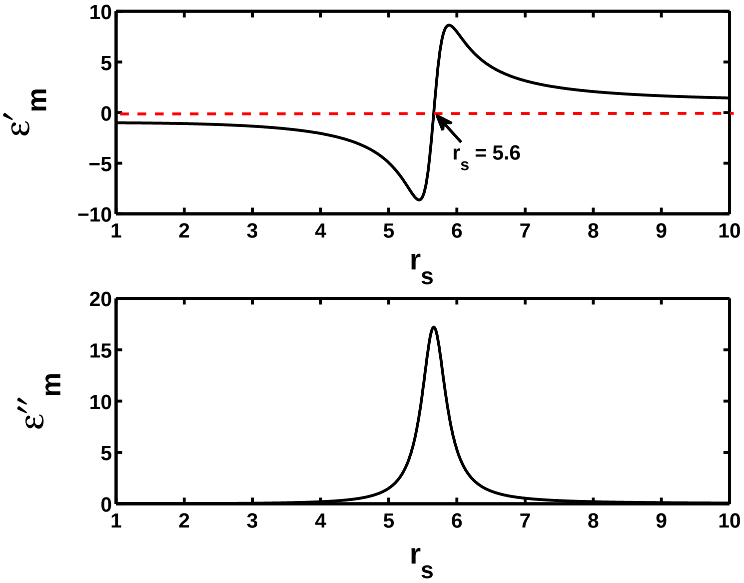

Figure 6.15: Dielectric function of the metal ($\varepsilon_m = \varepsilon'_m - j\varepsilon''_m$) as a function of the dimensionless parameter r_s. The corresponding parameters are $\eta = 1 \times 10^{14}$ Hz (0.42 eV) and $\lambda = 350$ nm.

Figure 6.15 shows that both real and imaginary parts of the dielectric constant of the metal increase in magnitude with r_s for the r_s range, $0 < r_s < 5$ and we do our analysis in this r_s range to avoid the irrelevant results due to the singularity that occurs after $r_s = 5$. The relation between ε' and ε'' is due to a general relation, Kramers-Kronig relation often used to relate the real and imaginary parts of the response functions in physical systems because causality implies the analyticity condition is satisfied and conversely, analyticity implies causality of the corresponding physical system. In other words, with a known real part, we can predict the imaginary part of the dielectric function.

Figure 6.16 shows how the increase in the magnitude of the real part of the dielectric constant causes the real and imaginary parts of the effective refractive index to decrease (this result is predicted from figure 6.4) and how the increase in the magnitude of the imaginary part of the dielectric constant causes the real part of the effective refractive index to decrease and the imaginary part of the effective refractive index to increase (However this increase is not big enough to increase the imaginary part of the effective refractive index which decreases due to the increase in the magnitude of the real part of the dielectric constant which is predicted from figure 6.5).

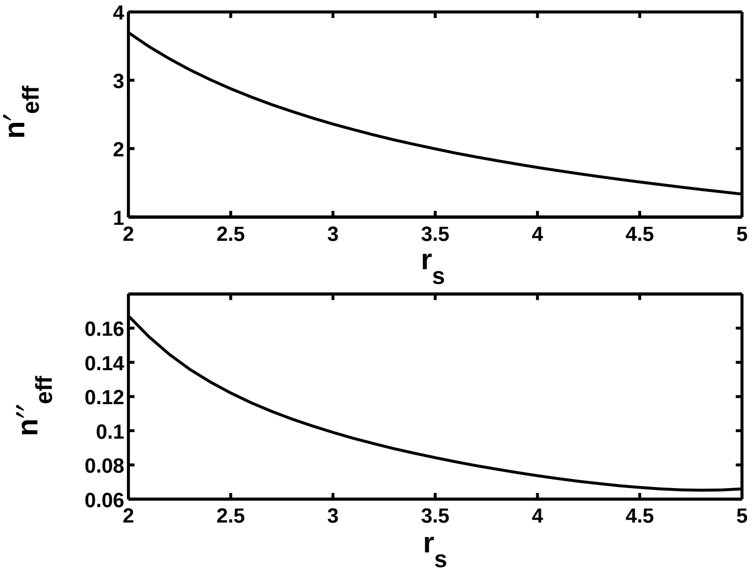

Figure 6.16: Effective refractive index of slit ($n_{eff} = n'_{eff} - jn''_{eff}$) as a function of dimensionless parameter r_s. The corresponding parameters are $\eta = 1 \times 10^{14}$ Hz (0.42 eV), $\lambda = 350$ nm, $r = 80$ nm and $\varepsilon_d = 1$.

Figure 6.17 shows how the transmission of light through the slit on the metal layer is affected by the dimensionless parameter, r_s. The transmission of light through the slit is proportional to r_s which is inversely proportional to the electron density N. Thus, an increase in N should trigger a decrease in the transmission as shown in figure 6.18. The transmission behavior can now be modified by modulating the electron density of the metal which gives us an important advantage to control and focus light using subwavelength circuit elements which have switchable transmission characteristics. This result can be very useful for the experimental studies on subwavelength optics and nano-photonics. Figure 6.18 also shows that the phase of the transmittance has dependence on the electron density. Controlling the phase of the transmission can lead the studies on subwavelength optics where more than one slits are use to analyze the transmission behavior and the electron density dependent phase behavior can result in different images obtained by the nano-apertures embedded in metal layer [23], [24].

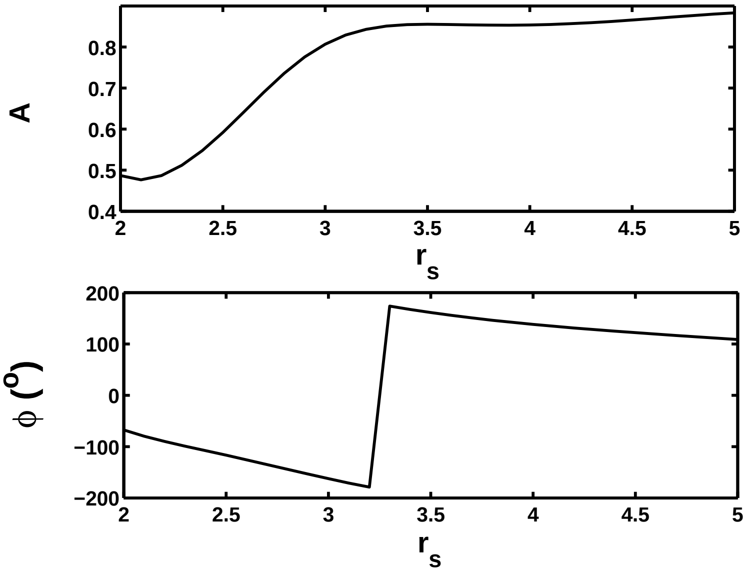

Figure 6.17: Amplitude and phase of the transmittance of light through a single slit embedded in a thin metal layer as a function of dimensionless parameter r_s. The corresponding parameters are $\eta = 1 \times 10^{14}$ Hz (0.42 eV), $\lambda = 350$ nm, $r = 80$ nm and $\varepsilon_d = 1$.

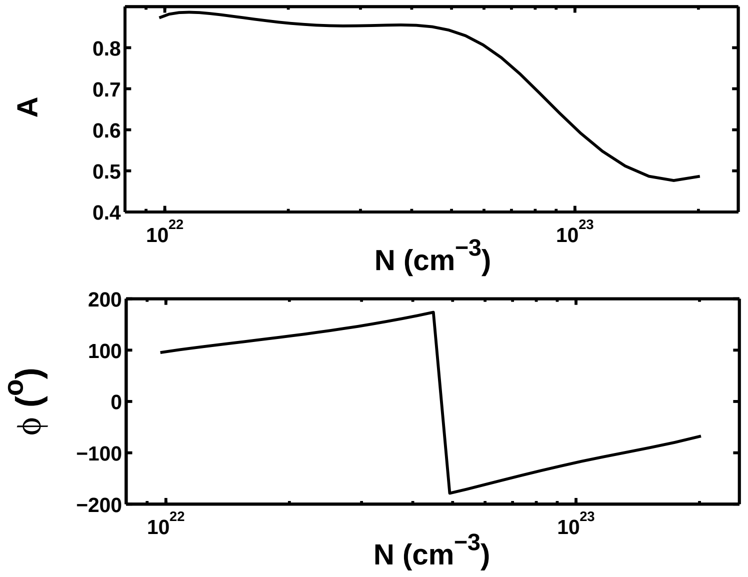

Figure 6.18: Amplitude and phase of the transmittance of light through a single slit embedded in a thin metal layer as a function of the electron density N. The corresponding parameters are $\eta = 1 \times 10^{14}$ Hz (0.42 eV), $\lambda = 350$ nm, $r = 80$ nm and $\varepsilon_d = 1$.

To understand the controllable enhanced transmission of nano-apertures phenomenon, we picturise the system including a nano-slit embedded in a metal sheet in figure 6.19. Surface plasmons are the waves that propagate on the surface of the metal and decay in the direction normal to the surface. Surface plasmons dissipate their energy as they propagate through the surface and disappear when their energy is exhausted. The enhanced transmission issue is related to the surface plasmon formed in the slit region. The higher energy of the surface plasmon is provided, the higher transmission of light through the slit is expected. As shown in figure 6.19, when a planar wave hits the bottom side of the metal, the two edges of the slit act like a dipole which is the source of all kinds of waves. The evanescent fields generated by these dipoles excite the surface plasmon waves and these waves propagate in the slit region. When the surface plasmons propagating in the slit region reach the slit exit, they turn into the propagating fields radiating in radial direction from the top side of the slit. Hence, the total transmitted light we see in the slit exit is the sum of the wave radiated by the surface plasmons and the directly transmitted part of the initial wave from the slit.

The reason behind the decrease in the amplitude of the transmittance with the electron density is that as the electron density increases, the loss of the system increases as well. We can predict this result from the fact that as N increases, the imaginary part of the effective refractive index [2] increases which can be inferred from figure 6.16. As the loss increases, the imaginary part of the surface plasmon wavevector which shows the rate of decay in the wave as it propagates through the medium increases so as the surface plasmon propagates through the slit, it dissipates its energy rapidly when the loss of the system increases.

In Bloch model, β stands for the stiffness coefficient, which determines the extent of the non-local spatial dispersion effects. As the surface electron plasma gets less stiff (higher r_s), it becomes more compressible so that it can support longer wavelength hydrodynamic disturbances with slower speeds. Thus, their associated quanta, the surface plasmons, would have smaller wavenumbers k_{sp} relative to those of more stiff systems. It is known that the surface plasmons with smaller wavenumber are less localized near the metal surface, have longer propagation lengths and are more easily decoupled from the surface into the freely propagating light [26]. In other words, the surface plasmons in less stiff systems could contribute into outgoing light more efficiently. Thus, as r_s increases, in other words, as the

---

[2] Imaginary part of the effective refractive index accounts for the total loss of the system.

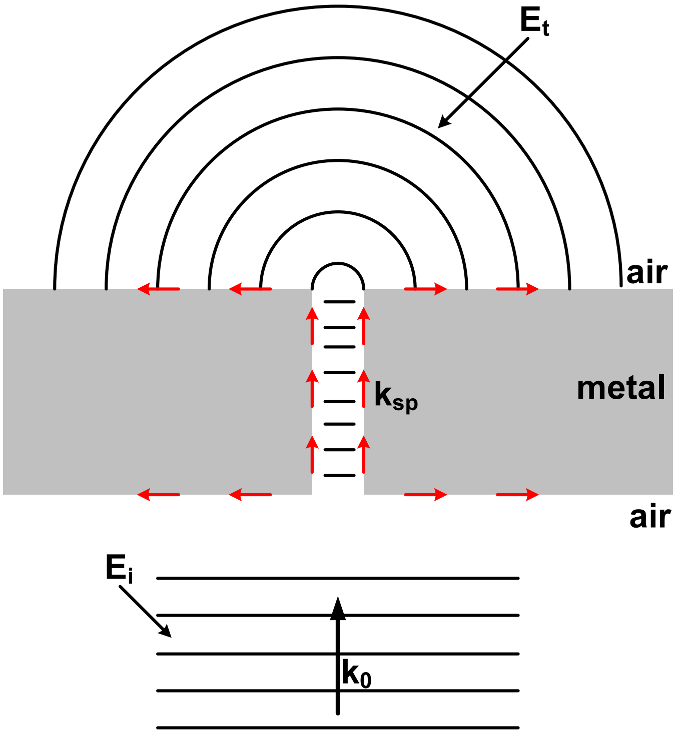

Figure 6.19: Optical transmission through a single slit formed in a metal layer. E_i is the TM polarized incident wave to the bottom side of the metal layer and E_t is the transmitted wave on the upper side of the metal layer due to the surface plasmon generated by the slit and the directly transmitted wave from the slit.

system becomes less stiff, k_{sp} decreases which results in the fact that the transmittance of the slit increases as shown in figures 6.17 and 6.20 - (a). The surface plasmon propagation length L_{sp} shows the distance the surface plasmon travels before attenuating away due to the damping of the electron oscillation. As r_s increases, the real part of the surface plasmon wavevector decreases so the surface plasmon becomes less localized to the surface and the surface plasmon propagation length increases due to the decrease in the resistive damping inside the metal as shown in figure 6.20 - (b). Thus, as r_s increases, the surface plasmon travels longer distance and the surface plasmon excited in the slit region reaches the slit exit with more energy which results in a more enhanced transmission.

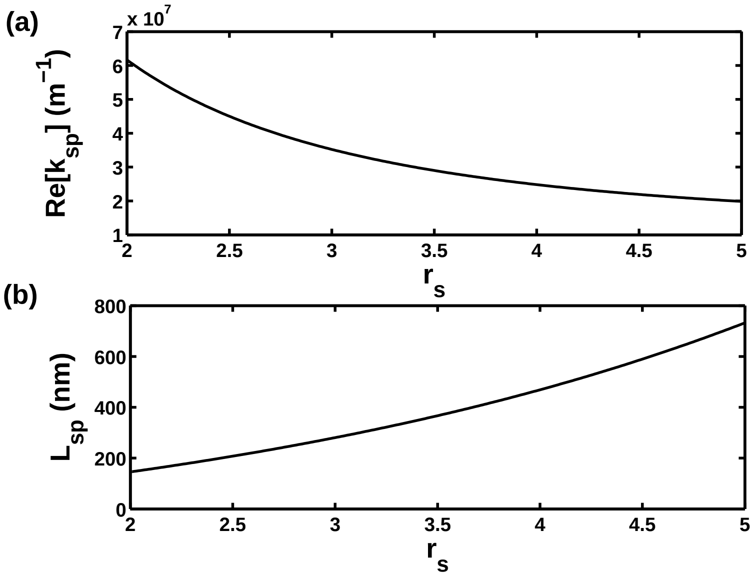

Figure 6.20: (a) Real part of the surface plasmon wavevector and (b) surface plasmon propagation length as a function of dimensionless parameter r_s. The corresponding parameters are $\eta = 1 \times 10^{14}$ Hz (0.42 eV), $\lambda = 350$ nm and $\varepsilon_d = 1$.

6.6 Beam Shaping and Tilting by Metallic Nano-Optic Lenses

Metallic lenses are made from metal layers with curvature structure where several nanoslit elements are embedded in. The idea behind the metallic lenses is that nano-slits with different height allow light transmission from the structure in different phases. Figure 6.22 shows COMSOL Multiphysics simulation of the transmission of light through a three-slit structure schematically shown in figure 6.21.

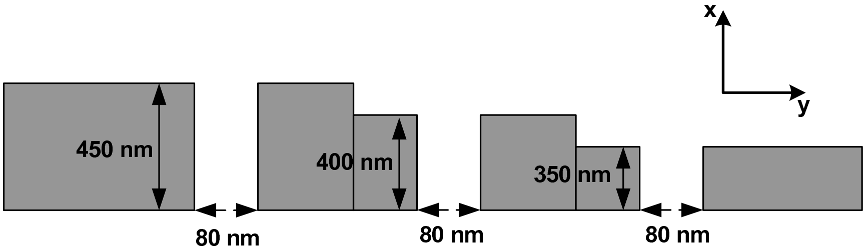

Figure 6.21: Dimension of the three-slit structure.

The COMSOL Multiphysics simulation shows that the transmitted beam propagates along the direction of the thicker side of the metal. The reason of this phenomenon is that different

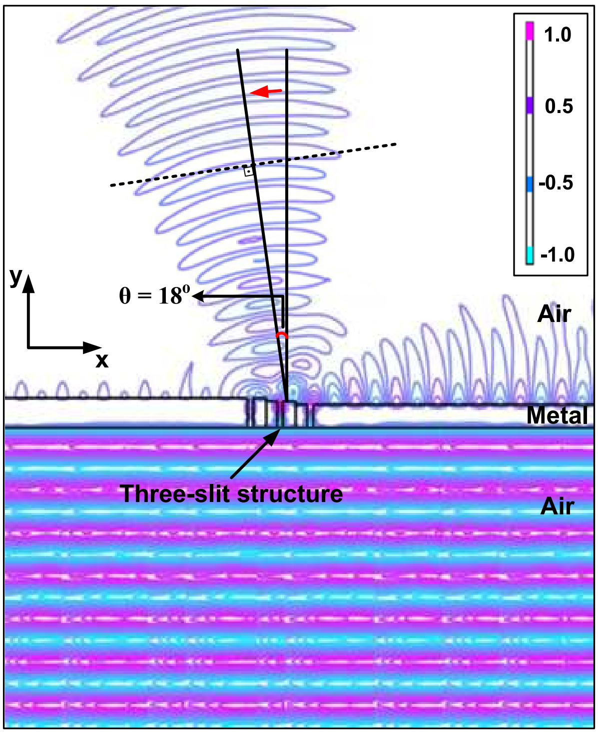

Figure 6.22: COMSOL Multiphysics simulation of the transmission of light through nano-apertures with different heights formed in a metal layer with tapered thickness. A TM-polarized plane wave is shot to the bottom side of the three-slit structure with wavelength of 650 nm. The dielectric constant of the metal is $\varepsilon_m = -16.19 - j1.05$.

heights of slit cause phase retardation. We can write the z-component of the magnetic field shown in figure 6.22 in the far field as a summation of the cylindrical waves formed in each nanoslit [13].

$$H_z(x,y) = \sum_{\alpha} \frac{A_\alpha}{\sqrt{r_\alpha}} e^{-j\phi_\alpha} e^{-jk_0 r_\alpha} \tag{6.23}$$

where $r_\alpha = \sqrt{(x-x_\alpha)^2 + (y-y_\alpha)^2}$ and k_0 is the wave vector of the transmitted beam in the air region. A_α and ϕ_α are, respectively, the amplitude and phase of the transmitted beam formed in the α^{th} slit located at (x_α, y_α) and can be calculated with equation 6.21. The transmitted beam propagates in the direction that satisfies the following phase matching condition at the metal-air interface as shown in figure 6.23 [13].

$$k_{sp} \sin\theta_i = k_0 \sin\theta_t \tag{6.24}$$

where θ_i is the incident angle of the surface plasmon wave to the hypothetical planar surface that comprises the slit apertures and θ_t is the tilt angle of the transmitted beam.

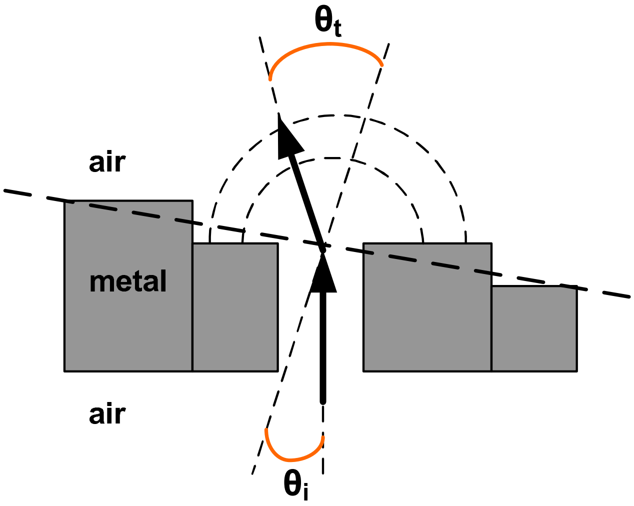

Figure 6.23: Phase matching condition at the metal/air interface.

From the phase matching condition, for the three-slit structure, the transmission angle θ_t is calculated as 17^o, which shows a reasonable match to the angle observed in the COMSOL Multiphysics simulation as 18^o. COMSOL Multiphysics simulation result demonstrates that the nanoslit arrays with tapered metal thickness possess the capability of beam shaping. Using the idea of the fact that the tapered metal layers can deflect beams, we design a convex metallic shape to have two identical but in reverse oriented tapered metallic layers, one to tilt the beam toward right and the other to tilt it toward left to get an overall focused beam. Figures 6.24 shows the COMSOL Mutiphysics simulation of the beam shaping with nanoslit array lenses that have convex profiles in the metal thickness. The dimensions of each lenses are shown in the insets. For the three-slit lens (figure 6.24 - (a)), the incident beam becomes sharply focused right after the lens with a beam waist of 400 nm. In the case of the five-slit lens (figure 6.24 - (b)), the incident beam becomes focused after the lens and remains well collimated with negligible divergence even after many wavelengths of propagation in the far field region. This indicates an increase of focal length in the five-slit lens compared to the three-slit lens [13].

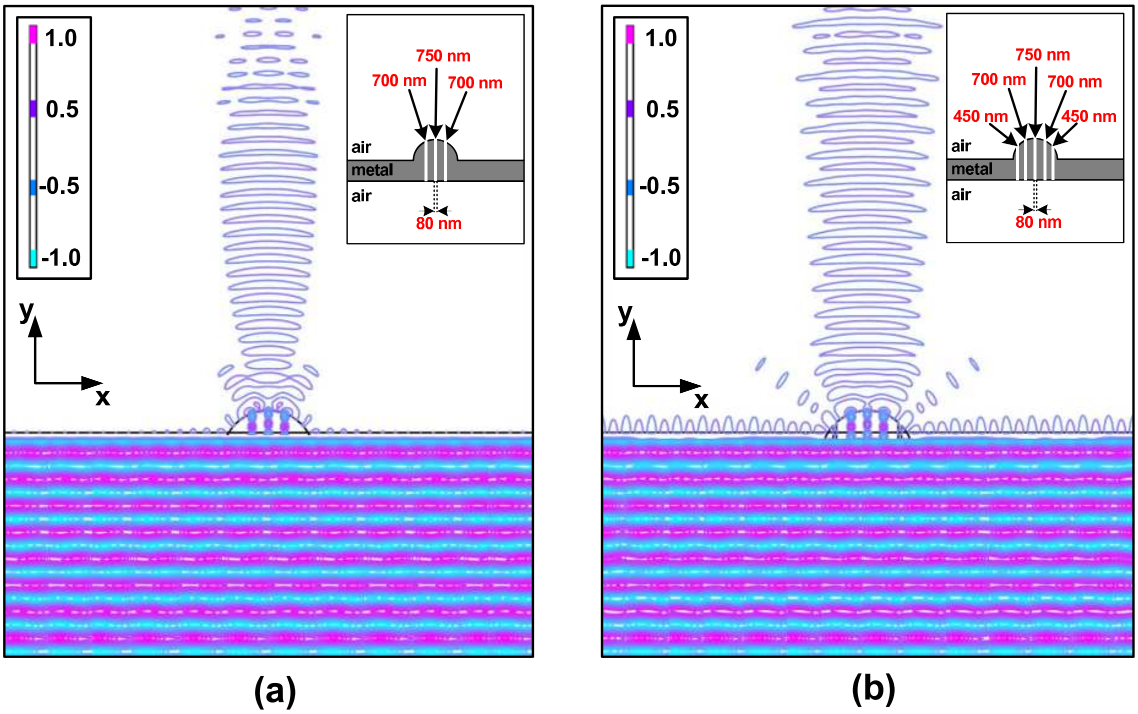

Figure 6.24: COMSOL Multiphysics simulation of beam shaping with a convex metallic lens with (a) three slits and (b) five slits. A TM-polarized light with 650 nm wavelength is incident to the bottom side of the metal layer ($\varepsilon_m = -16.19 - j1.05$). The convex region is designed to accommodate up to five slits (80-nm slit width) with 400-nm slit spacing and slit depth of 450, 700, 750, 700 and 450 nm.

Using Bloch's hydrodynamic model, we can control the power of the surface plasmon that reaches the exit of the nano-aperture where it diffracts into propagating wave. Thus, we have the ability of controlling the transmission of light through the nano-apertures by modifying β parameter which depends on the dimensionless parameter, r_s specific for each material. The idea of the controllable nature of the nano-apertures can be used to determine the beam shaping characteristics of the metallic structures. We use this controllable manner of the transmittance of nano-apertures embedded in metallic structures in the nano-optic lens design by changing the dimensionless parameter r_s. The metallic nano-optic lens to be analyzed is schematically drawn in figure 6.25 - (a).

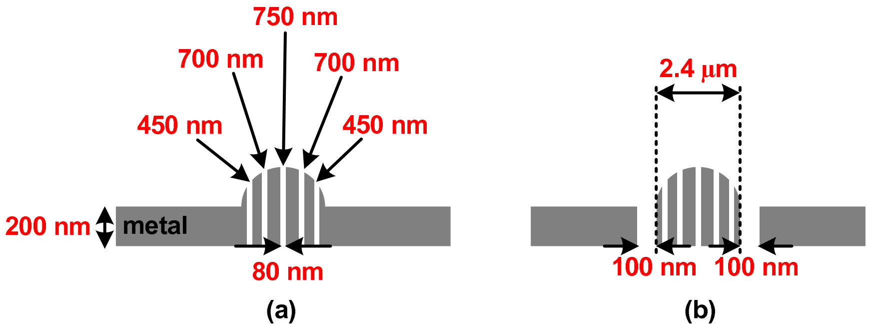

Figure 6.25: The dimension of the metallic nano-optic lens under consideration.

Figure 6.26 - (a) shows that the focal length of the metallic nano-optic lens shown in figure 6.25 - (a) increases and the beam waist decreases with r_s. Therefore, more efficient enhancement of the energy of the transmitted field in less stiff systems results in a narrower beam waist yielding better collimated, tighter beam and longer focal distances.

During the manufacturing process of the metallic nano-optic lens, there might be some experimental problems, i.e. the heights of the slits could be erroneously produced or located which affects the direction of the focused beam. The dislocation of the slits from the central position in the middle of the metal layers changes the beam direction. If these deformations are introduced into the system under control, they can lead to beneficial applications. In figure 6.28, we show two snapshots of the system schematically drawn in figure 6.27 that we move the location of the metal parts around the slits in vertical direction which changes the convex metallic shape shown in figure 6.28 - (a) to a tapered configuration as shown in figure 6.28 - (b). The focused beam can now be tilted toward the ticker side of the metal and if this process is done continuously from one side to the other, whole system can be used as a metallic nano-scanner. In practice, nano positioning of the rods may be achieved by using piezo-electric transducers. As the slits shift their vertical positions, from one tapered configuration to another, the beam gets deflected over an angular range of 56 degrees.

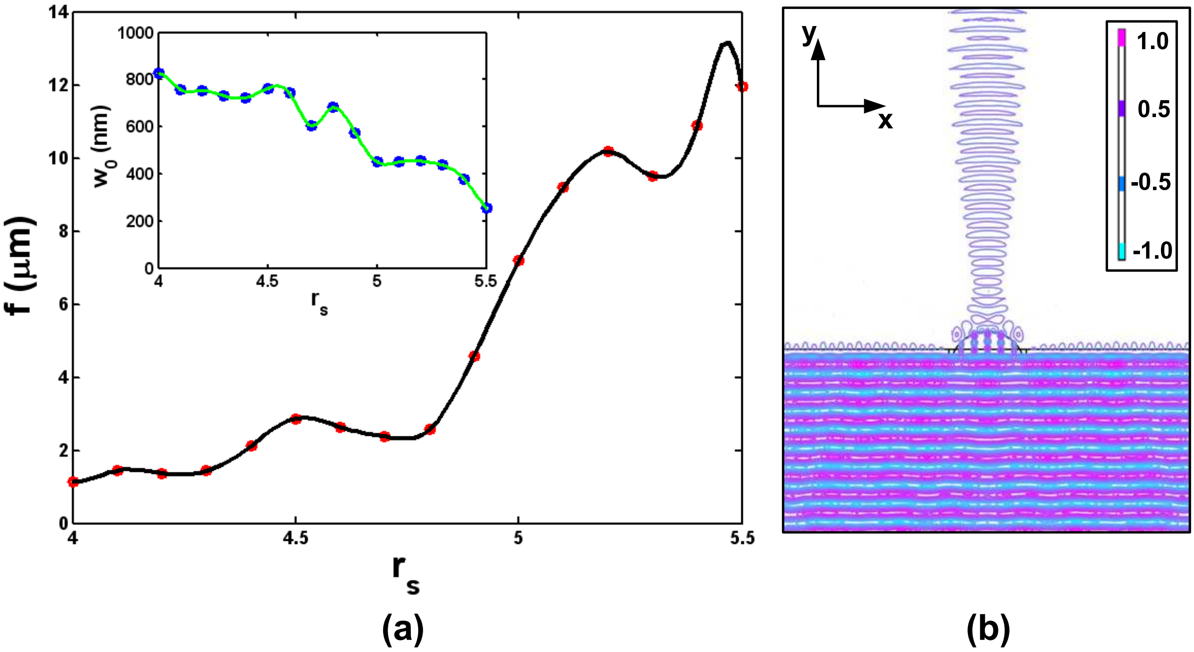

Figure 6.26: (a) Focal length and beam waist (inset plot) of the metallic nano-optic lens schematically drawn in figure 6.25 - (a) as a function of the dimensionless parameter r_s and (b) H_z distribution of the system shown for $r_s = 5.42$ of silver. A TM-polarized planar wave with wavelength of 350 nm is incident to the bottom side of the lens. $\eta = 1 \times 10^{14}$ Hz (0.42 eV)

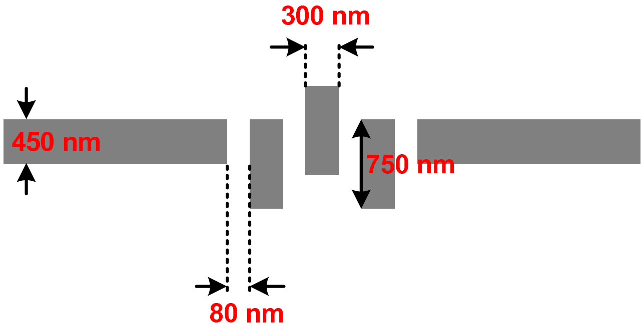

Figure 6.27: The dimension of the nano-scanner under consideration.

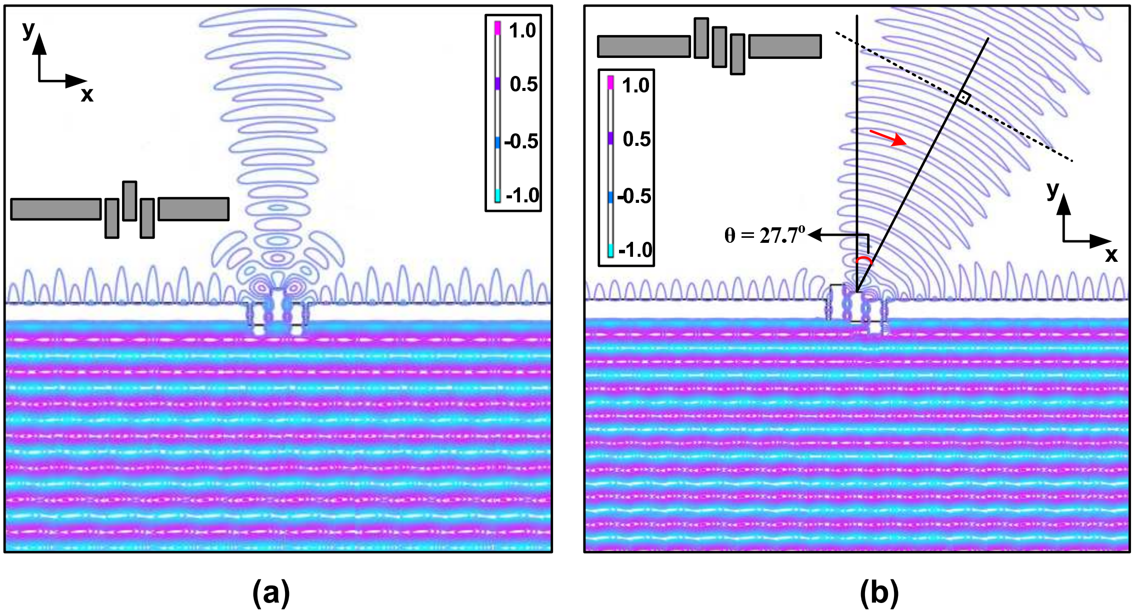

Figure 6.28: Beam tilting by a nano-scanner with movable slits. COMSOL Multiphysics simulation of tilting the focused beam with the nano-scanner made of silver ($r_s = 5.42$) where the slits are moved vertically between two metal layers is shown. Figure (a) shows a snapshot of the H_z distribution in the system when the slits have a convex shape and figure (b) shows a snapshot of the H_z distribution in the system when the slits have a ladder shape. A TM-polarized planar wave with wavelength of 350 nm is incident to the bottom side of the lens. $\eta = 1 \times 10^{14}$ Hz (0.42 eV)

In figure 6.29, we show a system consisting of a metallic nano-optic lens moving horizontally between two metal layers as schematically shown in figure 6.25 - (b). The beam is first focused after the system when the convex metallic shape is in the middle of the metal layers. We show that when the convex structure moves toward right, the focused beam tilts in the right up to 10 degrees. The reason behind this phenomenon is that when the convex metallic structure moves toward right, the slit formed in the left of the convex shape starts to excite surface plasmon and the transmission of light through the slit in that region is enhanced. In the upper side of the metallic nano-optic lens, the transmitted beam enhanced via surface plasmon formed in the slit region interferes with the focused beam after the metallic nano-optic lens. Thus, whole transmitted beam tilts toward the direction where the convex metallic structure moves to. If this process is done continuously from one side to the other, whole system can be used as a metallic nano-scanner for smaller angular range.

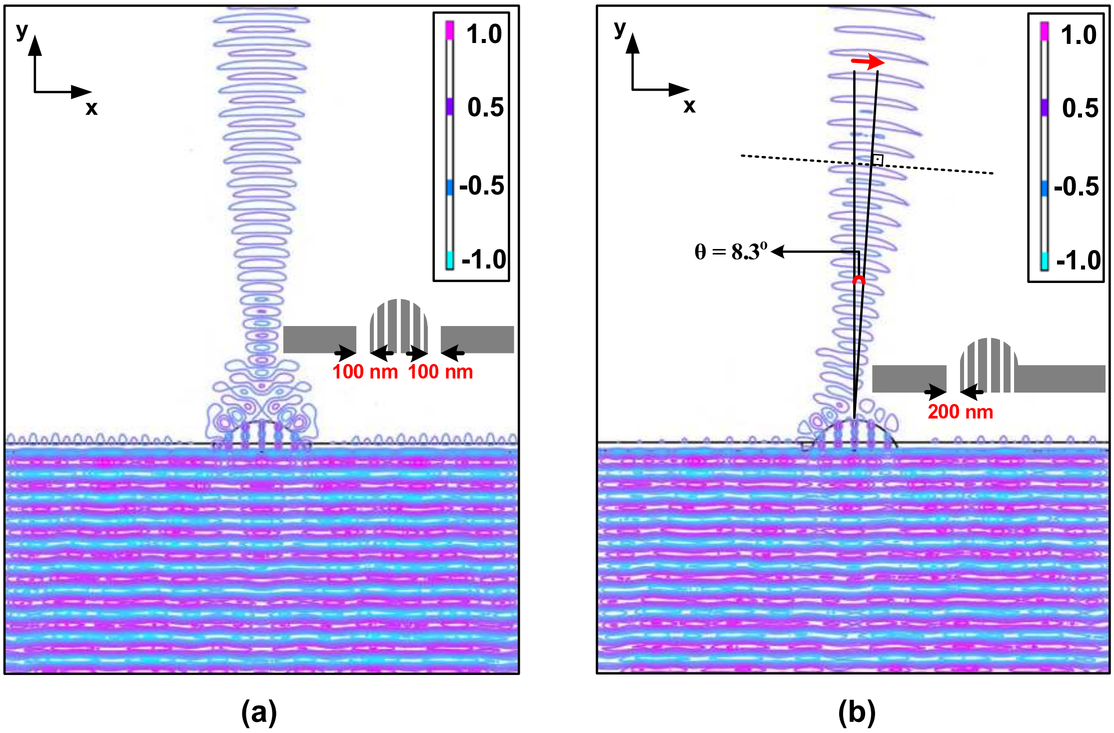

Figure 6.29: COMSOL Multiphysics simulation of tilting the focused beam with the metallic nano-optic lens where the convex metallic structure is moved between two metal layers. Figure (a) shows a snapshot of the system when the convex shape is in the middle of the two metal layers and figure (b) shows a snapshot when the convex shape next to the metal in the right side. In figure, H_z distribution of the system is shown. A TM-polarized planar wave with wavelength of 350 nm is incident to the bottom side of the lens where $\eta = 1 \times 10^{14}$ Hz (0.42 eV), $r_s = 5.42$ (silver) and slit width = 80 nm.

6.7 Beam Shaping by Metallic Textured Surfaces

Single nano-apertures show enhanced transmission when surrounded by a periodic structure [2]. In figure 6.30 - (a), we show a COMSOL Multiphysics simulation of a system where a nano-slit is embedded in a metal layer with a periodically textured surface on top. The surface plasmon generated in the slit region propagates through it and reaches the slit exit. Then it starts to propagate through the upper surface of the metal and hits the ears. When the surface plasmon reaches the grooves between two ears, it diffracts into radial distribution and the field distribution generated by each groove is summed after the textured surface. Hence, whole structure behaves like an antenna array. In figure 6.30 - (a), we show that the beam waist of the focused beam after the structure decreases with r_s, in other words, the beam becomes more focused and well collimated after the textured surface.

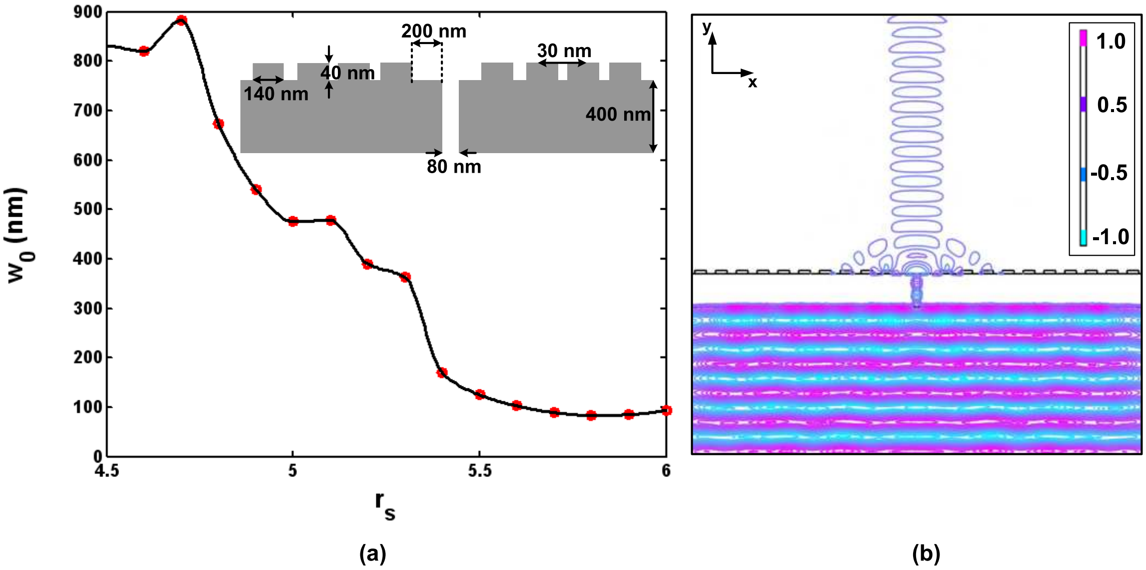

(a) (b)

Figure 6.30: (a) COMSOL Multiphysics simulation of beam shaping via a metallic structure with textured surface as a function of r_s and (b) H_z distribution of the system for $r_s = 5.42$ of silver. A TM-polarized planar wave with wavelength of 350 nm is incident to the bottom side of the lens where the slit width = 80 nm and the metal thickness = 200 nm. $\eta = 1 \times 10^{14}$ Hz (0.42 eV)

Chapter 7

SUMMARY OF RESEARCH

In this thesis, we have examined the non-local optical effects in extraordinary transmission of light through subwavelength nano-apertures. We have first established the background for the non-local effects in surface plasmon related enhanced transmission of light using Bloch's hydrodynamic model and then applied the outcome of the theory to improve transmission, focusing, and scanning properties of metallic nano-lenses by varying the lens geometry and the stiffness coefficient which determines the extent of non-local contributions.

We have shown that Bloch model is better in accounting for the observed dielectric response of the metals, such as silver, than the Drude model. We have then explored the surface plasmon dispersion relation while the non-local effects are taken into account. We have found new surface plasmon excitations near plasma frequency which results in new contributions in subwavelength metallic structures working in higher frequencies.

In addition to earlier results on the beam focusing characteristics of nano-lenses depending on the number of nano-slits, slit width, and the dielectric constant of the material that fills the slit region, we have modified the material parameters defined by Bloch model which affects the enhanced transmission of light through nano-apertures embedded in metallic structures to control the focus length of nano-lenses.

We have then shown two methods, one of which is controlling the relative vertical positions of the metallic nano-rods which enables beam scanning and the other is horizontal position control which leads to small angular scanning both of which can be achieved, in principle, by use of piezoelectric transducers.

Taking into account the spatial dispersion effects, it is shown that nano-lens can operate in the near plasma frequency regime of the metal optics and this dynamical control on the beam direction can lead to other applications of nano-lenses such as nano-scanners or can be exploited for high density memory reading and writing. In the final analysis, combination with the previous ideas on active control of nano-lenses, we expect that our results could lead to optimum designs of nano-lenses and open paths for novel applications.

Appendix A

GENERALIZED PENCIL OF FUNCTION METHOD

In this section, a linear method to approximate the functions by sum of complex exponentials is introduced. Generalized Pencil of Function (GPOF) method is a more efficient method both computationally and noise sensitively than Prony and Pencil of Function methods which yield the solution in two steps, the first step is solving the matrix equation and the second step is finding the roots of the polynomials.
In general, electromagnetic signals are described by the following equation

$$y(t) = \sum_{i=1}^{M} R_i e^{s_i t} \qquad 0 \leq t \leq T \tag{A.1}$$

R_i = residue,
s_i = complex pole of the signal ($s_i = -\alpha_i + j\omega_i$)
α_i = damping factors
ω_i = angular frequencies ($\omega_i = 2\pi f_i$)

After sampling with the sampling period T_s, the signal can be written as

$$y(kT_s) = \sum_{i=1}^{M} R_i z_i^k \qquad for\, k = 0, ..., N-1 \tag{A.2}$$

where $z_i = e^{s_i T_s} = e^{(-\alpha_i + j\omega_i)T_s}$ for $i = 1, 2......, M$ [1]

Now the problem turns into a problem of finding the optimal values of M, R and s from the sampled signal, $y(kT_s)$. To solve that problem, there are two main methods, the polynomial method (Prony Type) and GPOF method. In polynomial method, the two-step method, a matrix equation is solved for the coefficients of a polynomial whose roots are z_i, on the other hand, in GPOF method, one step method, z_is are found as the solution of the generalized eigenvalue problem.

---

[1] z_i is the complex pole in the Z domain

GPOF method extracts the poles from an exponentially damped sinusoids and it treats the pole extraction problem as a general eigen-analysis problem.
Consider the following set of information vectors $\mathbf{y}_0, \mathbf{y}_1, ..., \mathbf{y}_L$ where [2]

$$\mathbf{y}_i = [y_i, y_{i+1}, ..., y_{i+N-L-1}]^T \tag{A.3}$$

Let $[Y]$ be the data matrix formed by the noisy data, $y(t)$, described by equation (A.1)

$$[Y] = [\mathbf{y}_0, \mathbf{y}_1, ..., \mathbf{y}_L] \tag{A.4}$$

Define two $(N-L) \times L$ matrices $[Y_1]$ and $[Y_2]$

$$\begin{aligned} [Y_1] &= [\mathbf{y}_0, \mathbf{y}_1, ..., \mathbf{y}_{L-1}] \\ [Y_2] &= [\mathbf{y}_1, \mathbf{y}_2, ..., \mathbf{y}_L] \end{aligned} \tag{A.5}$$

The matrix forms of $[Y]$, $[Y_1]$ and $[Y_2]$ can be written as in the following.

$$\begin{aligned} [Y] &= \begin{bmatrix} y(0) & y(1) & \dots & y(L) \\ y(1) & y(2) & \dots & y(L+1) \\ \vdots & \vdots & \vdots & \vdots \\ y(N-L-1) & y(N-L) & \dots & y(N-1) \end{bmatrix}_{(N-L)\times(L+1)} \\ [Y_1] &= \begin{bmatrix} y(0) & y(1) & \dots & y(L-1) \\ y(1) & y(2) & \dots & y(L) \\ \vdots & \vdots & \vdots & \vdots \\ y(N-L-1) & y(N-L) & \dots & y(N-2) \end{bmatrix}_{(N-L)\times L} \\ [Y_2] &= \begin{bmatrix} y(1) & y(2) & \dots & y(L) \\ y(2) & y(3) & \dots & y(L+1) \\ \vdots & \vdots & \vdots & \vdots \\ y(N-L) & y(N-L+1) & \dots & y(N-1) \end{bmatrix}_{(N-L)\times L} \end{aligned} \tag{A.6}$$

In GPOF method, the information matrix is divided into two matrixes because of the fact that in this method, the aim is to reach the eigenvalues of the system. Figure A.1 shows the Error Measurement System which gets the information of the system by checking and comparing the data of input $u(t)$ and output $y(t)$.

---

[2] $[\,]^T$ denotes the transpose of a matrix.

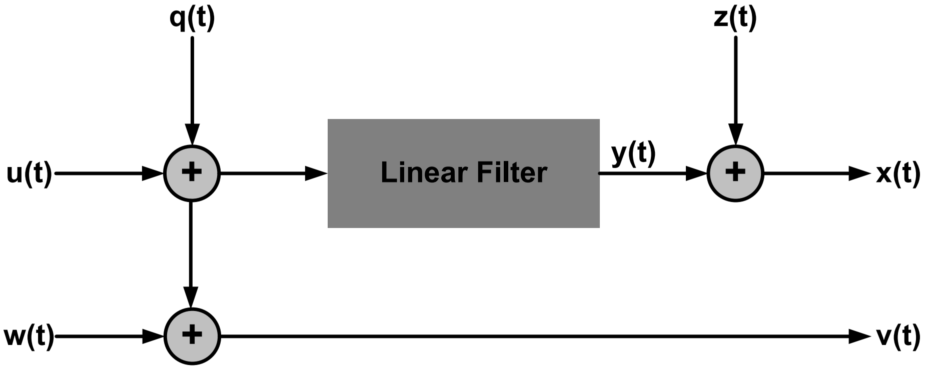

Figure A.1: Noise Measurement System

We can describe the time response of the system as

$$h(t) = \sum_{i=1}^{n} A_i e^{\lambda_i t} \tag{A.7}$$

where λ_i is the pole of the system.

While achieving the output of the system, we should add the noise data to the convolution result as in the following.

$$y(t) = h(t) * [u(t) + q(t)] = \sum_{i=1}^{n} e^{\lambda_i t} A_i \int_0^t e^{-\lambda_i \tau}[u(\tau) + q(\tau)] d\tau \tag{A.8}$$

The set of pencil is

$$y_1(t) - \lambda y_2(t), ..., y_n(t) - \lambda y_{n+1}(t); u_2(t), ..., u_{n+1}(t) \tag{A.9}$$

is dependent if λ becomes one of the system poles.

Ignoring the noisy data in the system, we can rewrite equation A.8 as below.

$$y(t) = \sum_{i=1}^{n} e^{\lambda_i t} A_i \int_0^t e^{-\lambda_i \tau} u(\tau) d\tau \tag{A.10}$$

The output of the system can be described as follows.

$$y(t) = \sum_{j=1}^{n} A_j p_j(t) \tag{A.11}$$

where

$$p_j(t) = e^{\lambda_j t} \int_0^t e^{-\lambda_j \tau} u(\tau) d\tau \qquad j = 1, ..., n \tag{A.12}$$

If we consider the filter below

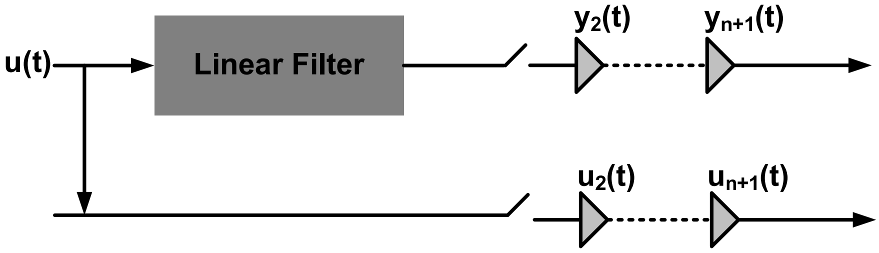

Figure A.2: Filter System

The input, $u(t)$, and the output, $y(t)$, of the system can be represented below.

$$u_{i+1}(t) = \int_0^t u_i(\tau)d\tau \qquad i = 1, ..., n \tag{A.13}$$

$$y_{i+1}(t) = \int_0^t y_i(\tau)d\tau \qquad i = 1, ..., n \tag{A.14}$$

Using equations A.11, A.12, A.13 and A.14, the following relationship can be found.

$$y_{i+1}(t) = \sum_{j=1}^{n} A_j [\frac{p_j(t)}{\lambda_j^i} - \sum_{m=1}^{i} \frac{u_{m+1}(t)}{\lambda_j^{i-m+1}}] \qquad i = 1, ..., n \tag{A.15}$$

Equation A.15 implies that the pencil sets $y_1(t) - \lambda y_2(t), ..., y_n(t) - \lambda y_{n+1}(t); u_2(t), ..., u_{n+1}(t)$ are linearly dependent when λ takes the same value of one of the system poles due to the fact that our pencil set bounds the independent set of functions $A_1 p_1(t), ..., A_n p_n(t); u_2(t), ..., u_{n+1}(t)$ by the $2n \times 2n$ matrix as shown below.

$$\begin{bmatrix} E & X \\ 0 & I \end{bmatrix} \tag{A.16}$$

I = identity matrix of order n,

0 = zero matrix of order n

Here our matrix assumption depends on the E matrix;

$$E = [e_{ij} = (1 - \lambda/\lambda_j)/\lambda_j^{i-1}] \qquad i, j = 1, ..., n \tag{A.17}$$

For GPOF Method, when $M < L < N - M$, z_i becomes eigenvalue of the system (λ_i of equation A.21) of the matrix pencil $[Y_2] - z[Y_1]$. [3]

The two matrices $[Y_1]$ and $[Y_2]$ can now be described as follows.

$$\begin{aligned} [Y_2] &= [Z_1][R][Z_0][Z_2] \\ [Y_1] &= [Z_1][R][Z_2] \end{aligned} \tag{A.19}$$

where [4]

$$[Z_1] = \begin{bmatrix} 1 & 1 & \dots & 1 \\ z_1 & z_2 & \dots & z_M \\ \vdots & \vdots & \vdots & \vdots \\ z_1^{N-L-1} & z_2^{N-L-1} & \dots & z_M^{N-L-1} \end{bmatrix}_{(N-L)\times M} \tag{A.20}$$

$$\begin{aligned} [Z_2] &= \begin{bmatrix} 1 & z_1 & \dots & z_1^{L-1} \\ 1 & z_2 & \dots & z_2^{L-1} \\ \vdots & \vdots & \vdots & \vdots \\ 1 & z_M & \dots & z_M^{L-1} \end{bmatrix}_{M\times L} \\ [Z_0] &= diag[z_1, z_2, ..., z_M] \\ [R] &= diag[R_1, R_2, ..., R_M] \end{aligned}$$

Now we can write the pencil matrix equation $[Y_2] - \lambda[Y_1]$ as

$$[Y_2] - \lambda[Y_1] = [Z_1][R]([Z_0] - \lambda[I])[Z_2] \tag{A.21}$$

For equation A.21, when the following condition exists

$$\lambda = z_i \qquad i = 1, 2, ..., M \tag{A.22}$$

the i^{th} row of $[Z_0] - \lambda[I]$ becomes zero and the rank of this matrix becomes $M - 1$. When $[Z_0] - \lambda[I]$ is zero, the two matrices, $[Z_1]$ and $[Z_2]$ are annihilated. Hence z_i is found as the generalized eigenvalues of the matrix pair $([Y_2]; [Y_1])$.

---

[3] The classical mathematical eigenvalue problem is defined as the solution of the following equation.

$$[A]\mathbf{v}_n = \lambda_n \mathbf{v}_n \qquad n = 1, ..., M \tag{A.18}$$

where λ is the eigenvalue and $\mathbf{v}_n$ is the eigenvector of the matrix $[A]$.

[4] diag[ ] represents an $M \times M$ diagonal matrix.

Now the problem turns into finding the eigenvalues of the matrix pencil problem. We first begin with writing the equation below. [5]

$$\begin{aligned} [Y_1]^+[Y_2] &= [Z_2]^+[R]^{-1}[Z_1]^+[Z_1][R][Z_0][Z_2] \\ &= [Z_2]^+[Z_0][Z_2] \end{aligned} \tag{A.23}$$

Then there exists the vector, p_i, the generalized eigenvector of $[Y_1] - z[Y_2]$. [6]

$$\begin{aligned} [Y_1]^+[Y_1]\mathbf{p}_i &= \mathbf{p}_i && i = 1, ..., M \\ [Y_1]^+[Y_2]\mathbf{p}_i &= z_i\mathbf{p}_i && i = 1, ..., M \end{aligned} \tag{A.24}$$

The best way to compute pseudo inverse is to use singular value decomposition of $[Y_1]$ as shown below. [7]

$$[Y_1] = \sum_{i=1,M} s_i\mathbf{u}_i\mathbf{v}_i^H = [U][S][V]^H \tag{A.25}$$

$$[Y_1]^+ = [V][S]^{-1}[U]^H \tag{A.26}$$

$[U] = [\mathbf{u}_1, ..., \mathbf{u}_M]$ (Matrix containing the left singular vectors of $[Y_1]$)
$[V] = [\mathbf{v}_1, ..., \mathbf{v}_M]$ (Matrix containing the right singular vectors of $[Y_1]$)
$[S] = diag[s_1, ..., s_M]$

When data $y(t)$ are noisy, we choose the singular values, $s_1, ..., s_M$, to be the M largest values of $[Y_1]$. ($[Y_1]^+$ is the truncated pseudo inverse of $[Y_1]$.)
Substituting equation A.26 into equation A.25 and multiplying the result by $[V]^H$, we get

$$([Z] - z_i[I])\mathbf{z}_i = 0 \qquad i = 1, ..., M \tag{A.27}$$

where $[Z] = [S]^{-1}[U]^H[Y_2][V]$ and $\mathbf{z}_i = [V]^H\mathbf{p}_i$. $[Z]$ is an $M \times M$ matrix, z_i and $\mathbf{z}_i$ are eigenvalue and eigenvector of $[Z]$ respectively.
The optimal choice of M can be done with the following procedure. The SVD of $[Y]$ is shown below.

$$[Y] = [U][S][V]^H \tag{A.28}$$

---

[5] $[\,]^+$ denotes the pseudo-inverse.

[6] $\mathbf{p}_i = [p_i, p_{i+1}, ..., p_{i+N-L-1}]^T$

[7] $[\,]^H$ denotes the conjugate transpose of a matrix.

where $[U]$ and $[V]$ are unitary matrices composed of the eigenvectors of $[Y][Y]^H$ and $[Y]^H[Y]$ respectively and $[S]$ is the diagonal matrix composed of the singular values of $[Y]$, such that

$$[U]^H[Y][V] = [S] \tag{A.29}$$

After finding the singular values of $[Y]$, we start to compare the ratio of the different singular values. Consider the singular value s_c such that

$$s_c/s_{max} \approx 10^{-p} \tag{A.30}$$

where p is the number of the significant decimal digits in the data. When the data are accurate up to n significant digits, the ratio of the singular values in equation A.30 becomes lower than the value, 10^{-n}, then these singular values are noisy singular values and they should not be used to reconstruct the data.

$[V']$ is the filtered matrix which is constructed after selecting the value, M and filtering the data, in other words, it contains only M dominant right singular vectors of $[V]$.

$$[V'] = [v_1, v_2, ..., v_M] \tag{A.31}$$

The two matrices, $[Y_1]$ and $[Y_2]$ turn into

$$\begin{aligned}[Y_1] &= [U][S'][V_1']^H \\ [Y_2] &= [U][S'][V_2']^H\end{aligned} \tag{A.32}$$

where $[S']$ is obtained from the M columns of $[S]$ corresponding to the M dominant singular values.

Thus, the eigenvalues of the following matrix for the noiseless matrix, $[Y]$

$$([Y_2] - \lambda[Y_1])_{L\times M} \Rightarrow ([Y_1]^+[Y_2] - \lambda[I])_{M\times M} \tag{A.33}$$

are equivalent to the eigenvalues of the matrix below.

$$([V_2'] - \lambda[V_1']^H) \Rightarrow ([V_1']^H)^+([V_2']^H)^+ - \lambda[I] \tag{A.34}$$

The algorithm provides the minimum variance when estimating z_i in the presence of noise. After finding M and z_i, R_i can be found from the following matrix solution.

$$\begin{bmatrix} y(0) \\ y(1) \\ \vdots \\ y(N-1) \end{bmatrix} = \begin{bmatrix} 1 & 1 & \dots & 1 \\ z_1 & z_2 & \dots & z_M \\ \vdots & \vdots & \vdots & \vdots \\ z_1^{N-L} & z_2^{N-L} & \dots & z_M^{N-L} \end{bmatrix} \begin{bmatrix} R_1 \\ R_2 \\ \vdots \\ R_M \end{bmatrix} \tag{A.35}$$

VITA

Arif Engin Çetin was born in Antalya, Turkey on July 15, 1983. He has received the B.S. degree in Electrical and Electronics Engineering in June 2007 and the M.S. degree in Electrical and Computer Engineering in June 2009 from Koç University, İstanbul, Turkey. Since September 2007, he has been a research and teaching assistant at Koç University, Electrical and Computer Engineering Department. He is a member of SPIE (International Society for Optical Engineering) and OSA (Optical Society of America). His research interests include nanophotonics, surface plasmons, plasmonic structures, computational electromagnetics, metamaterials and photonic band-gap structures. He will pursue his researches at Boston University, USA as a PhD student.

BIBLIOGRAPHY

[1] L. M. Moreno, F. J. Garcia Vidal, H. J. Lezec, K. M. Pellerin, T. Thio, J. B. Pendry and T. W. Ebbesen, "Theory of extraordinary optical transmission through subwavelength hole array," *Physical Review Letters* **86,** pp. 1114-1117, 2001.

[2] W. L. Barnes, A. Dereux and T. W. Ebbesen, "Surface plasmon subwavelength optics," *Nature* **424,** pp. 824-830, 2003.

[3] R. H. Ritchie, "Plasma losses by fast electrons in thin films," *Physical Review Letters* **106,** pp. 874-881, 1957.

[4] A. V. Zayats, I. I. Smolyaninov and A. A. Maradudin, "Nano-optics of surface plasmon polaritons," *Physics Reports* **408,** pp. 131-314, 2004.

[5] W. L. Barnes, "Surface plasmon-polariton length scales: a route to sub-wavelength optics subavelength optics," *Journal of Optics* **8,** pp. 87-93, 2006.

[6] N. Kinayman and M. I. Aksun, "Modern Microwave Circuits," Artech House, Boston, 2005.

[7] V. Veselago, L. Braginsky, V. Shklover and C. Hafner, "Negative refractive index materials," *Journal of Computational and Theoretical Nanoscience* **3,** pp. 1-30, 2006.

[8] J. B. Pendry, A. J. Holden, W. J. Stewart, I. Youngs, L. Braginsky, V. Shklover and C. Hafner, "Extremely low frequency plasmons in metallic mesostructures," *Physical Review Letters* **76,** pp. 4773-4776, 1996.

[9] J. B. Pendry, A. J. Holden, D. J. Robbins and W. J. Stewart, "Magnetism from conductors and enhanced nonlinear phenomena," *IEEE Transactions on Microwave and Techniques* **47,** pp. 2075-2084, 1999.

[10] Y. Huang and L. Gao, "Left-handed material containing material spherical and non-spherical metallic and magnetic particles," *Physics Letters A* **328,** pp. 225-231, 2004.

[11] J. M. Pitarke, V. M. Silkin, E. V. Chulkov and P. M. Echenique, "Theory of surface plasmons and surface-plasmon polaritons," *Reports on Progress in Physics* **70,** pp. 1-87, 2006.

[12] A. L. Fetter and J. D. Walecka, "Quantum Theory of Many-Particle Systems," McGraw-Hill, New York, 1971.

[13] Z. Sun and H. K. Kim, "Refractive transmission of light and beam shaping with metallic nano-optic lenses," *Applied Physics Letters* **85,** pp. 642-644, 2004.

[14] R. Gordon and A. G. Brolo, "Increased cut-off wavelength for a subwavelength hole in a real metal," *Optics Express* **13,** pp. 1933-1938, 2005.

[15] R. Gordon, "Ligth in a subwavelength slit in a metal: Propagation and reflection," *Physical Review B* **73,** pp. 153405, 2006.

[16] J. S. Kaur, Z. Sun, J. Wuenschell and H. K. Kim, "High-sensitivity surface plasmon resonance spectroscopy based on a metal nanoslit array," *Applied Physics Letters* **88,** pp. 243105, 2006.

[17] Y. Hua and T. K. Sarkar, "Generalized pencil-of-function method for extracting poles of an EM system from its transient responce," *IEEE Transactions on Antennas and Propagation* **37,** pp. 229-234, 1989.

[18] G. Grosso and G. P. Parravicini, "Solid State Physics," Academic Press, New York, 2000.

[19] I. R. Hooper and J. R. Sambles, "Surface plasmon polaritons on thin-slab metal gratings," *Physical Review B* **67,** pp. 235404, 2003.

[20] W. L. Barnes, W. A. Murray, J. Dintinger, E. Devaux and T. W. Ebbesen, "Surface plasmon polaritons and their role in the enhanced transmission of light through periodic

arrays of subwavelength holes in a metal film," *Physical Review Letters* **92,** pp. 107401, 2004.

[21] U. Schroter and D. Heitmann, "Surface-plasmon-enhanced transmission through metallic gratings," *Physical Review B* **58,** pp. 419-421, 1998.

[22] K. G. Lee and Q-Han Park, "Coupling of surface plasmon polaritons and light in metallic nanoslits," *Physical Review Letters* **95,** pp. 103902, 2005.

[23] H. F. Schouten, N. Kuzmin, G. Dubois, T. D. Visser, G. Gbur, P. F. A. Alkemade, H. Blok and G. W t Hooft, "Plasmon-assisted two-slit transmission: Youngs experiment revisited," *Physical Review Letters* **94,** pp. 053901, 2005.

[24] C. H. Gan, G. Gbur and T. D. Visser, "Surface plasmons modulate the spatial coherence of light in Youngs interference experiment," *Physical Review Letters* **98,** pp. 043908, 2007.

[25] J. M. Pitarke, V. M. Silkin, E. V. Chulkov and P. M. Echenique, "Surface plasmons in metallic structures," *Journal of Optics A: Pure and Applied Optics* **7,** pp. 73-84, 2004.

[26] D. R. Smith and F. R. Fickett, "Low-temperature properties of silver," *Journal of Research of the National Institute of Standards and Technology* **100,** pp. 119-171, 1995.

[27] T. W. Ebbesen, C. Genet and S. I Bozhevolnyi, "Surface plasmon circuitry," *Physics Today* **61,** pp. 44-50, 2008.

[28] P. Lalanne and J. P. Hugonin, "Interaction between optical nano-objects at metallo-dielectric interfaces," *Nature Physics* **2,** pp. 551-556, 2006.

[29] P. Lalanne, J. P. Hugonin and J. C. Rodier, "Theory of surface plasmon generation at nanoslit apertures," *Physical Review Letters* **95,** pp. 263902, 2005.

[30] N. W. Ashcroft and N. D. Mermin, "Solid State Physics," Holt, Rinegart and Winston, New York, 1976.

[31] A. Yelon, K. N. Piyakis and E. Sacher, "Surface plasmons in Drude metals," *Surface Science* **569,** pp. 47-55, 2004.

[32] G. W. Ford and W. H. Weber, "Electromagnetic interactions of molecules with metal surfaces," *Physics Reports* **113,** pp. 195-287, 1984.

[33] R. Fuchs and F. Claro, "Multipolar response of small metallic spheres," *Physical Review B* **35,** pp. 3722-3727, 1987.

[34] N. D. Mermin, "Lindhard dielectric function in the relaxation-time approximation," *Physical Review B* **1,** pp. 2362-2363, 1970.

[35] F. Bloch, "Inkoharente rontgenstreuung und dichteschwankungen eines entarteten Fermigases," *Helvetica Physica Acta* **7.4,** pp. 385-405, 1934.

[36] H. Jensen, "Eigenschwingungen eines Fermi-gases und anwendung auf die Blochsche bremsformel für schnelle," *Zeitschrift für Physik* **106,** pp. 620-632, 1937.

[37] P. M. Platzman and P. A. Wolff, "Waves and Interactions in Solid States Plasmas," Holt, Academic, New York, 1973.

[38] G. Barton, "Some surface effects in the hydrodynamic model of metals," *Reports on Progress in Physics* **42,** pp. 963-1016, 1979.

[39] Y. E. Lozovik and A. V. Klyuchnik, "The Dielectric Function of Condensed Systems," (edited by L. V. Keldysh, D. A. Kirzhnitz and A. A. Maradudin, pp. 299-3817) North-Holland, Amsterdam, 1989.

[40] O. K. Harsh and B. K. Agarwal, "Surface-plasmon dispersion relation for the inhomogeneous charge-density medium," *Physical Review B* **39,** pp. 8150-8152, 1989.

[41] R. H. Ritchie and R. E. Wilems, "Photon-plasmon interaction in a nonuniform electron gas," *Physical Review Letter* **178,** pp. 372-381, 1969.

[42] P. Zacharias and K. L. Kliewer, “Dispersion relation for the 3.8 eV volume plasmon of silver,” *Solid State Communication* **18,** pp. 23-26, 1976.

[43] A. Liebsch, “Surface plasmon dispersion of Ag,” *Physical Review Letter* **71**, pp. 145-148, 1993.

[44] A. Liebsch, “Surface plasmon dispersion and size dependence of Mie resonance: Silver versus simple metals,” *Physical Review Letter B* **48,** pp. 11317, 1993.

[45] C. Min, P. Wang, X. Jiao, Y. Deng and H. Ming, “Beam manipulating by metallic nano-optic lens containing nonlinear media,” *Optics Express* **15,** pp. 9541-9546, 2007.

[46] H. X. Yuan, B. X. Xu, B. Lukiyanchuk and T. C. Chong, “Principle and design approach of flat nano-metallic surface plasmonic lens,” *Applied Physics A* **89,** pp. 397-401, 2007.

[47] V. K. Jain, “Filter analysis by use of pencil-of-function : Part I,” *IEEE Transactions on Circuits System* **21,** pp. 574-579, 1974.

[48] Y. Hua and T. K. Sarkar, “Matrix pencil method for estimating parameters of exponentially damped/undamped sinusoids in noise,” *IEEE Transactions on Acoustics Speech and Signal Processing* **38,** pp. 574-579, 1990.

[49] V. K. Jain, T. K. Sarkar and D. D. Weiner, “Rational modeling by pencil-of-functions method,” *IEEE Transactions on Acoustics Speech and Signal Processing* **31,** pp. 15-23, 1983.

[50] T. K. Sarkar and O. Pereira, “Using the matrix pencil method to estimate the parameters of a sum of complex exponentials,” *IEEE Antennas and Propagation Magazine* **37,** pp. 15-23, 1995.

[51] Y. Jiang, C. Hou, X. Sun and Z. Zhou, “The coexistence of TE-TM surface waves in uniaxially anisotropic left-handed materials,” *Optics Communications* **276,** pp. 196-199, 2007.

[52] R. H. Ritchie and A. L. Marusak, "The surface plasmon dispersion relation for an electron gas," *Surface Science* **4,** pp. 234-240, 1966.

[53] J. Liu, R. Li, P. Zhu, Z. Xu and J. Liu, "Modified hydrodynamic model and its application in the investigation of laser-cluster interactions," *Physical Review A* **64,** pp. 033426, 2001.

[54] H. F. Schouten, N. Kuzmin, G. Dubois, T. D. Visser, G. Gbur, P. F. A. Alkemade, H. Blok, G. W.'t Hooft, D. Lenstra and E. R. Eliel, "Plasmon-asissted two-slit transmission: Young's experiment revisited," *Physical Review Letters* **94,** pp. 053901, 2005.

[55] Q. Cao and P. Lalanne, "Negative role of surface plasmons in the transmisson of metallic gratings with very narrow slits," *Physical Review Letters* **88,** pp. 057403, 2002.

[56] R. Gordon, "Near-field interference in a subwavelength double slit in a perfect conductor," *Journal of Optics A : Pure and Applied Optics* **8,** pp. L1-L3, 2006.

[57] A. N. Grigorenko, A. K. Geim, H. F. Gleeson, Y. Zhang, A. A. Firsov, I. Y. Khrushchev and J. Petrovic, "Nanofabricated media with negative permeability at visible frequencies," *Nature* **438,** pp. 335-338, 2005.

[58] G. Leveque and O. J. F. Martin, "Transient behavior of surface plasmon polaritons scattered at a subwavelength groove," *Physical Review B* **76,** pp. 155418, 2007.

[59] Z. S. Sacks, D. M. Kinsland, R. Lee and J. F. Lee, "A perfectly matched anisotropic absorber for use as an absorbing boundary condition," *IEEE Transactions on Antenna and Propagation* **43,** pp. 1460-1463, 1995.

[60] P. Lalanne, J. P. Hugonin, S. Astilean, M. Palamaru and K. D. Mller, "One-mode model and Airy-like formulae for one-dimensional metallic gratings," *Journal of Optics A : Pure and Applied Optics* **2,** pp. 48-51, 2000.

[61] R. Zia and M. L. Brongersma, "Surface plasmon polariton analogue to Young's double-slit experiment," *Nature Nanotechnology* **2,** pp. 426-429, 2007.

[62] C. H. Gan and G. Gbur, “Spatial coherence conversion with surface plasmons using a three-slit interferometer,” *Plasmonics* **3,** pp. 111-117, 2008.

[63] V. G. Veselago, “Electrodynamics of media with simultaneously negative electric permittivity and magnetic permeability,” (edited by S. Zouhdi, A. H. Sihvola and M. Arsalane *NATO Science*, pp. 83-97) Kluwer Academic Publishers, Dordrecht, The Netherlands, 2002.

[64] L. Chen, J. T. Robinson and M. Lipson, “Role of radiation and surface plasmon in optical interactions between nano-objects on metal surface,” *OSA Conference on Lasers and Electro-Optics/Quantum Electronics and Laser Science Conference and Photonic Applications Systems Technologies*, paper QThE6, pp. 111-117, 2007.

[65] M. W. Kowarz, “Homogeneous and evanescent contributions in scalar near-field diffraction,” *Applied Optics* **34,** pp. 3055-3063, 1995.

[66] G. Gay, O. Alloschery, B. V. de Lesegno, C. O’Dwyer, J. Weiner and H. J. Lezec, “The optical response of nanostructured surfaces and the composite diffracted evanescent wave model,” *Nature Physics* **2,** pp. 262-267, 2006.

[67] J. Elser and V. A. Podolskiy, “Scattering-free plasmonic optics with anisotropic metamaterials,” *Physical Review Letters* **100,** pp. 066402, 2008.

[68] C. Min, P. Wang, X. Jiao, Y. Deng and H. Ming, “Beam manipulating by metallic nano-optic lens containing nonlinear media,” *Optics Express* **15,** pp. 9541-9546, 2007.

[69] R. Ruppin, “Surface polaritons of a left-handed medium,” *Physics Letter A* **277,** pp. 61-64, 2000.

[70] N. Kuzmin, G. W.’t Hooft, E. R. Eliel, G. Gbur, H. F. Schouten and T. D. Visser, “Enhancement of spatial coherence by surface plasmons,” *Optics Letter* **32,** pp. 445-447, 2007.

[71] B. Wu and Y. C. Shin, “A one-dimensional hydrodynamic model for pressures induced near the coating-water interface during laser shock peening,” *Journal of Applied Physics* **101,** pp. 023510, 2007.

[72] R. Chang, H. P. Chiang, P. T. Leung, D. P. Tsai and W. S. Tse, “Nonlocal effects in the optical response of composite materials with metallic nanoparticles,” *Solid State Communications* **133,** pp. 315-320, 2005.

[73] M. T. Michalewicz, “Hydrodynamic model of collective electronic oscillations in spherical geometries,” *Topics in Condensed Matter Physics Nova Science Publishers*, New York, (edited by M. P. Das, pp.143-167), 1995.

[74] H. M. Milchberg, S. J. McNaught and E. Parra, “Plasma hydrodynamics of the intense laser-cluster interaction,” *Physical Review E* **64,** pp. 056402, 2001.

[75] M. Wakano, “Foundations for a treatment of the scattering of light by the hydrodynamical and statistical atom model,” *Journal of Mathematical Physics* **2,** pp. 803-823, 1961.

[76] K. S. Srivastava and A. Tandom, “Dispersion relation for coupled surface plasmon and surface optical-phonon waves in polar semiconductors for some finite geometrices,” *Physical Review B* **39,** pp. 3885-3888, 1989.

[77] J. Harris, “Surface-plasmon dispersion: A comparison of microscopic and hydrodynamic theories,” *Physical Review B* **4,** pp. 1021-1027, 1971.

[78] A. D. Rakic, A. B. Djurisic, J. M. Elazar and M. L. Majewski, “Optical properties of metallic films for vertical-cavity optoelectronic devices,” *Applied Optics* **37,** pp. 5271-5283, 1998.

[79] R. H. Ritchie, “Surface plasmons in solids,” *Surface Science* **34,** pp. 1-19, 1973.

[80] K. Ishikawa and B. U. Felderhof, “Dielectric response in Bloch’s hydrodynamic model of an electron-ion plasma,” *Physica A* **250,** pp. 506-516, 1998.